SANDIA REPORT
SAND2018-0436
Unlimited Release
Printed January 2018

NSRD-15: Computational Capability to Substantiate DOE-HDBK-3010 Data

David L.Y. Louie, John Bignell, Remi Dingreville, Ethan T. Zepper, Christopher J. O'Brien, Robert D. Busch and Corey M. Skinner

Prepared by
Sandia National Laboratories
Albuquerque, New Mexico 87185 and Livermore, California 94550

Sandia National Laboratories is a multimission laboratory managed and operated by National Technology and Engineering Solutions of Sandia, LLC, a wholly owned subsidiary of Honeywell International, Inc., for the U.S. Department of Energy's National Nuclear Security Administration under contract DE-NA0003525.

Issued by Sandia National Laboratories, operated for the United States Department of Energy by National Technology and Engineering Solutions of Sandia, LLC.

Available to DOE and DOE contractors from
U.S. Department of Energy
Office of Scientific and Technical Information
P.O. Box 62
Oak Ridge, TN 37831

Telephone: (865) 576-8401
Facsimile: (865) 576-5728
E-Mail: reports@osti.gov
Online ordering: http://www.osti.gov/scitech

Available to the public from
U.S. Department of Commerce
National Technical Information Service
5301 Shawnee Rd
Alexandria, VA 22312

Telephone: (800) 553-6847
Facsimile: (703) 605-6900
E-Mail: orders@ntis.gov
Online order: https://classic.ntis.gov/help/order-methods/

SAND2018-0436
Printed January 2018
Unlimited Release

NSRD-15: Computational Capability to Substantiate DOE-HDBK-3010 Data

David L.Y. Louie
Severe Accident Analysis

John Bignell, Remi Dingreville, and Christopher J. O'Brien
Structural and Thermal Analysis

Ethan T. Zepper
Fire Science and Technology

Sandia National Laboratories
P. O. Box 5800
Albuquerque, New Mexico 87185-MS0748

Robert D. Busch and Corey M. Skinner
Department of Nuclear Engineering
The University of New Mexico
Albuquerque, New Mexico 87131

Abstract

Safety basis analysts throughout the U.S. Department of Energy (DOE) complex rely heavily on the information provided in the DOE Handbook, DOE-HDBK-3010, Airborne Release Fractions/Rates and Respirable Fractions for Nonreactor Nuclear Facilities, to determine radionuclide source terms from postulated accident scenarios. In calculating source terms, analysts tend to use the DOE Handbook's bounding values on airborne release fractions (ARFs) and respirable fractions (RFs) for various categories of insults (representing potential accident release categories). This is typically due to both time constraints and the avoidance of regulatory critique. Unfortunately, these bounding ARFs/RFs represent extremely conservative values. Moreover, they were derived from very limited small-scale bench/laboratory experiments and/or from engineered judgment. Thus, the basis for the data may not be representative of the actual unique accident conditions and configurations being evaluated.

The goal of this research is to develop a more accurate and defensible method to determine bounding values for the DOE Handbook using state-of-art multi-physics-based computer codes.

This enables us to better understand the fundamental physics and phenomena associated with the types of accidents in the handbook. In this third year, we improved existing computational capabilities to better model fragmentation situations to capture small fragments during an impact accident. In addition, we have revised Chapter 6 of the Handbook "Inadvertent Nuclear Criticality", and a simulated 7A drum release in a fire condition. Thus, this work provides a low-cost method to establish physics-justified safety bounds by taking into account specific geometries and conditions that may not have been previously measured and/or are too costly to perform during an experiment.

ACKNOWLEDGMENTS

Dr. Louis F. Restrepo of Atkins NS has provided guidance and review for this project. He is one of the original contributors and reviewers to DOE-HDBK-3010, and both his expertise with DOE-HDBK-3010 and his extensive experience in the U.S. Department of Energy (DOE) facility nuclear safety have helped this project significantly. Also, Dr. Alexander L. Brown of SNL provided review and suggestions for the drum fire simulations and Jerry Hicks, a former criticality safety expert from DOE-Albuquerque Operations Office. Finally, the authors would like to express their appreciation to Dr. Alan Levin and Patrick Frias of DOE-HSS (AU-30) for overseeing this research. This work is supported by the DOE Health, Safety and Security Nuclear Safety Research and Development Program under WAS Project No. 2016HS201601210.

TABLE OF CONTENTS

1. Introduction 17
   - 1.1. FY2015 Accomplishments (Year 1) 19
     - Simulated 19
     - 1.1.1. Liquid Fire Experiments 19
     - 1.1.2. Exploratory Simulations 20
   - 1.2. FY2016 Accomplishments (Year 2) 23
     - 1.1.3. Fuego Code Improvements 23
     - 1.1.4. Re-analyzed Fire Experiment Simulations 24
     - 1.1.5. Re-analyzed Powder Release Experiments 25
     - 1.1.6. Fragmentation Exploratory Simulations 27
     - 1.1.7. Recommendations for Future Works 27
   - 1.3. FY2017 Tasks (Year 3) 29
2. Implementation of a Micromorphic Fragmentation Model in SIERRA/SM 31
   - 2.1. Model Summary 31
   - 2.2. Validation Data Sources 32
     - 2.1.1. Handbook Data 32
     - 2.1.2. Kraftwerk Union Fuel Tests 33
   - 2.3. Sequentially-Coupled Fragmentation Model 33
     - 2.1.3. Macroscale Model 33
     - 2.1.4. Microscale Model 34
     - 2.1.5. Implementation Notes 35
     - 2.1.6. Validation 36
     - 2.1.7. Results and Analysis 42
   - 2.4. Concurrently-Coupled Model 43
     - 2.1.8. Model Description 44
     - 2.1.9. Implementation Notes 47
     - 2.1.10. Current Limitations and Planned Improvements 48
   - 2.5. Summary and Conclusion 51
3. Revision of Chapter 6 of DOE-HDBK-3010 53
   - 3.1. Summary of Bounding Release Estimates 53
     - 3.1.1. Solutions 54
     - 3.1.2. Fully Moderated/Reflected Solids 55
     - 3.1.3. Bare, Dry Solids and Large Storage Arrays 55
   - 3.2. Total Fission Yield 56
     - 3.1.4. Historical Excursions 56
     - 3.1.5. Analytical Models for Solution Criticalities 67
     - 3.1.6. Analytical Models for Metal Criticalities 68
     - 3.1.7. Assessment of Fission Yields 68
   - 3.3. Summary and Conclusion 87
4. Drum Fire Release Simulation using SIERRA/SM/FM 89
   - 4.1. Problem Definition 90
     - 4.1.1. FLAME Pool Fire Experiments 90
     - 4.1.2. RART Trash Fire Experiments 92
   - 4.2. Simulation Methods 93

4.3. Drum Thermal Fluid Model: Heat Transfer....94
4.1.3. Model Description....94
4.1.4. Results....96
4.4. Drum Thermal Mechanical Model....97
4.1.5. Model Description....97
4.1.6. Results....102
4.5. Drum Thermal Fluid Model: CFD and Release....110
4.1.7. Model Description....110
4.1.8. Results....113
4.6. Summary and Conclusion....116
5. Summary and Conclusion....117
6. Recommendation for Future Works....120
7. References....122
Appendix A: Summary Table for Handbook Data....128
Appendix B: Users Guide for Micromorphic Fragmentation Model....136
B.1 Sequential Fragmentation Users Guide....137
B.2 Concurrent Fragmentation Users Guide....145

FIGURES

Figure 2-1 Flowchart illustrating the design of the sequentially and concurrently-coupled fragmentation models. 32
Figure 2-2 Macro-Scale Finite Element Model Mesh. 34
Figure 2-3 Damage to UO_2 pellet predicted by the finite-element model, 500 μs after impact. Results of the sequentially-coupled approach are provided. Degradation refers to stress degradation, with undamaged elements having a value of 1.0 and fully degraded elements having a value of 0.0. 37
Figure 2-4 Cumulative mass distribution as a function of particle size is illustrated for the sequentially applied fragmentation model (broken lines), and the new integrated two-scale model (solid lines). Macroscale data is shown in red and microscale fragmentation data is shown in blue. 37
Figure 2-5 Fragment size distribution resulting from the sequentially-coupled model for impact of an unirradiated UO_2 fuel pellet experiencing an impact energy of 1.2 J/cm^3. The broken black and red lines represent using different initial strain rate selection conditions. 38
Figure 2-6 Distribution of strain rates for the sequentially-coupled model for impact of an unirradiated UO_2 fuel pellet experiencing an impact energy of 1.2 J/cm^3. 39
Figure 2-7 Fragment size distribution using the sequentially-coupled model on Pyrex with 1.2 J/cm^3 of impact energy. The solid line represents experimental data and the broken lines show the model predictions for the (black) initial and (red) final strain-rate cases. 40
Figure 2-8 Sequentially-coupled model prediction of damage distribution of failed Pyrex test cylinder subject to 1.2 J/cm^3 of impact energy, 700 μs after impact. 40
Figure 2-9 Distribution of strain rates for the sequentially-coupled model for impact of a Pyrex cylinder experiencing an impact energy of 1.2 J/cm^3. 41
Figure 2-10 Fragment size distribution generated by the sequentially-coupled model on unirradiated UO_2 fuel, compared with data [Ruhmann 1985]. Experimental data (solid lines) are plotted with results from the microscale model initiated with the final strain rate (dashed lines). 42
Figure 2-11 Effect of strain-rate condition and impact energy [J/cm^3] on fragment size distribution. 43
Figure 2-12 Effect of strain-rate condition and impact energy on values of strain rate in individual failed elements. 43
Figure 2-13 Representation of phase-field magnitude for a 1.2J/cm^3 UO_2 impact test 110 μs after impact with a mesh resolution of 0.125 mm. The phase-field currently implemented produced a single crack and only two macroscale fragments. 49
Figure 2-14 Cumulative mass distribution determined from the concurrently-coupled model (solid line) compared with the UO_2 data of Jardin, et al. (broken line), using 0.125 mm mesh. The impact energy was 1.2 J/cm^3. The microfragment size distribution is plotted as a histogram with the hashed bar representing the cumulative number of fragments with length less than 20 μm. 49
Figure 3-1 Maximum Specific Fission Yields Resulting from Solution 70
Figure 4-1. Sierra Coupling Scheme 90
Figure 4-2. Four 55-gallon drums containing assorted trash on the circumference of a three-meter pool fire. 91

Figure 4-3. a) Pre-test drum trash b) Trash remnants inside a 55-gallon steel drum after being exposed to a 30-minute fire. 91
Figure 4-4. Drum Assembly Thermal Fluid: Heat Transfer Mesh 95
Figure 4-5. Cutaway Aria drum mesh with applied fire heat flux. Blue block is air region; green block is cellulosic waste. 96
Figure 4-6.Trash decomposition at 30 minutes and drum temperature. The red in the lower layer represents unreacted trash, while the blue represents reacted trash. 97
Figure 4-7 Drum Assembly Thermal-Mechanical Model Mesh. 99
Figure 4-8. Predicted Drum Internal Pressure from Aria Simulation. 100
Figure 4-10. Drum Temperatures from Aria Simulation (Several Snapshots in Time) 101
Figure 4-10 Simulation 1: Loss of Lid. 103
Figure 4-11 Simulation 1: Loss of Seal Integrity 104
Figure 4-12 Internal Pressure and Breach Area vs. Time (Simulations #1 and #2). 105
Figure 4-13 Simulation 1: Reduction in Breach Area Due to Mechanical Deformation of the Drum Lid. 106
Figure 4-14 Simulation 2: Lid Retained Following Drum Depressurization. 108
Figure 4-15 Simulation 2: Depressurization of Drum. 109
Figure 4-16. Thermal Fluids CFD Mesh (Half Domain) 111
Figure 4-17. CFD Mesh Vent Release Area (Half Domain) 111
Figure 4-18 CFD Mesh Boundaries (Exploded View for Clarity). 112
Figure 4-19. Contaminant Input Size Distribution. Red Circles: Experimental Size Distribution from RART, Black Line: Simulation Input Size Distribution 113
Figure 4-20. a) Particle Release from Vented 7A Drum and b) Mass Deposition Location 115

TABLES

Table 1-1 SIERRA Codes at SNL* 17
Table 1-2 Fuego Improvement Proposed for FY2016 22
Table 1-3 Recommendation for Modeling Mechanical Insult Accident Using SIERRA SM Code for FY2016 22
Table 1-4 Recommendations on Modeling Pressurized Powder Release Simulations for FY2016 22
Table 1-5 Fuego Particle Model Improvement Needs 27
Table 2-1 Fragmentation Models 31
Table 3-1 Summary of Known Accidental Criticality Excursions (1945 to 2016) [Olsen 1974, McLaughlin 2000, USAEC 1975] 57
Table 3-2 Inhomogeneous Water-Moderated Systems [Stratton 1967, McLaughlin 2000] 64
Table 3-3 Destructive Power Excursion Summary [Nyer 1965] 66
Table 3-4 Bounding Criticality Accident Fission Yields [McLaughlin 2003, Barbry 2009] 69
Table 3-5 Accident Fission Energy Releases (a) Uranium, (b) Plutonium Solution Criticality Accidents. [McLaughlin 2000] 71
Table 3-6 Estimated ARF Values for Solution Excursions. [Barbry 2009] 75
Table 3-7 Curies of Important Nuclides Released from First Spike in Uranium Solution Criticality (based on 10^{17} fissions and 100 liters of solution) 76

Table 3-8 Curies of Important Nuclides Released from Multiple Excursions in Uranium Solution Criticality (based on 10^{18} fissions and 100 liters of solution) 77
Table 3-9 Curies of Important Nuclides Released from a Slow Cooker Event Over 8 Hours in Uranium Solution (based on 10^{18} fissions and 100 liters of solution) 78
Table 3-10 Curies of Important Nuclides Released from First Spike in Plutonium Solution Criticality (based on 10^{17} fissions and 100 liters of solution) 80
Table 3-11 Curies of Important Nuclides Released from Multiple Excursions in Plutonium Solution Criticality (based on 10^{18} fissions and 100 liters of solution) 81
Table 3-12 Curies of Important Nuclides Released from a Slow Cooker Event Over 8 Hours in Plutonium Solution Criticality (based on 10^{18} fissions and 100 liters of solution). 82
Table 3-13 Assumed Fission Product and Transuranic Nuclide Atom Density and Activity in Spent Fuel Solution Based on (ORIGEN calculations for 33 GWd/MT and 150-day cooling) 84
Table 3-14 Plutonium Isotopes, Specific Activities, and Estimated Activities per Gram of Weapons Grade and Reactor Grade Material 85
Table 3-15 Release Fractions for Solid Systems Based on Table 3.2 from [NUREG 1997] 86
Table 4-1 Average mass fraction composition of waste materials in FLAME and RART contaminant release experiments 92
Table 4-2 Arrhenius Reaction Values for Two-Step Cellulose Decomposition 95
Table 4-3 Trash Decomposition Gases 95
Table 4-4 Predicted Mass Deposition Location and ARF from TF/CFD Simulation 116

NOMENCLATURE

Abbreviation	Definition
Abbreviation	Definition
1-D	One-dimensional
3-D	Three-dimensional
AED	Aerodynamic equivalent diameter
ANS	American Nuclear Society
ARF	Airborne release fraction
ASC	Advanced Simulation and Computing
BC	Boundary condition
BNWL	Battelle Northwest Laboratory
CFD	Computational Fluid Dynamics
DOE	Department of Energy
DR	Damage ratio
DSA	Document Safety Analysis
EDC	Eddy dissipation concept
EOS	Equation of state
FD	Fluid dynamics
FY	Fiscal year
GDE	Gradient damage explicit
HEPA	High efficiency particulate air
HEU	Highly Enriched Uranium
hr	Hour
IC	Integrated Code
ISO	International Organization for Standardization
ITAR	International Traffic in Arms Regulations
KEWB	Kinetic Experiments on Water Boilers
LAME	Library for Advanced Materials Engineering (Material models for SIERRA/SM)
LES	Large-eddy simulation
LPF	Leak path factor
Ma	Mach number
MAR	Material-at-risk
mph	Miles per hour
MS	Mishima and Schwendiman
NRC	Nuclear Regulatory Commission
NSRD	Nuclear Safety Research and Development
ODE	Ordinary differential equations
ORIGEN	Isotope Generation and Depletion Code System Developed by Oak Ridge National Laboratory
PARE	Pressurized airborne release equipment
PDF	Probability Density Function
PNL	Pacific Norwest Laboratory
RART	Radioactive airborne release tank

Abbreviation	Definition
RANS	Reynolds averaging of the Navier Stokes equations
RF	Respirable fraction
RG	Reactor Grade Enrichment
SAR	Safety Analysis Report
SCALE	Comprehensive Modeling and Simulation Software for Nuclear Safety Analysis and Design Developed by Oak Ridge National Laboratory
SD	Structural dynamics
SE	Solution Experiment Incident
SM	Solid mechanics
SNL	Sandia National Laboratories
SP	Solution Processing Incident
SPH	Smoothed particle hydrodynamics
ST	Source term
TBP	Tributyl phosphine
TF	Thermal fluid
UNH	Uranium nitrite
WG	Weapons Grade Enrichment
W	Water Moderated Incident

Symbols for Chapter 2

Symbol	Definition
$A_{0\mu}$	Coupling material constant in Eq. (2-21)
$B_{0\mu}$	Coupling material constant in Eq. (2-21)
Δt	Time-step of microscale model
E	Young's modulus of material
E_0	Young's modulus at macroscale used in Section 2.4.3.3.
E_μ	Young's modulus at microscale used in Section 2.4.3.3
$E^\star$	(Effective) Young's modulus used in phase-field equations
ρ	Density of material or macroscopic density for Eq. (2-18)
v_c	Speed of sound in material
ΔX	Minimum microfragment size (resolution of 1-D model)
L	Maximum microfragment size (length of 1-D bar)
M	A point on a 1-D bar in a undeformed state
M'	A point on a 1-D bar in a deformed state
N	Number of cohesive zones
η	Interactive microforce for Eq. (2-19)
σ_0	Initial stress applied on microfragmentation model

Symbol	Definition
σ	Macrostress (Piola stress) used by Eq. (2-18)
D_i	Individual cohesive-zone damage value (calculated with microscale model)
$\dot{\epsilon}_{\mathrm{M}}$	Macroscale Strain rate projected onto direction of stored maximum principal stress
$\dot{\epsilon}_{\mu}$	Microscale Strain rate in 1-D bar
G_c	Fracture energy (fracture energy release-rate)
K_{1c}	Fracture toughness
ℓ	Fracture length-scale
ψ_e^+	Undamaged tensile strain energy
ψ_e^-	Undamaged compressive strain energy
c	Phase-field value
c_c	Critical value of phase-field variable indicating onset of fracture
$\mathcal{H}$	History function, ensures that argument always increases
Γ	Energy dissipated by crack opening
ϵ_{ij}	Strain tensor component of continuum model
$\boldsymbol{\epsilon}$	Strain tensor of continuum model
$\boldsymbol{\epsilon}^e$	Elastic portion of strain tensor of continuum model
ν	Poisson's ratio
v	Macroscopic velocity that equals to u_t in Eq. (2-20)
u_{tt}	The second partial derivative of u with respect to t
u	1-D bar displacement field in an un-deformed state
u'	1-D bar displacement field in a deformed state
μ	Microstress (coupled stress) for Eq. (2-19)
μ_x	The first derivative of μ with respect to x for Eq. (2-19)
$\boldsymbol{\sigma}$	Stress tensor of continuum model
σ_c'	Critical stress defined by phase-field model
σ_c	Critical stress to initiate fracture (opening of cohesive-zone)
ς	Direction of maximum principle stress upon reaching σ_c
I_μ	Micro-inertia associated with microvolume around the material point M
t	Subscript for partial derivative with respect to time for Eqs (2-18) to (2-20)
x	Subscript for partial derivative with respect to space for Eqs. (2-18) to (2-20)

Symbols for Chapter 3

Symbol	Definition
$c1$	Subscript for the volatile designation in Equation (3-1)
$s1$	Subscript for the non-volatile designation in Equation (3-1)
$c2$	Subscript for Equation (3-2)
m	Mass (kilograms)
$\boldsymbol{N_f}$	Total Integrated Fission Yield
$\boldsymbol{t}$	Time (seconds)
$\boldsymbol{t_{\frac{1}{2}}}$	Half-Life
$\boldsymbol{V}$	Volume (liters)

Symbols for Chapter 4

Symbol	Definition
A_i	Vented area
A_n	Reaction specific pre-exponential factor
C_d	Discharge coefficient
C_r	Critical ratio
E_n	Activation energy
k	Heat capacity radio
$\dot{m}$	Mass flux through the vent
P_{atm}	Atmospheric pressure
P_i	Pressure at current step
R_g, R_u	Universal gas constant
r_n	Reaction rate
T	Temperature
T_i	Temperature at current step
t	Time
Y_R	Mass fraction of the trash
$\bar{\rho}$	Average density

1. Introduction

Safety analysts throughout the U.S. Department of Energy (DOE) complex rely heavily on the data provided in the DOE Handbook (referred to herein as the Handbook), DOE-HDBK-3010 [DOE 1994], to determine radionuclide source terms (STs) in support of safety and risk analyses in documented safety analysis (DSA) or risk analysis documents. In calculating source terms, analysts tend to use the Handbook's bounding values on airborne release fractions (ARF) and respirable fractions (RF) for various categories of insults (representing potential accident release categories). This is typically due to both time constraints and the avoidance of regulatory critique. Unfortunately, these bounding ARF/RFs may represent extremely conservative values. Moreover, they were derived from very limited small-scale and bench/laboratory experiments, as well as from engineering judgment which may not have been substantiated. Furthermore, these previous estimates may not be representative of the actual accident conditions and configurations under consideration. In response, we have proposed including high-fidelity modeling to provide a more accurate and defensible method to identify not only bounding values, but also more representative values that can be used by analysts tasked with risk assessments.

Advances in computing capability at national laboratories have enabled us to use computer simulations to better model hydrodynamic, structural dynamic, and thermal/fluid dynamic phenomena. This provides a better understanding of the insights on the fundamental physics related to potential accident scenarios that could occur or could be postulated. Today, the availability of the high-fidelity computer resources (both hardware and software) that incorporate state-of-the-art models at national laboratories allows safety and risk analysts to utilize these methods for non-weapon-related safety activities. An example of the use of these state-of-the-art models in supporting source term calculations and in particular ARFs for postulated scenarios is the SIERRA high fidelity codes developed at Sandia National Laboratories (SNL). The SIERRA codes are designed to solve multi-physics engineered problems, particularly for weapon applications (see Table 1-1).

Table 1-1 SIERRA Codes at SNL*

Module/Code Name	Description	Potential Application
Solid mechanics (SM) [SIERRA 2017a]	A three-dimensional solid mechanics code with a number of features: versatile element library, nonlinear material models, large deformation capabilities, and contact. • Adagio –The standard SM code that currently provides the full suite of both explicit and implicit capabilities. In the past, the SM code for solving problems in explicit and implicit capabilities was separated into Presto and Adagio, respectively. Thus, Presto executable became obsolete. • Presto_itar – This SM code version provides capabilities to material models with an energy-dependent pressure response, such as for very large deformations and strain rates and for blast modeling [SIERRA 2017b]. The use of this code version falls under the U.S. Department of State's International Traffic in Arms Regulations (ITAR) export-control rules. Many of the material models in this version are similar to those models in CTH code.**** • Peridynamics – an extension of the SM code for modeling classical solid mechanics problems, such	May be used to model impacts, large deformation of solids, powders, and liquid dispersals using a smoothed particle hydrodynamics (SPH) model.

	as the modeling of bodies in which discontinuities occur spontaneously.	
Structural dynamics (SD)	Used to perform most traditional structural dynamics simulations in time and frequency domains, including stress and fatigue calculations. These calculations could include energy dissipation at discrete joints. Since this SD module has a massively parallel capability, it can efficiently perform simulations to millions of degrees of freedom. Its variety of equations solvers enables solving problems with a large number of constraints. This module also includes a structural-acoustics capability for simulating noise-induced structural vibration or response due to a given noise source [SIERRA 2017c].	May be used to determine the failure of the structural-related components in the problem. No apparent applications for this research at this time.
Thermal Analysis**	Aria, Calore, and Chaparral modules comprise the state-of-the-art thermal analysis tools using massive parallel capability: • Aria is a Galerkin finite element-based program for targeting applications that involve incompressible flow and primarily focus on energy transport; species transport with reactions; electrostatics; and the general transport of scalar, vector, and tensor quantities in two and three dimensions for both transient and direct-to-steady state. It is a thermal fluid (TF) code. • Calore approximates linear and nonlinear continuum models of heat transfer. • Chaparral is a library package to address three-dimensional enclosure radiation heat transfer problems.	May be used to determine situations requiring detailed thermal analysis. No apparent applications for this research at this time.
Fluid dynamics (FD) with low Mach**	Fuego*** is an FD module for the SIERRA code suite. Fuego is designed to predict low-Mach number (Ma<0.3) reacting flows, and has a capability to model particle and drop transport using a dilute spray approximation Lagrangian/Eulerian coupling. The liquid phase can be modeled as individual Lagrangian drops that interact through momentum source terms with the Eulerian gas phase. It couples with Syrinx, a media radiation heat transfer module, to simulate a more complete heat transfer and FD problems, such as fires. Fuego models particles in terms of user input or code generated as in soot from a fire. With the particle capability, it can model particle dispersal; however, Fuego does not currently model particle interaction, which is important for the particulate release out of a pathway.	Useful to model fire with particulates and droplet/powder release due to an elevated pressure effect.
Fluid dynamics (FD) with high Mach**	Aero module that can model flow problems at Mach numbers in excess of Mach 8. It can model gas flow in two and three-dimensional problems, which can approximate the compressible Navier-Stokes equations on unstructured meshes.	Useful to model deflagration types of accidents, particularly their flow conditions. Aero currently does not have a particle model, and thus has no apparent applications for this research at this time.

*see [SIERRA 2016] for more details on the specific module description and usage. This suite is compliant to DOE Order 414.1D [Minana 2012].

**These codes and modules make up the SIERRA Thermal Fluid (TF).

***[SIERRA 2017d]

****http://www.sandia.gov/CTH

This report summarizes our research on the application and use of these types of codes in determining ARFs in our first two years of funding

Starting in FY2015, this research was funded by DOE Nuclear Safety Research and Development (NSRD) Program. Sections 1.1 and 1.2 summarize accomplishments from the first two years of the funded project, which are more extensively documented in SAND reports [Louie 2015] and [Louie 2016]. FY2017 tasks are discussed in section 1.3.

1.1. FY2015 Accomplishments (Year 1)

Two tasks were assigned in the first year of the project.

- Simulate the liquid fire experiments in the Handbook.
- Conduct exploratory simulations, such as an object hitting a can filled with powders and pressurized release experiments from the Handbook, to identify if SIERRA codes can be used to model solid particle entrainment.

The SAND report "NSRD-6: Computational Capability to Substantiate DOE-HDBK-3010 Data" documents our accomplishments [Louie 2015]. Sections 1.1.1 and 1.1.2 summarize Year 1 accomplishments based on the two tasks assigned.

1.1.1. Simulated Liquid Fire Experiments

For the first task (simulate the liquid fire experiments in the Handbook), we simulated a beaker fire and a gasoline pool fire.

For the beaker fire, there were 25 ml of kerosene with 30% Tributyl phosphine (TBP) and contaminants in a beaker and a chimney apparatus to ensure no cross-flow [Mishima 1973]. A Fuego model was developed for droplet entrainment during the boiling for the release of the contaminants. An initial droplet size distribution was employed to model droplet breakup during rising bubbles. The simulations included a number of parameter variations, such as the initial liquid height and turbulence induced at the boiling surface. The sensitivity to the initial fuel height was significant, since results indicated that this parameter is closely related to the airborne release. The aerosol release for a 20 mm initial liquid height showed reasonable agreement with the data. Beaker wall deposition was also observed in the simulations. Since Fuego does not currently have a liquid level depletion model, no resuspension is used. The beaker simulation study identified these major findings:

- Liquid height might influence the release of contaminant, a parameter not considered in the experiments.
- The effect of flow turbulence was not particularly significant.
- Much of the airborne release was predicted to occur at the beginning of the simulations during the ignition.

In addition to the beaker fire, a gasoline pool fire with ~20 g of UO_2 powder was simulated using Fuego [Mishima 1973a]. For this experiment, a steel pan was located inside a wind tunnel, in which gasoline contaminated with UO_2 was allowed to entrain. In this simulation series, a number of entrainment phenomena were considered in the model such as evaporation induced entrainment (EIE) and agitation by boiling (similar to that in the beaker fire). Although wind can be important for resuspension, this aspect of these tests was not simulated because Fuego currently does not model resuspension. In subsequent work (FY2016), we implemented and tested a resuspension

model (see Section 1.2). As demonstrated in the gasoline pool fire simulation, the deposited mass on the walls of the wind tunnel is small compared to the outflow of the airborne materials. The magnitude of the EIE is very small in comparison to the boiling. All cases were found to have higher ARF values than that of the experiments, but this was driven by the assumed boiling time. Better assessments of the boiling time are needed.

The pool fire simulation series concluded that:

- The entrainment mechanism (surface agitation by boiling) significantly dominated the entrainment during flaming.
- Turbulence boundary conditions were not reported, and a practical range of assumptions results in significant uncertainty in the ARF for the above entrainment mechanisms.
- The boiling mechanism was found to be the significant contributor to the amount of entrained mass. Modeling particle entrainment from pool boiling will improve the modeling accuracy.

1.1.2. Exploratory Simulations

In addition to the liquid fire simulations, exploratory simulations were also conducted to identify if SIERRA codes can be used to model solid particle entrainment.

For a projectile impacting a can filled with UO2 powder, the simulations for the powders included the use of the Mie-Gruneisen Equation of State (EOS) Model and the Soil-Crushable Foam material model using SIERRA/SM.

Two simulation impact speeds of 20 m/s and 175 m/s were conducted. Two mesh models (coarse and fine) were also used for the simulation. A total of five cases were simulated. In general, a 20 m/s impact velocity of the projectile would puncture a hole in the can, which leads to powder escaping. At this velocity, the can remains stationary while the projectile rebounds. On the other hand, when the impact speed increases to 175 m/s, the projectile penetrates the can and becomes lodged inside while the can flies upward. During can lofting, particles escape through the opening. Eventually, the can falls back and hits the floor again. During this time, additional release near the bottom of the can was observed in the simulation. This release may not be realistic. Therefore, additional 20 m/s impact velocity cases were simulated to observe this secondary release. Only cases with the Mie-Gruneisen EOS material model were observed to have this behavior. The use of the Soil-Crushable Foam material model did not exhibit the secondary release. Perhaps the Mie-Gruneisen EOS material model may not appropriate for low impact speed scenarios; it may instead be appropriate for explosion simulations or high-impact velocity simulations where shocks are developed. Further analysis of this behavior for the Mie-Gruneisen EOS model may be needed. On the other hand, the Soil-Crushable Foam material model is useful for modeling the impact from an accident.

From the projectile impact case, we concluded:

- SIERRA/SM code can be used to simulate solid entrainment using an SPH model.
- The use of Mie-Gruneisen EOS material model should be limited for shock related impact type of accidents.

- The use of a Soil-Crushable Foam material model is useful for modeling impact accidents.
- The use of coarse and fine mesh models for the same simulation model suggests that the model may behave well.
- Problems with a longer duration are needed to observe unrealistic model results.

The other exploratory powder simulations involved the pressurized release from a container to a containment type volume [Sutter 1983]. Here, because of known limitations of Fuego's model for particle interactions, the MELCOR code was also used. Although MELCOR is a system-level code, it contains an aerosol physics model [Humphries 2015]. Because the MELCOR aerosol physics model is based on concentrations of the airborne aerosol, multiple volumes were required. A single volume model and a two-volume model have been developed. Two pressure cases were simulated (50 psig and 250 psig). A better modeling method is needed to include the utilization of both Fuego and MELCOR to model this type of simulations..

A preliminary Fuego model was developed to simulate the 50 psig case of the experiment. Although the surfaces for the model are assumed to re-bound rather than stick, a 60-second run showed the impingement of the particles on the ceiling. This result is consistent with the experimental results.

From these exploratory pressurized powder release simulations, we concluded:

- Although MELCOR is a system-level code with a concentration based on an aerosol physics model, it can be used to simulate this type of experiment.
- Fuego, on the other hand, has been used to model fires as described in Section 1.1.1. This FD code can be extended to model pressurized powder release.
- Fuego may not be appropriate for modeling high pressure conditions since it is designed for low-Mach flow.
- Although Fuego currently does not have a particle interaction model, it can be used to identify the particle impingement to walls and ceilings.

Note that these exploratory simulations were intended to demonstrate the code's capability in FY2015. At the year one stage, the simulations were not intended to be compared to experimental results. Further analyses of scenarios using MELCOR and Fuego for pressured powder release were continued in subsequent work (in FY2016).

The following three tables summarized the further work needed from year one (i.e., FY2015). Table 1-2 lists the Fuego improvement proposed for FY2016. Table 1-3 provides the recommendations for modeling mechanical insults using the SM code. Finally, Table 1-4 lists the recommendations for simulating powder release experiments conducted. Many of the code improvements and recommendations were accomplished in FY2016 (see Section 1.2). However, no further study was made for the recommendations described in Table 1-3.

Table 1-2 Fuego Improvement Proposed for FY2016

SIERRA FD code (Fuego) Recommendation	Potential Benefit
Multicomponent particle capability	This capability is particularly useful when fuel and solids (contaminants) are mixed, allowing fuel to evaporate while solids remain during the fire
Resuspension of particle capability	This capability is important for resuspension of deposited materials from the walls or burn residues resuspended under wind conditions

Table 1-3 Recommendation for Modeling Mechanical Insult Accident Using SIERRA SM Code for FY2016

Model and Simulation Improvement	Potential Benefit
Mie-Gruneisen EOS Material Model	This model should be used with caution, particularly with the SPH capability for modeling particle dispersal. It should only be applied to explosion simulations and high-velocity impact cases where shocks can be developed. In addition, this model is only available in Presto (ITAR version) of the SIERRA SM code. Discussions of the model and results are limited.
Soil-Crushable Foam Material Model	This material model should be suitable for modeling low-velocity impact cases as described in Section 1.1.2. It tends to be stable in comparison to the Mie-Gruneisen EOS model above for the same simulation model. Unlike the Mie-Grunesien EOS model, this material model can be obtained from Adagio, which may not be restricted in terms of export controls.

Table 1-4 Recommendations on Modeling Pressurized Powder Release Simulations for FY2016

Model Improvement	Potential Benefit
Multi-volume MELCOR model	This multi-volume MELCOR model may improve results with the experiment since the aerosol physics model depends on concentration.
Flow of Air exchange during experiment needed to be included in MELCOR model	During the aerosol measurement, air inside the containment volume was exchanged 80 times. This exchange may improve MELCOR model results with experimental data.
Refined Fuego model	Proper modeling of the experiments is needed, including those described in the MELCOR model improvement above. This would improve the particle deposition results on the walls and ceiling of containment.

Fuego/MELCOR Coupling	Since Fuego currently does not model particle interactions, the Fuego results, particularly for the wall and ceiling deposition, can be used in conjunction with MELCOR results to compare with the experimental data. This coupling would improve the calculation results to experiments.
Adagio/Fuego/MELCOR Coupling	As described in this research, Fuego can only model pressurized powder release with a 50 psig pressure. To model higher pressure cases, the use of the SPH particle model in Adagio may be required. The results of Adagio are then used by Fuego to predict impingement. Finally, the results are used in MELCOR to determine the final results to compare with the experiments.

1.2. FY2016 Accomplishments (Year 2)

During FY2016, we:

- Improved the Fuego code to add both the multi-component evaporation model and the particle resuspension model.
- Re-analyzed the beaker fire and gasoline pool fire experiment simulations
- Re-analyzed the powder release experiment started in the exploratory simulation of Year 1, and
- Conducted exploratory fragmentation simulations

The recommendations from FY2016 are summarized in Section 1.1.7.

Based on the recommendations from Year 1, we accomplished what was proposed to DOE. A final report documents what was accomplished in FY2016, the second year of the project [Louie 2016]. In this section, we summarize Year 2 accomplishments and the list of recommendations for Year 3.

1.1.3. Fuego Code Improvements

Based on Table 1-2, Fuego was improved in FY2016 to add both the multi-component evaporation model and the particle resuspension model.

Particle Resuspension Model

In the resuspension model effort, we attempted to characterize the model by using a number of parameters that can be input to Fuego, allowing various flow and particle conditions. The basic resuspension model is based on the Wichner resuspension model described in [Young 2015]. This model is a force balance between the lift and adhesive forces. A similar resuspension model has been implemented in MELCOR [Humphries 2015]. To account for a mechanism for the various particle size and surface properties where the particles were originated, this model in Fuego has been extended to be a stochastic resuspension model, accounting for a probability function. In addition, based on the effect of the boundary layer near the surfaces, it is necessary to include a model of calculating the wall shear stress. We have demonstrated development test problems,

which illustrates the usefulness of the model. Without additional work, this model may be only suitable for a certain range of particle sizes and flow velocities.

Multi-Component Evaporation Model

In terms of the multi-component evaporation model, we have provided a basic evaporation model, and a simplified approach to model multi-components of an evaporating droplet. We also provided development example inputs for testing this model. The simplified approach describes the beaker fire experiment which was described in detail in Chapter 4 of [Louie 2016]. The resuspension model was used in Chapter 3 for analyzing two experiments from the Handbook.

1.1.4. Re-analyzed Fire Experiment Simulations

Based on the recommendations from Year 1, Fuego improvement, such as resuspension and multi-component evaporation models, has been done. Thus we re-analyzed the beaker and gasoline pool fire simulations as described in Year 1.

Beaker Fire Experiment:

For this experiment, we concluded the following:

- Our results indicate that contaminant release from a burning fuel with entrained contaminant droplets is not principally due to initial flame dynamics, though that was observed in the original study in Year 1 with non-evaporating inertial particles.
- The variation of the particle insertion data played the largest role with turbulence variation near the pool surface showing less importance. Initial pool height had large impact on the ARF, and, as in the earlier study, it is clear that more experimental results would be helpful in exploring this variation.
- Since the goal of the Handbook is to provide conservative estimates for these scenarios, and greater contaminant release rates were observed both at lower (0mm) and higher (40mm) pool heights than the nominal of 20mm, variation in pool height should be explored further.

Gasoline Pool Fire Experiment:

For this experiment, we concluded the following:

- Multiple entrainment mechanisms were presented as potential methods for hazardous contaminant release from contaminated fuel fires.
- The predicted ARF calculated by a CFD code was compared to the ARF measured in a relevant historical experiment and previous computational work. The addition of multiple species evaporation and deposition for particles provided new insight to the entrainment dynamics. The volatile fuel was seen to evaporate rapidly in the fire above the pool surface, increasing the likelihood that the remaining non-volatile solid contaminant would transport down the wind tunnel and reach the outflow.
- Practical assumptions for the turbulence boundary conditions result in significant uncertainty in the ARF.
- Boiling mechanism duration was again found to be the most significant factor in predicting the ARF. Improved modeling of particle entrainment from pool boiling will help the quantitative accuracy of this type of modeling.
- The particle input temperature did not significantly alter the volatile evaporation, resulting in similar contaminant release.

- Future work would include longer duration simulations of the resuspension of deposits left from a multiple component boiling entrainment scenario in order to detect contaminant release at the collection point, potentially enabling a prediction of the resuspension entrainment ARF.

1.1.5. Re-analyzed Powder Release Experiments

In terms of re-analyzing the powder release experiment started in the exploratory simulations during FY2015, we were able to simulate the pressurized release experiment entirely. In addition, to address the shortcoming of the low Mach limitation of Fuego, we were able to couple SIERRA/SM to Fuego to model high Mach pressurized release experiment. In addition, we included the simulation of the gravitational spill of the powder using Fuego.

In Year 2 (FY2016), three simulations were conducted for the free-fall spills. 50 psig (0.34 MPa) and 250 psig (1.72 MPa) pressurized powder release cases in the experiments were also performed.

Free-Fall Spill

A gravitational (free fall) spill simulation of 100 g of TiO_2 powder in a beaker has been done, 10^8 out of 10^{13} of the particles in 100 g were tracked. We have used a fine mesh for this simulation, which is a significant improvement over that of Year 1. We model the prescribed sample flow and introduce a turbulence model approximation, both improvements over the Year 1 effort. When the beaker is turned, the falling powder will interact the surrounding air, and induce the fluid flow within the radioactive airborne release tank (RART) volume. The induced fluid velocity can be used by MELCOR [Louie 2017]. We were able to run the simulation to the experiment end time of 30 minutes.

However, the aerosol result of the simulation overestimates the ARF in terms of the particles collected in the samples. This difference may be due to the following factors:

- Fuego currently does not model agglomeration, which may cause the settling to be faster.
- The assumption of 10^8 (10^5 with 1000 particles per parcel) particles in the model versus the actual number of particles of 10^{13} may overestimate the number of particles pulled through the samples.
- The turbulence flow model used may influence the mixing that causes the overestimation.
- The percent particle collected is a number percent, which may be different than the experiment data as a mass percent.

Pressurized Release

In the pressurized release experiments, we conducted both 50 psig (0.34 MPa) and 250 psig (1.72 MPa) cases. Because Fuego is a low-Mach number, Ma (< 0.7) fluid code, we can only model the 50 psig (0.34 MPa) case (Ma is about 0.38). For the higher-pressure case, we use SIERRA/SM (Presto) code to perform the initial blast of the powder and pass the particle data to Fuego at a later time for simulating the rest of the experiment condition.

50 psig (0.34 MPa) Case

For the 50 psig (0.34 MPa) pressure case, the simulation of the rupture disk in the experiment for the pressure release from the PARE to RART was assumed to be done within approximately one millisecond. The fluid velocity of 643 m/s was assumed for this pressure case. The results show that the particle cloud rises up toward the ceiling of RART in a short time, while the sampling (or filters) flow pulls the particles toward the sampling devices. As the simulation continues, particles that impact to the ceiling or hit the PART walls will stick or deposit. Because of the difficulties to observe any deposition, additional simulation runs with fluid open boundary conditions were used to allow depositions. Despite this issue, the deposition values were reported for both the ceiling and filters.

250 psig (1.72 MPa) Case

For the 250 psig (1.72 MPa) pressure case, the simulation of the powder release of 250 psig (1.72 MPa) was first done using Presto code. Initially, a coarse mesh was used to model the TiO_2 powder by using SPH model in the pressurized airborne release equipment (PARE) with the prescribed pressure as the induced pressure (or stress) load. However, the size of this stress is insufficient to induce the release of the powder. Therefore, a multiplication of 1000 is applied to this stress. This increase in value is justified because Presto models solids. Presto does not model fluid, even though there is an ideal gas model (only in the ITAR version), which is not truly modeling the gas as in a fluid code like Fuego. In reality, when the PARE is pressurized, both powder and air inside the PARE are at pressure. Without modeling the gas portion, the induced stress needed to be larger in order to push the particles out of the PARE volume. When passing the particles to Fuego, the induced fluid flow by the injecting particles may not yield the actual fluid conditions as in the experiment. That is why the use of the multiplier is justified.

At first, the coarse particle sizes in the order of millimeters from the Presto run were input to the Fuego run. The Fuego model was based on the "no flow" case for the 50 psig (0.34 MPa) simulation described. In this case, the Fuego run showed that the particles were stuck to the surfaces early because the particles are too large. In the fine particle size run (using the results of Presto in the second run), the Fuego results showed that the particles were very slow because the micron-sized particles could not influence the fluid in the RART volume. Therefore, the multi-size particle run (using final run of Presto simulation) was conducted. In this simulation, the results are more encouraging. However, the results showed slightly improved deposition onto the middle ring of the RART ceiling in comparison to what was observed in the same case for the 50 psig (0.34 MPa) simulation. This may be because of the selection of the turbulence model chosen or other effect associated with the boundary layer. Thus, iterations may be required to model the condition of the experiment correctly.

In conclusion, the coupled method of using Presto and Fuego has proven to be useful to address high Mach number flow, which Fuego alone cannot be able to handle. However, iterations and the use of a multi-size particle approach are needed in order to produce meaningful results.

1.1.6. Fragmentation Exploratory Simulations

In addition to above, the fragmentation analysis in Year 2 was intended to explore if SIERRA/SM code can be used to simulate the fragmentation experiment data described in Section 4.3.3 of the Handbook.

The two-scale modeling approach uses the finite element method to simulate dynamic fracture under general loading and boundary conditions to determine macro-scale fragmentation. At the lower length scale, a 1-D model is used to determine the micro-scale fragmentation. Boundary conditions for the 1-D model are derived from the macro-scale model. Fragmentation characteristics from both length scale models are combined to determine the resulting fragment size distribution spanning both length scales.

The two-scale modeling approach presented has been shown to be capable of providing reasonably accurate particle size distribution predictions across the entire particle size range of interest for brittle radioactive material forms susceptible to fracture through its application to a laboratory scale UO_2 impact test. The approach is particularly promising because it provides the necessary level of accuracy, fidelity, and versatility for making safety assessments of brittle radioactive materials subjected to wide ranging accident conditions while remaining computationally tractable.

1.1.7. Improvement Identified

In Year 2, we provided several needed code and simulation improvements to assess the Handbook data.

Fuego Code Improvement

In Year 2, we implemented two new particle models into SIERRA/FD (Fuego): resuspension and multi-component evaporation models. Both models have been tested. We offer several Fuego improvements to better model the ARF data in the Handbook (see Table 1-5).

Table 1-5 Fuego Particle Model Improvement Needs

Model	Description
Agglomeration	Although the adhesive model is being implemented in the code, the completion of the agglomeration model will help to better model the powder release simulations as described in Chapter 5.
Deposition	Deposition is an important model for aerosol physics. In this research we have encountered a number of issues relating to the deposition (*sticking* in Fuego's terms) when the particles are deflected from the surfaces. If the deposition allows the particles to agglomerate as in a real situation, then the particle resuspension model can be more realistic, since the current resuspension only models the resuspension according to the same particle deposition size distribution (that ignores agglomeration).
Boundary Layer	The particle impact behavior in the boundary layer needs further validation.

Fuego Resuspension Model Testing

We attempted to test the particle resuspension model by selecting resuspension experiment data from the Handbook and a reactor experiment of STORM SR-11 (see Chapter 3 of [Louie 2017]). However, we decided to stop the simulation of the STORM SR-11 test because the high fluid velocity creates a large computational cost to resolve the flow for the long duration of the experiment. On the other hand, we successfully demonstrated model predictions for the human activity resuspension experiment (see Chapter 3 of [Louie 2017] for the Fish experiment) from the Handbook. Because the experiment was not well described in the test report, (conditions such as the pace of the human walking on a contaminated surface and the collection method) it is difficult to assess model accuracy. Therefore, a number of assumptions were used to model the human walking and duration. The Fuego calculation with the resuspension model did not compare well with the experiment data. Because the calculation was done using an older version of Fuego which did not include turbulent variations in the wall shear stress, it is recommended that the calculation be re-done with the final version of the resuspension model. In addition, a separate calculation without the use of the resuspension model should be conducted to ensure that the assumed human walking motion model in the Fuego simulation induces realistic resuspension.

Fire Experiments

In Year 2, we have demonstrated that the improved Fuego models—such as the multi-component evaporation model—could contribute better predictions of the experimental data in both beaker and gasoline pool fires. We were not able to demonstrate the resuspension model fully for the gasoline pool fire test due to lack of a relevant model parameter set. The deposition model in Fuego may require the addition of particle agglomeration models to capture some of the relevant deposition processes. To better observe the resuspension phenomena, the simulations needed to be run longer to be more consistent with the experiment.

Powder Release Experiments

In Chapter 5 of [Louie 2017], we modeled the gravitational (free-fall) experiment and two pressurized release cases (50 psig and 250 psig) of TiO_2 powders in RART. For both free fall and the 50 psig pressurized release experiments, we were able to demonstrate the simulations out to 30 minutes. For the free-fall case, we estimated the ARF and compared it with the experimental data. If the agglomeration physics were included in the Fuego particle physics model, then the comparison might be better. We recommend repeating the free-fall case simulation once the particle agglomeration model is added to Fuego. In addition, the free-fall experiments as described in [Sutter 1981] contained different fall height and powder material. The additional cases should be run to substantiate the data for these experiments as well. For the pressurized release cases of [Sutter 1983], the inclusion of boundary layer entrainment and other particle forces (e.g. Van der Waal or electrostatic) may change the simulated particle interactions with the RART ceiling. To model the 250 psig pressure case, we used a number of Presto models to obtain energetic particles (kinetic energies) to be passed to Fuego simulations, so that they can be compared to the experimental data. We determined that multi-size particle models were needed in order to produce reasonable agreement with the experiments. Additional simulations are required to fine tune the multi-size particle models from Presto to Fuego in order to produce meaningful results. Therefore, it is recommended that these additional simulations be performed and that the simulations should be conducted out to 30 minutes. If the Fuego improvements, as described in Table 1-5, were added, these additional simulations could be more realistically modeled.

Fragmentation Analysis

As described in Chapter 6 of [Louie 2017], we demonstrated the ability to model the fragmentation experiment data of the Handbook. A two-scaled modeling approach was employed to address the disparate length scales involved (particles ranging in size from millimeters to microns). The two-scale model results match the impact test data reasonably well. The choice of strain rate used to initialize the micro-scale model simulations has a significant effect on the resulting particle size distribution; particularly in the particle size range of interest for safety evaluations. Results from the three rates selected do bound the test data, which is encouraging, and potentially indicates that improved results may be obtained if strain rate time-histories from the macro-scale model are used instead to define the boundary conditions for the micro-scale model simulations. Therefore, it is recommended to further develop this capability in FY2017 (Year 3).

1.3. FY2017 Tasks (Year 3)

In FY2017, as reported here, we proposed the following tasks:

- **Task 1: Develop the capability of the SIERRA/SM code to model the fragmentation experiment of a UO_2 pellet fracture using a two-scale model approach as described in Year 2.** In this capability, a microscopic 1-D model was developed to provide a way to predict finer fragments in the range of 10 microns or less. The results from this approach seem to agree well with the experimental data. To reduce the explicit coupling between the macro-scaled and micro-scaled simulations, we proposed implementing the microscopic scaled model into SIERRA/SM (Presto) as a material model in FY2017.
- **Task 2: Update Chapter 6 of the Handbook.** We proposed revising this chapter to examine more recent data in the open literature and assess the data within the Handbook. Much of the documented source terms for the nuclear criticality were from NRC regulatory guides that have been cancelled and represented the data that is not thoroughly applicable to DOE facilities and fissile material configuration at DOE sites. Task 2 supported a master thesis student from the University of New Mexico [Skinner 2017].
- **Task 3: Enhance Chapter 5 of the Handbook.** To enhance Chapter 5 of the Handbook, we proposed adding a simulation for a breach and combustion scenario involving the contents of a 55-gallon (7A) waste drum. We proposed this addition because no such data existed previously and because a drum accident occurred recently at the Waste Isolation Pilot Plant which prompted the review of any potential breach of waste drums. Using the existing drum model from the WIPP study and recent pipe over pack fire experiments conducted at SNL, a simulation using SIERRA/FM and SM codes (Aria, Fuego and Presto) was completed to predict DR, ARF and RF.

This report is divided into six chapters. The SIERRA/SM code improvement is discussed in Chapter 2, which documents both the development of the fragmentation model that includes a macroscale and microscale sub-models implemented in the code as a material model option. Chapter 3 provides a revision of Chapter 6 of the Handbook. Chapter 4 provides a development of an approach to simulate a drum fire scenario which leads to the release of contaminant from the rupture drum. Chapter 5 describes the summaries, conclusions and recommendations. Chapter 6 provides the recommendation for future efforts, including a description of the tasks to be investigated in FY2018. Appendix A provides a summary table of Handbook data. Note: the

summary table is an “in-progress” table, which means that it will be updated as more substantiating studies in this project are completed with Handbook data. Appendix B provides the proposal users guide for the models described in Chapter 2.

2. Implementation of a Micromorphic Fragmentation Model in SIERRA/SM

The work conducted for this task resulted in a new hierarchical multi-scale fragmentation model implemented within the Library of Advanced Materials for Engineering (LAME) [Scherzinger 2016] that is part of the finite element structural mechanics code SIERRA/SM [SIERRA 2017a]. The overall model combines existing independent macro and microscale fragmentation models into a single material model. The integration of the model within SIERRA/SM not only joined the existing independent fragmentation models into a single framework, but also enabled the further development of the model. As part of this development and the advantage of the scale separation, an advanced material model that features true two-way coupling between the fragmentation models at the micro and macroscales was created.

Hereafter, two fragmentation models are described (see Table 2-1). Each of these hierarchical models were used to predict the fragments that result from the impact loading of a commercially available UO_2 nuclear fuel as reported in [Louie 2016]. Understanding the fragmentation behavior of such materials is important for evaluating the risk of airborne particulate release under impact loading scenarios.

Table 2-1 Fragmentation Models

Fragmentation Model	Description
Sequentially-applied	Sequential coupled as the previous implemented model in NSRD-11 [Louie 2016]
Concurrently-coupled	The advanced two-way coupled model. This is a new model to be implemented this year.

2.1. Model Summary

The *sequentially-applied* fragmentation model consists of two independent models applied sequentially to account for the macroscale and microscale fragmentation. The model is more fully described in the final report for NSRD-11 [Louie, 2016]. The macroscale fragmentation behavior is calculated using a gradient damage explicit material model developed to model fracture in brittle materials [Lorentz 2011]. The microscale fragmentation model is an implementation of the 1-D cohesive-zone model [Zhou 2005]. In the original sequentially-applied model, the microscale model is implemented a posteriori by post-processing the macroscale data that provides initial conditions for the 1-D analysis. The microscale model is necessary to predict the resulting fragment size distribution at length scales inaccessible to the finite element based macroscale model. The full range of fragmentation behavior is then predicted by combining the results from the two independent models.

The *sequentially-coupled* approach is a newly developed model that supersedes the sequentially-applied fragmentation model. The fundamental difference between the models is in the integration into SIERRA/SM as a LAME material model. Integration allows for the results of the fragmentation model to be output with the rest of the simulation information without the need for additional post-processing (see Figure 2-1). Figure 2-1a contains a graphical description of the sequentially-coupled model that makes it clear that the microscale model only receives information from the macroscale model and no information about the state of the microscale 1-D fragmentation model is passed to the higher length scale.

The *concurrently-coupled* model employs a modified scale integration strategy to predict fragmentation. Implemented as a LAME material model in SIERRA/SM, this model involves a two-way transfer of information between both the macro and microscales. This transfer of information is graphically illustrated in Figure 2-1b and shows that the coupling occurs by continually (i) updating boundary conditions on the microscale 1-D model and (ii) passing a damage variable (energy dissipated due to cohesive zone opening) back to the macroscale model.

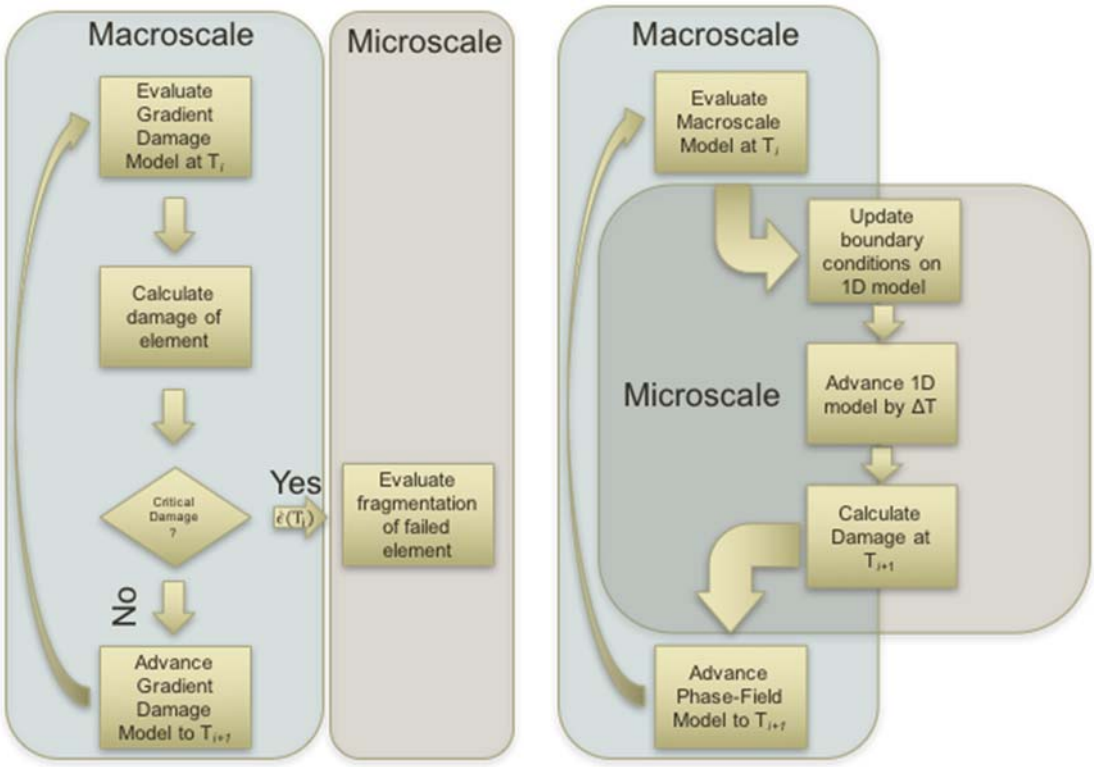

(a) Sequentially-Coupled Model **(b) Concurrently-Coupled Model**

Figure 2-1 Flowchart illustrating the design of the sequentially and concurrently-coupled fragmentation models.

2.2. Validation Data Sources

Little experimental data exists to validate the fragmentation models developed in this work. The two primary sources of measured data are those used in the Handbook, and a number of tests conducted on spent fuel by the German company Kraftwerk Union [Ruhmann 1985]. The data available is summarized in the following two sections.

2.1.1. Handbook Data

The experimental test used for validation of the original sequentially applied fragmentation model is a free-fall spill and impaction stress release case specified in the Handbook. The same experiment was used to compare the sequentially applied and integrated two-step model. In the selected test, a 10kg cylindrical steel weight was dropped onto a cylindrical ceramic uranium

dioxide (UO_2) pellet orientated on its side between two flat hardened steel plates (each about 12.5 mm thick) in a sealed container [Mecham 1981]. The lower plate was restrained from moving while the upper plate was free to translate into the pellet once struck by the falling weight. The drop height of the steel weight was selected so as to provide 1.2 J of kinetic energy per cubic centimeter of specimen material. The UO_2 pellet was comprised of three 13.7 mm diameter by 13.6 mm thick discs of commercially available nuclear fuel.

It should be noted that the actual data used in the correlation for release fraction (Eq. 4-1 in the Handbook) is taken from the Pyrex impact data [Jardin 1982].

2.1.2. Kraftwerk Union Fuel Tests

The second principle data source is from tests conducted on both unirradiated and spent fuel by the German company Kraftwerk Union [Ruhmann 1985]. These tests were conducted at substantially higher energies (two to three orders of magnitude) than those reported in the Handbook. The experimental setup was similar in that fuel was impacted by a falling weight. However, no detail about the orientation or shape of the fuel pellets was provided, nor were material properties given. The Kraftwerk data for unirradiated fuel will be used to validate the models at higher impact energies.

2.3. Sequentially-Coupled Fragmentation Model

This section introduces the new sequentially-coupled fragmentation model and details the validation of the implemented sequentially-applied model for a specific case of impact loading of a brittle material. This exercise will demonstrate consistency between both the sequentially applied and the new sequentially-coupled approaches.

As the first step, the sequentially-applied fragmentation model [Louie 2016] involves running a continuum finite element model with a gradient damage material model [Lorentz 2011]. The gradient damage model calculated the macroscopic fragmentation behavior and removed elements from the model that became fully damaged. As a post-processing step, the 1-D fragmentation model [Zhou 2005] was applied to each of the removed elements at a strain rate derived from the continuum model to predict the microscale fragmentation behavior. The model introduced in this work is the implementation of the sequentially-applied models into SIERRA/SM.

2.1.3. Macroscale Model

The ceramic pellet material was represented using an elastic gradient damage material model. Once an element is fully damaged (has near zero stiffness), it is removed from the analysis. To approximately account for real material variability, the critical fracture stress and fracture energy were varied on an element-by-element basis throughout the pellet by randomly assigning values drawn from Weibull distributions (with appropriate medians) for each parameter.

To reduce the model size and computation time, a plane-strain representation of the impact test was created. This simplification was deemed acceptable for the purposes of this validation. The steel weight, the upper and lower steel plates, and the UO_2 pellet were all included in the finite element model illustrated in Figure 2-2. The drop weight was given an initial velocity sufficient to impart an impact energy of 1.2 J per cubic centimeter to the pellet. Each component was represented using reduced integration hexahedral elements with a single integration point. In the pellet, each element extended 0.02 mm in the thickness direction of the modeled plane. A total of

about 450,000 elements were used to represent the UO_2 pellet, resulting in an in-plane element size of about 0.02 mm. The lower plate, upper plate, and drop weight were more coarsely represented using approximate element sizes of 1.0 × 1.0 × 2.0 mm. Additional details regarding the experiments may be found in [Mecham 1981, Jardine 1982] while further information about the finite element model may be found in [Louie 2016].

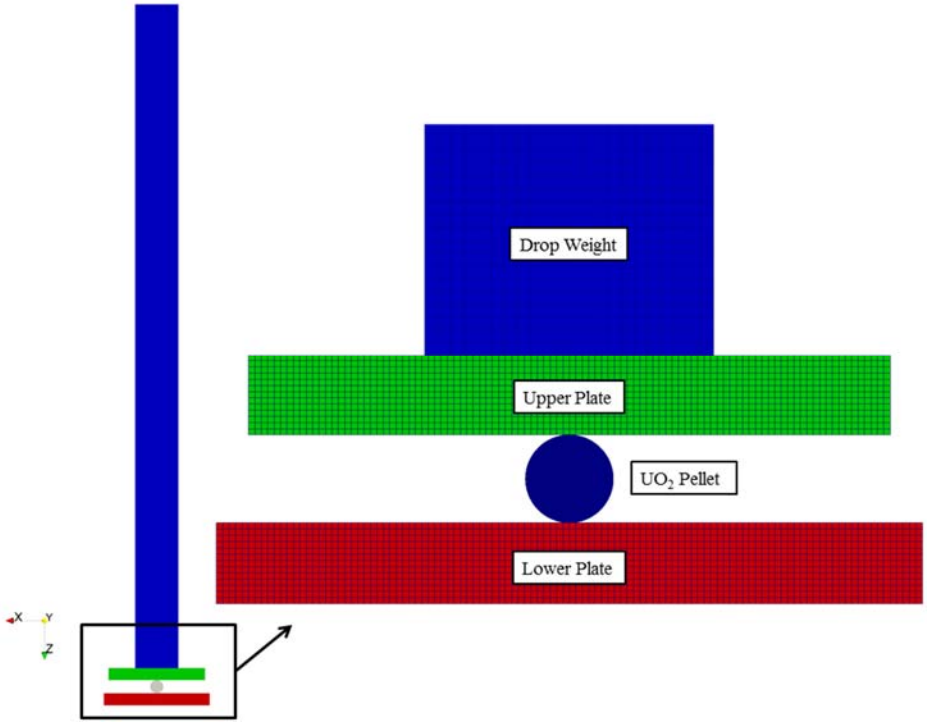

Figure 2-2 Macro-Scale Finite Element Model Mesh.

2.1.4. Microscale Model

The microscale fragmentation model is derived from the approach proposed in [Zhou 2005]. It considers the fragmentation of a 1-D bar containing defects described as equally spaced cohesive-node couples whose opening behavior is prescribed by a cohesive law. The cohesive law describing the crack growth behavior results in a linearly decaying irreversible crack opening/closing behavior. This model also allows for contact closing or reopening depending on the loading path.

When a user-specified value of damage is reached in an element, the strain rate is used as a boundary condition for the 1-D fragmentation analysis. The microscale model represents each element as a 1-D bar of length $L = 13.7$ mm, equal to the pellet diameter, containing $N = 6849$ cohesive zones that results in a minimum fragment size of 2 μm. Time evolution is described with a finite difference scheme with an integration time-step Δt taken as $\Delta t = \Delta X / v_c$, where $v_c = \sqrt{E/\rho}$ is the elastic wave speed, ΔX is the minimum fragment size (spacing of cohesive zones), and ρ is the mass density. This choice of time-step ensures that the Courant-Friedichs-Lewy condition is satisfied (Strikwerda). Material properties used in the 1-D model (elastic constants, critical fracture stress, and fracture energy) correspond to those used in the macroscale model, on an element by element (or integration point) basis so as to include variations in properties. Beside

the maximum principle strain rate, additional boundary and initial conditions are passed internally to the microscale of the integrated two-scale model. However, for purposes of validation against the sequentially applied model, the current implementation presented in this manuscript uses the initial stress condition employed by the prior model of [Louie 2016], which set the initial stress σ_0 to $0.98\sigma_c$ for strain rates $\dot{\epsilon}_{1\text{-D}} > 1000$, and $\sigma_0 = 0$ otherwise. Future improvements to the model will update the strain rate boundary condition to match the value calculated by the finite element analysis.

2.1.5. Implementation Notes

Appendix B provides complete documentation including a description of the input and available output values and instructions for using the material model within SIERRA/SM. Herein, we summarize the model's implementation to document the parameters needed to initialize the model and interpret the results. Input parameters for the code are referred to in fixed-width font.

The sequentially-coupled fragmentation model is implemented in two separate stages. First, the macroscale GDE (Gradient Damage Explicit) model is employed to calculate macroscale damage evolution in the system [Lorentz 2012]. Second, the microscale 1-D fragmentation model [Louie 2016] is applied to a bar of equivalent mass for each failed element that meets the user specified FAILURE CRITERIA for the continuum damage. Upon attaining a user specified amount of continuum damage, DAMAGE THRESHOLD, the strain rate is stored and used to initialize the 1-D fragmentation model. This parameter is used to set the thresholds for the initial and final strain rates referred to elsewhere in this documents. For the sequentially-coupled model results reported in this report, the *initial* strain rate is defined as reaching a damage value of 0.0001, and the *final* strain rate is defined as reaching a damage of 0.9999.

The GDE model is implemented within SIERRA/SM and documented elsewhere. The GDE model governs the damage evolution in the material such that the GDE calculated damage is compared with the FAILURE CRITERIA to determine which elements are removed from the system. Each failed element is divided into a number of segments with cohesive zones between them. The 1-D model is implemented using a finite difference scheme along characteristic lines as proposed [Zhou 2005]. An equivalent 1-D strain is calculated according to

$$\dot{\epsilon}_{1\text{-D}} = \dot{\epsilon}_{xx}^2 + \dot{\epsilon}_{yy}^2 + \dot{\epsilon}_{zz}^2 + 2\left(\dot{\epsilon}_{xy}^2 + \dot{\epsilon}_{yz}^2 + \dot{\epsilon}_{zx}^2\right) \qquad (2\text{-}1)$$

and stored when the GDE damage reaches DAMAGE THRESHOLD for use in the 1-D fragmentation model. The 1-D strain rate determines the velocity boundary condition applied to the end segments of the bar. Each cohesive zone is given an initial velocity based on the 1-D strain rate applied in increasing amounts from the center of the bar until reaching the velocity boundary condition at either end. The specified INITIAL MICROFRAGMENTATION STRESS FACTOR is the initial condition of stress as a fraction of the critical stress causing fracture. The initial stress is applied uniformly across the bar at each cohesive zone.

The 1-D model is run for MAX MICROFRAGMENTATION STEPS time-steps. Each time-step is equal to the time it takes for an elastic wave to propagate between two cohesive zones. The distance between the cohesive zones defines the minimum fragment size, or resolution, of the technique.

2.1.6. Validation

Three different types of validation were conducted including: a validation between the original sequentially-applied model and the superseding sequentially-coupled model, comparison to Pyrex and unirradiated UO_2 from DOE Handbook 3010, and the experiments on spent-fuel.

2.1.6.1. Model Consistency Validation

First, it must be ensured that the sequentially-applied and sequentially-coupled models produce consistent results as the implementation is the only difference between them. Both models use the same criteria for element removal, which occurs when the damage value of an element exceeds a value of 0.9999 (FAILURE CRITERIA). The results compared herein employ the *final* strain-rate value of each element. The *final* strain-rate value is the maximum strain rate reached in the element upon becoming fully damaged. The damage value at which the strain rate is recorded is determined by the DAMAGE THRESHOLD. In this case, the damage threshold is set equal to the FAILURE CRITERIA at 0.9999. The same finite element model outputs were used for each analysis with the macroscale fragmentation being illustrated in Figure 2-3. The finite element analysis found 30 macroscale fragments generated due to the removal of surrounding elements.

The macroscale fragment distributions for the sequentially-applied fragmentation model (broken red lines) and the new integrated model (solid red lines) are plotted in Figure 2-4. The mass of fully damaged elements derived from the finite-element GDE material model amounts to 8.1% of initial pellet mass. Below a fragment size of approximately $200\ \mu$m, the data in Figure 2-4 is generated solely by the microscale fragmentation model. The $200\ \mu$m limit is determined by the phase-field regularization length, a parameter of the GDE material model that is set to be approximately five times the width of an element. The validation of the sequentially-coupled model to the sequentially-applied model is conducted using the *final* strain rate to initialize the fragmentation analysis. The differences between the results of the new sequentially-coupled model (solid blue line) and sequentially-applied fragmentation model (broken blue line) predictions for the microscale cumulative mass distribution of Figure 2-4 is due to minor differences in the implementation of the 1-D fragmentation model in SIERRA/SM as a LAME material model. The details of the implementation results in slight differences between the strain rates and handling of element removal used by either model. The effect on the microscale cumulative mass distribution is negligible, but some differences are not surprising considering that the microscale fragmentation model is sensitive to the value of strain rate [Zhou 2005].

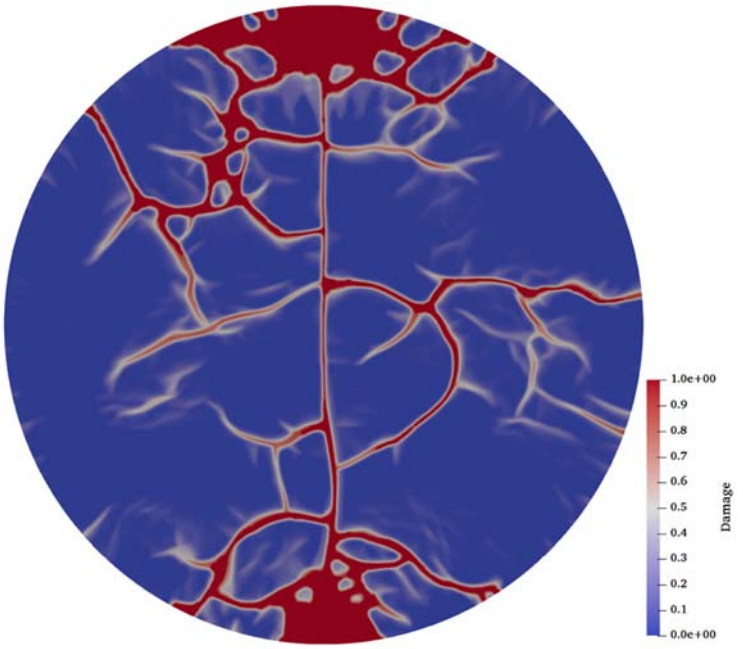

Figure 2-3 Damage to UO_2 pellet predicted by the finite-element model, 500 μs after impact. Results of the sequentially-coupled approach are provided. Degradation refers to stress degradation, with undamaged elements having a value of 1.0 and fully degraded elements having a value of 0.0.

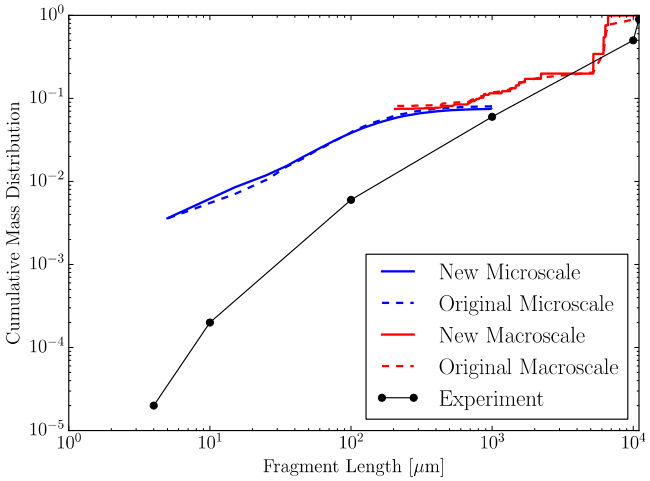

Figure 2-4 Cumulative mass distribution as a function of particle size is illustrated for the sequentially applied fragmentation model (broken lines), and the new integrated two-scale model (solid lines). Macroscale data is shown in red and microscale fragmentation data is shown in blue.

2.1.6.2. Validation with Handbook Data

The Handbook provides two primary tests for validation including impact tests of unirradiated UO_2 and Pyrex glass. Ultimately, the more extensive Pyrex glass fragmentation data was used to establish the conservative Handbook's Equation (4-1) for calculating the fraction of particles of equivalent diameter of 10 μm or less. However, for a better comparison to experimental data, the cumulative mass distribution of UO_2 impaction tests conducted by [Jardin 1982], are used for comparison and were described. Figure 2-5 plots the mass distribution from the UO_2 experiments versus the distributions obtained by using either the initial or final strain-rate conditions as defined. The material properties of the UO_2 used in the model (density $\rho = 10500\ \mathrm{kg} \cdot \mathrm{m}^{-3}$, elastic modulus $E = 137.9$ GPa, critical fracture stress $\sigma_c = 82.7$ MPa, and fracture energy $G_c = 75.0\ \mathrm{J} \cdot \mathrm{m}^{-2}$) were estimated from material test data for a related UO_2 ceramic material.

Although the results of the sequentially-coupled model plotted in Figure 2-5 do not match the experimental data below approximately 1000 μm, the model does effectively bound the experimental results by providing a high and low estimate of the cumulative mass distribution of small fragments. It should be noted that the sudden increase in cumulative mass distribution for the initial strain-rate case results from the addition of all fragments larger than 1000 μm generated by the microscale model. Figure 2-6 illustrates that the initial strain rates are typically much lower than for the final case and many elements do not fragment extensively resulting in long fragments. Due to limitations on the output of data from SIERRA/SM, only a histogram of the microscale fragments is returned rather than a record of each fragment produced. Any fragments larger than the user-set maximum bin of the histogram are automatically included in the largest bin so that their mass is not lost in the final accounting. Therefore, the step in the cumulative mass distribution is an artifact in data processing rather than a physical effect.

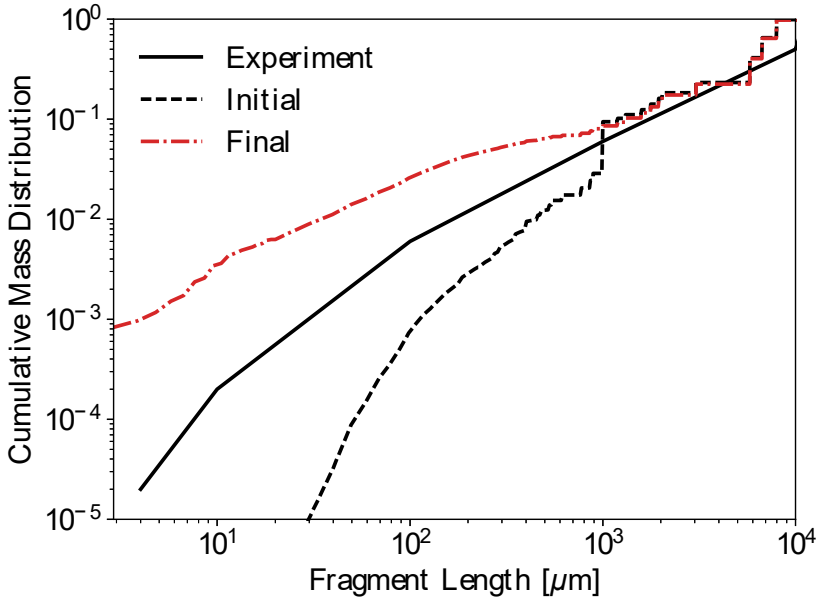

Figure 2-5 Fragment size distribution resulting from the sequentially-coupled model for impact of an unirradiated UO_2 fuel pellet experiencing an impact energy of 1.2 J/cm^3. The broken black and red lines represent using different initial strain rate selection conditions.

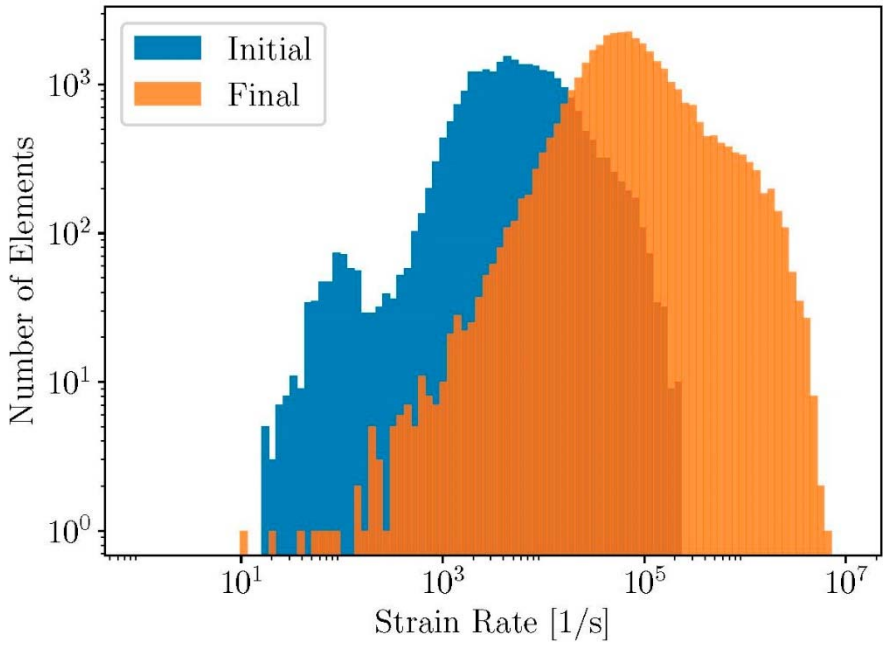

Figure 2-6 Distribution of strain rates for the sequentially-coupled model for impact of an unirradiated UO_2 fuel pellet experiencing an impact energy of 1.2 J/cm^3.

Pryex glass was also extensively tested by Jardin [Jardin 1982]. The tests were analogous to the UO_2 impact tests and were also conducted at an impact energy of 1.2 J/cm^3. The experimental (and simulation) setup was identical to that for the UO_2, except that the cylindrical sample was 12.7 mm in diameter by 60.43 mm long. Material properties of the Pyrex used in the tests were not explicitly reported in the Handbook or referenced reports, so were instead drawn from a variety of literature sources. Unless otherwise noted, data comes from the Corning Pyrex 7740 specifications. Critical stress to fracture was set to the Weibull mean $\sigma_c = 20.272$ MPa, with shape 2.20, extracted from the Weibull parameters reported [Batdorf 1978]. Elastic modulus of $E = 62.75$ GPa, fracture energy release rate [Linger 1968] of $G_c = 4.7\ \mathrm{J/m^2}$, with shape 100, stress intensity factor of $K_{1c} = 0.77\ \mathrm{MPa} \cdot \sqrt{\mathrm{m}}$, density of $\rho = 2.23{\times}10^3\ \mathrm{kg/m^3}$, with a Poisson's ratio $\nu = 0.2$.

Figure 2-7 compares the measured cumulative mass distribution to the predicted cumulative mass distribution for the Pyrex impact tests. The resulting damage to the Pyrex cylinder can be found in Figure 2-8. As expected, Pyrex is much more brittle than UO_2. Another significant difference is in the strain-rates' distribution. A significantly narrower strain-rates distribution is encountered during fracture of Pyrex (Figure 2-9) than in UO_2 (Figure 2-6), although the means are similar. Unlike the results of the UO_2 test with the same energy, the Pyrex simulation fails to predict even the macroscale fragments. There are a number of likely reasons for this failure of the model, including the lack of specification of the material properties in the original report. There is a wide range of material properties for Pyrex available in the literature and the inherent strain-rate dependence of these properties makes it difficult to choose a representative value.

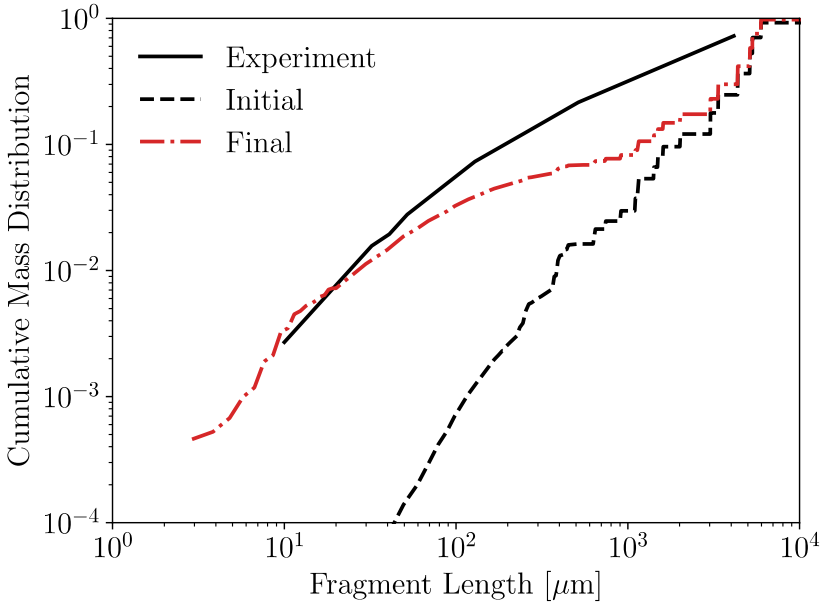

Figure 2-7 Fragment size distribution using the sequentially-coupled model on Pyrex with 1.2 J/cm^3 of impact energy. The solid line represents experimental data and the broken lines show the model predictions for the (black) initial and (red) final strain-rate cases.

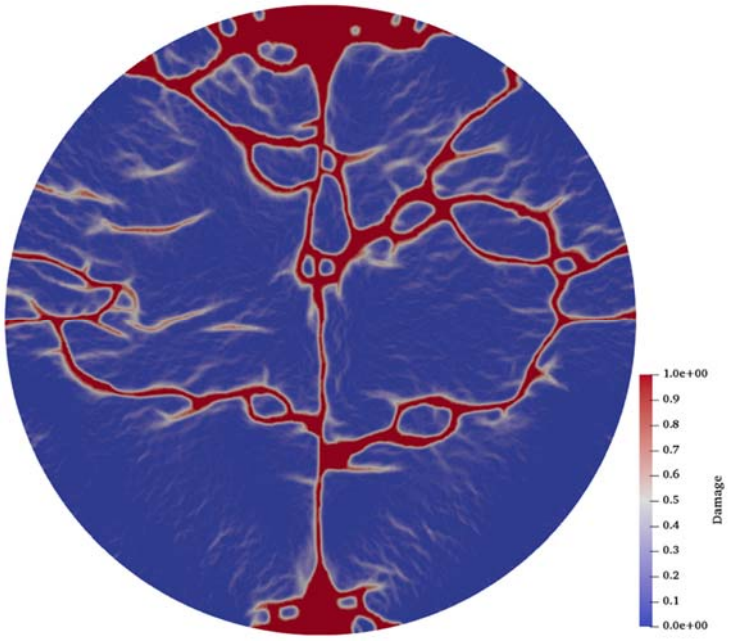

Figure 2-8 Sequentially-coupled model prediction of damage distribution of failed Pyrex test cylinder subject to 1.2 J/cm^3 of impact energy, 700 μs after impact.

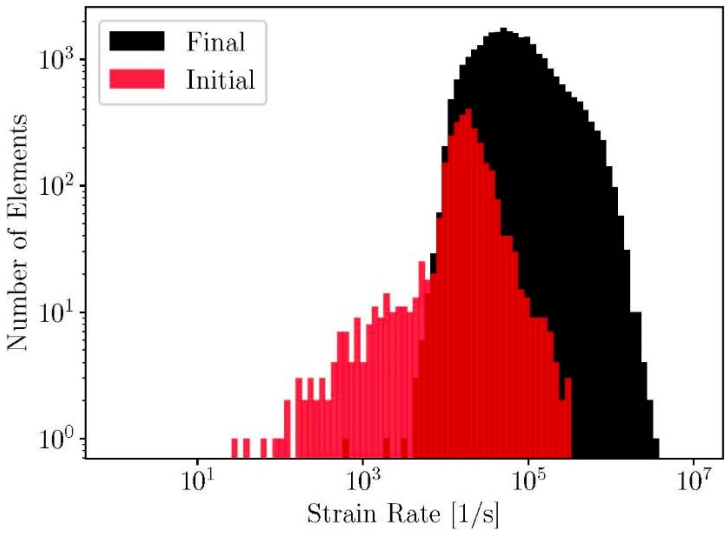

Figure 2-9 Distribution of strain rates for the sequentially-coupled model for impact of a Pyrex cylinder experiencing an impact energy of 1.2 J/cm^3.

2.1.6.3. Validation with Spent Fuel Data

The Kraftwerk Union dataset [Ruhmann 1985] provided many fragmentation cases of both fresh and used UO_2 fuel. The report did not specify the orientation or shape or material properties of the pellets used to generate the data. Although we cannot be assured that the test geometry is equivalent between the two experimental studies, the same simulation was used for both the Kraftwerk [Ruhmann 1985] and Jardin [Jardine 1982] experiment datasets. The value of the Kraftwerk dataset is in the fact that the fragmentation experiments were conducted at much higher energies than those reported by Jardin. The only parameter changed in the simulations reported in Figure 2-10 from those reported in Figure 2-5 are the impact energies.

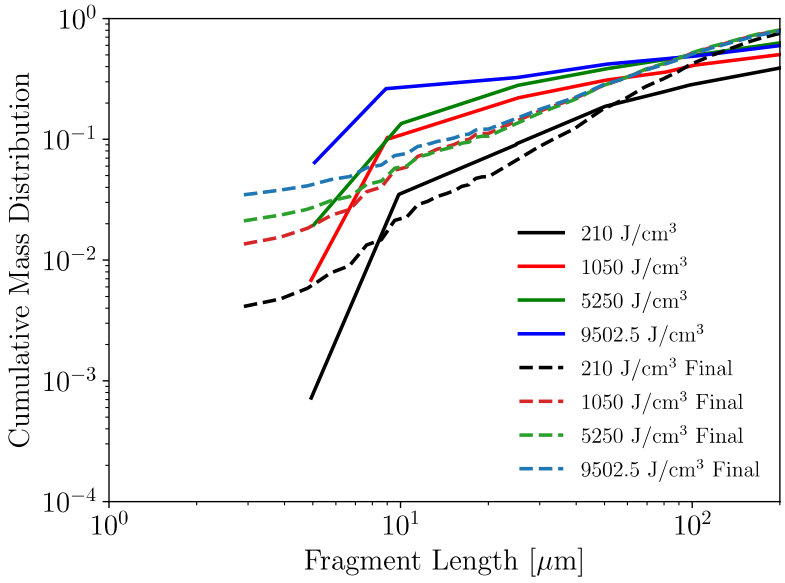

Figure 2-10 Fragment size distribution generated by the sequentially-coupled model on unirradiated UO_2 fuel, compared with data [Ruhmann 1985]. Experimental data (solid lines) are plotted with results from the microscale model initiated with the *final* strain rate (dashed lines).

2.1.7. Results and Analysis

The ability to bound the particle size distribution model with the sequentially-coupled model indicates that the modeling efforts are approximately correct, at least at long length scales. The discrepancy at lower length scales is ultimately due to the sensitivity of the fragment size distribution on the strain rate. The choice of strain rate is particularly important as a single value is applied to each element that governs the evolution throughout the simulation. The dominance of strain rate on the fragment size distribution is clearly demonstrated in Figure 2-11 after observing that the magnitude and distribution of the strain rate is only slightly modified by the differing impact energies. The primary effect of increasing impact energy is in the number of elements experiencing a given strain rate as illustrated in Figure 2-12. It is the increase in the number of elements experiencing a given strain rate that causes the cumulative mass distributions corresponding to higher impact energies to have larger values across the fragment length range as seen in Figure 2-11. The cumulative mass distribution in Figure 2-11a clearly presents a discontinuity at 1000 μm. This feature is due to the large number of elements that have fragmented by having their end elements broken off from the main body of the bar (maximum length 1000 μm). Ultimately, this artifact originates from the lower strain rates encountered using the *initial* strain-rate condition with the sequentially coupled model (compare mean values in Figure 2-12).

This sensitivity and the inability to modify the strain rate as the sample continues to fracture and deform provided the impetus for generating a model that incorporates a non-constant strain rate and provides a two-way coupling between the micro and macroscale components of the model.

.

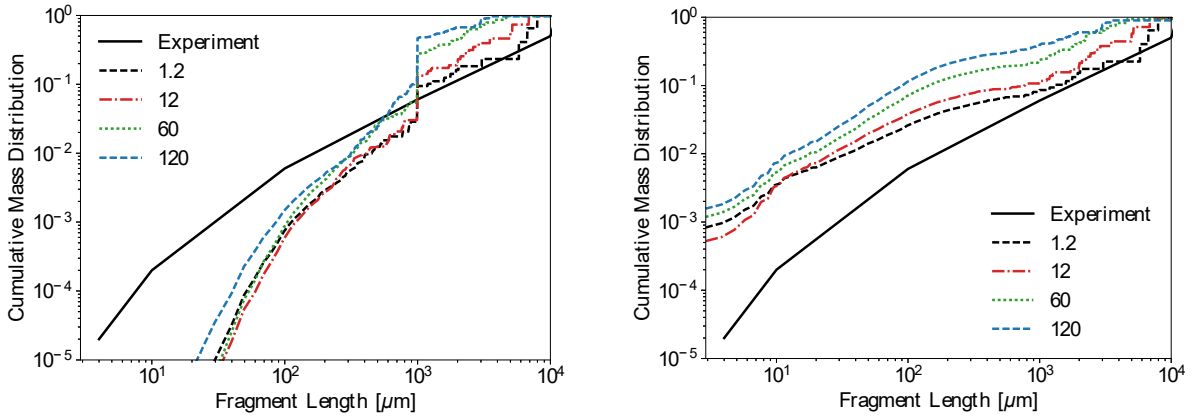

(a) Initial strain rate **(b) Final strain rate**

Figure 2-11 Effect of strain-rate condition and impact energy [J/cm³] on fragment size distribution.

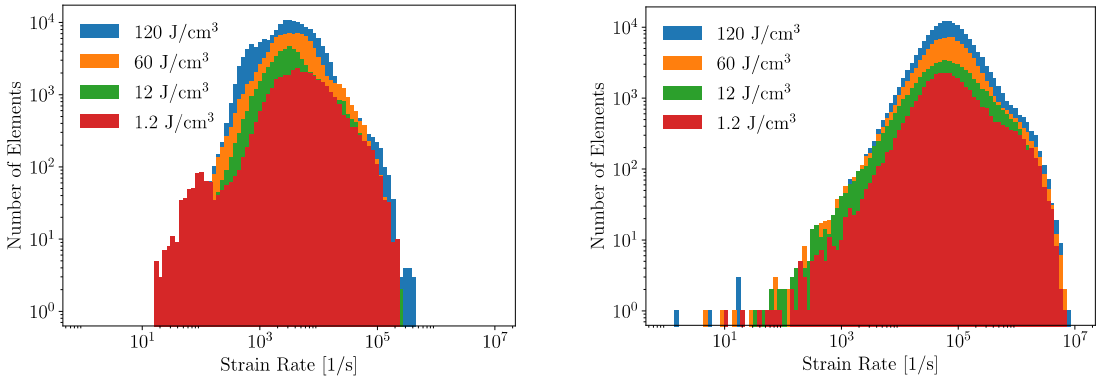

(a) Initial strain rate **(b) Final strain rate**

Figure 2-12 Effect of strain-rate condition and impact energy on values of strain rate in individual failed elements.

2.4. Concurrently-Coupled Fragmentation Model

The two-way coupled fragmentation model implemented in LAME is accessed as the material model `MicroFragmentation_Concurrent`. The material model is intended to calculate the fragmentation of brittle materials with a multiscale modeling paradigm. At the continuum length-scale, the material is described as linear-elastic with hardening and damage accounted for using SIERRA/SM's Phase-field Reaction-diffusion scheme to distribute nonlocal damage in the material; the resolution at the macroscale is limited by the length-scale inherent in the phase-field approach. The unique capability of the material model described is the ability to calculate the distribution of microscale fragments concurrently with the macroscale fragments. At the microscale, the model approximates the material as a 1-D bar in which the elasto-dynamic governing equation is solved explicitly with a finite-difference scheme. The damage calculated by

the microscale model is related to continuum damage mechanics by accounting for the energy dissipated in the opening of cohesive-zones. The length of fragments formed is defined in terms of the unit length of material defined by regularly spaced preexisting cohesive zones. These cohesive zones are able to support a load in compression after opening, but the loss in tensile strength is permanent. This model reports the resulting fragment mass distribution in the form of a histogram over a range with bin sizes specified by the user in the SIERRA/SM input file. Summary statistics (average size and standard deviation) are calculated on a per-element basis.

2.1.8. Model Description

The macroscale damage model is an implicit phase-field model implemented within SIERRA/SM and described elsewhere. A summary of the phase-field scheme is provided here for consistency of presentation. The phase-field model [Borden 2012], provides for non-local damage evolution by solving:

$$\left(\frac{4\ell\mathcal{H}(\psi_e^+)}{\Gamma}+1\right)c-4\ell^2\nabla^2 c=1, \qquad (2\text{-}2)$$

where c is the phase-field, ℓ is the nonlocal length-scale, Γ is the energy that can be dissipated by crack opening, and $\mathcal{H}$ is a history function which ensures that the 1-D undamaged extensional (positive) strain energy ψ_e^+ only increases. The phase-field has a value of 1 for undamaged material and decreases toward 0 with increasing degradation (damage) in the material. The phase-field is defined such that the damaged stress tensor is the sum of the undamaged tensile and compressive strain energies with the tensile component multiplied by the decay coefficient:

$$\sigma_{ij}=c^2\frac{\partial\psi_e^+}{\partial\epsilon_{ij}}+\frac{\partial\psi_e^-}{\partial\epsilon_{ij}}. \qquad (2\text{-}3)$$

Using a Griffith model of fracture where G_c is the fracture energy release-rate, we assume $\Gamma = G_c$. However, due to the presence of the microscale model, G_c is not equal to the energy dissipated in the model at the onset of fracture as it would be in the case of Griffith fracture. The microscale model can actually dissipate more than G_c due to the presence of multiple cohesive zones in the 1-D bar. According to Eq. 15 of [Zhou 2005], the energy dissipated in the 1-D bar due to partially opened cracks is $\sum_i D_i^2 G_c$, summed over all cohesive-zones, where the damage measure $(0 \le D_i \le 1)$ is proportional to the cohesive-zone opening displacement.

The coupling between the length-scales occurs via the energy dissipated by cohesive-zone opening at the microscale. Equation (2-2) is formulated under the premise that the energy ratio in the first term goes to unity upon meeting the condition for fracture, assuming only a single crack in each element. Due to the presence of multiple cohesive-zone crack nucleation sites, the dissipated energy exceeds G_c by $\sum_i D_i^2 G_c$. To ensure the ratio goes to 1 when any given cohesive-zone becomes fully damaged, the maximally damaged ($D_{\max} = \max D_i$) cohesive-zone energy must be removed from the total amount of dissipated energy. The total energy that may be dissipated due to fracture in Eq. (2-2) becomes

$$\Gamma = G_c\left(1+\sum_{i=1}^{N} D_i^2-\max D_i^2\right). \qquad (2\text{-}4)$$

This expression ensures that, in the case of one fully-opened (fractured) cohesive-zone, the dissipated energy is the sum of the partially opened cohesive-zone energies and G_c from the fully-opened cohesive-zone. Thus, we replace Γ in Eq. (2-2) with Eq. (2-4) so that

$$\left(\frac{4\ell\mathcal{H}(\psi_e^+)}{G_c(1+\sum_i D_i^2-\max D_i^2)}+1\right)c-4\ell^2\nabla^2 c=1. \qquad (2\text{-}5)$$

This is the phase-field equation solved implicitly during model execution. Due to the way this model was formulated by [Borden 2012], the critical stress σ_c' where the value of the phase-field and stress decrease with increasing strain is

$$\sigma_c'=\frac{9}{16}\sqrt{\frac{EG_c}{6\ell}}. \qquad (2\text{-}6)$$

For consistency between length-scales, the phase-field model's critical stress σ_c' must reach the material's critical stress σ_c used in the 1-D fragmentation model. This may be accomplished by replacing E with a modified Young's modulus $E^\star$. Substituting E for $E^\star$ and replacing σ_c' with σ_c in Eq. (2-6), and solving for the fracture length-scale ℓ, it is found that

$$\ell=\frac{27}{512}\frac{E^\star G_c}{\sigma_c^2}. \qquad (2\text{-}7)$$

Substituting the expression for ℓ into the phase-field's value of critical strain,

$$\epsilon_c'=\sqrt{\frac{G_c}{6\ell E^\star}}, \qquad (2\text{-}8)$$

it is found that, in order for the material's critical strain and stress to be related according to Hook's law ($\sigma_c=E^\star\epsilon_c$), the modified modulus must be

$$E^\star=\frac{9}{16}E. \qquad (2\text{-}9)$$

Using $E^\star$ as the modulus at the macroscale guarantees that the conditions for cohesive-zone opening at the microscale and degradation of the stress tensor will occur simultaneously.

The microscale model of fracture is identical to that used in the sequentially-coupled fragmentation model but with the boundary conditions continually updated to reflect the changing loading conditions on each element. The conditions are updated each macroscale time-step before the microscale model is executed over its smaller time-step (governed by the speed of sound and fragment resolution requested) to advance the microscale model to the next macroscale time-step. As in the sequentially-coupled model, each element contains a single instance of the 1-D microscale model. As the microscale model employs a 1-D representation of the material, the continuum state of stress must be projected onto a single dimension. The direction is chosen by recognizing that microcracks will form normal to the maximum principle stress when that stress exceeds σ_c. Upon the state of stress meeting this condition in an element, the direction of the maximum principle stress is recorded. All future crack opening must occur along the direction

recorded when the maximum principle stress first reached σ_c. The projection of the continuum state of stress is denoted as ϵ_M.

In the case of the sequentially-coupled model, the strain rate and initial stress were used as the boundary and initial conditions, respectively. In the concurrently-coupled model, these conditions are updated at each macroscale time-step and applied during the intervening microscale model execution. This hand-off between length scales must be energetically consistent. However, matching the projected macroscale strain rate $\dot{\epsilon}_M$ at the microscale does not ensure that energy is consistently transferred between length scales as will be derived below; An equivalent strain rate for the microscale model $\dot{\epsilon}_\mu$ will need to be defined. Energy conservation can be assured by matching the work done on the 1-D bar at the microscale with that of the sum of the kinetic and elastic energy.

The microscale description of work done on the 1-D bar is derived by [Zhou 2006],

$$W(t) = \int_0^t \sigma_0\,(t')v_0 dt', \qquad (2\text{-}10)$$

where σ_0 and v_0 are the stress and velocity at the left-hand end of the bar (cohesive zone 0). The time-step's 1-D velocity boundary condition is the velocity v_0 at the left-hand end of the bar is dependent on length of the bar L and the microscale strain rate $\dot{\epsilon}_\mu$. Assuming the center of the bar is fixed, the velocity-boundary condition is

$$v_0 = \dot{\epsilon}_\mu \left(-\frac{L}{2}\right). \qquad (2\text{-}11)$$

Therefore, the amount of work done is implicitly dependent on the length of the bar through the form of the velocity boundary condition. The stress term in Eq. (2-10) at the left-hand end of the bar (cohesive zone 0) is given by [Zhou 2005], and is dependent on the velocity and stress at the neighboring node (i.e. cohesive-zone 1) as

$$\sigma_0(t + \Delta t) = \sigma_1(t) - \rho v_c\big(v_0 - v_1(t)\big). \qquad (2\text{-}12)$$

Eq. (2-10) can also be expressed as the sum of the kinetic and strain-energy with respect to the macroscale model as

$$\psi = \frac{1}{2} V(\rho \dot{\epsilon}_M L + \mathrm{E}\epsilon_M^2). \qquad (2\text{-}13)$$

Substituting Eq. (2-11) into Eq. (2-10), the work done on the 1-D bar of area A is

$$W(t) = \sigma_0 v_0 A \Delta t = \dot{\epsilon}_\mu \left(-\frac{L}{2}\right) \sigma_0 A \Delta t. \qquad (2\text{-}14)$$

Equating the macro- and microscale energies from Eqs. (2-13) and (2-14) then solving for $\dot{\epsilon}_\mu$ yields

$$\dot{\epsilon}_\mu = \frac{V(\rho L \dot{\epsilon}_\mathrm{M} + E\epsilon_M^2)}{-L\sigma_0 A \Delta t}. \qquad (2\text{-}15)$$

This expression is the value of the microscale strain rate consistent with the energy dissipated in the 3-D element at the macroscale by the phase-field model.

2.1.9. Implementation Notes

This section summarizes the implemented model, including the parameters needed to initialize the model and interpret the results. Appendix B provides complete documentation with a description of the input and available output values and instructions for using the material model within SIERRA/SM.

The 1-D fragmentation model is implemented identically as in the sequentially-coupled model. The difference is in the application of initial and boundary conditions on the 1-D bar. Unlike the GDE model, the phase-field model (as implemented) has no free parameters aside from the material properties. To ensure that energy is conserved across length-scales, the mass of the 1-D bar must be identical to the material point. Therefore, each integration point (or element if each contains a single integration point) is represented by a 1-D bar with sides of length $L = \sqrt[3]{V}$, equivalent to the size of a cube with the same mass as the integration point. Each element contains $N_{\text{seg}} = L/\Delta X$ segments that are each joined by a cohesive zone described by the cohesive law specified by [Zhou 2005]. The strain energy calculated by the continuum model is used to calculate an equivalent 1-D strain, and then the equivalent microscale strain rate. The microscale strain rate from Eq. (2-15) is used to update the boundary conditions of the 1-D fragmentation model that will be run for as many microscale time-steps (based on the speed of sound and minimum fragment size) as necessary to reach the next continuum time-step.

SIERRA/SM provides the strain tensor for the present time-step to the material model: $\boldsymbol{\epsilon}_i$. The continuum stress is calculated from the continuum strain at the current time-step i without damage as $\boldsymbol{\sigma}_i = \boldsymbol{E}\boldsymbol{\epsilon}_i^{\text{e}}$. This is accomplished by directly calculating the stress from the given strain without applying the damage. The microscale model is initiated upon an element decaying to the critical value of the phase-field defined by [Borden 2012] as $c_c = \sqrt{\sigma_c/E\epsilon_c} = 3/4$. At this point, the direction of applied stress ς is stored as discussed in Section 2.4.1.

The strain applied to the microscale model is calculated at the current time-step as

$$(\epsilon_M)_i = \frac{\boldsymbol{\sigma}_i \cdot \varsigma}{E}. \tag{2-16}$$

This value of strain is the one used in Eqs. (2-13)–(2-15). The strain rate projected from the macroscale model $(\dot{\epsilon}_M)_i$ is not updated by SIERRA/SM until after the material model is invoked meaning that the strain rate is always one macroscale time-step behind. The strain rate at the current time-step $(\dot{\epsilon}_M)_i$ is therefore calculated consistent with the current macroscale strain using the prior value of the strain $(\epsilon_M)_{i-1}$ to calculate the current value of strain rate as

$$(\dot{\epsilon}_M)_i = \frac{(\epsilon_M)_i - (\epsilon_M)_{i-1}}{\Delta t}, \tag{2-17}$$

that is then used in Eqs. (2-13) and (2-15). The microscale fragmentation model then calculates the evolution of cohesive-zone opening and stress in the bar. This microscale damage in each cohesive-zone is used to calculate the value of the phase-field at the next time-step as described previously.

2.1.10. Current Limitations and Planned Improvements

The concurrently-coupled model employs a phase-field approach to alleviate mesh-dependence in the fracture behavior at the microscale. However, the present version of the model fails to accurately represent the fragmentation behavior of the pellet. This section summarizes the limitations of the current implementation of the model and discusses proposed remedies to be implemented in FY18.

2.1.10.1. Model Limitation

The most apparent limitation of the macroscale phase-field implementation is in the lack of produced macroscale fragments. Comparing the concurrently-coupled model macroscale fragmentation in Figure 2-13 to that of the sequentially-coupled model in Figure 2-3, it is apparent that the concurrently-coupled model fails to produce the expected fragmentation behavior. The concurrently-coupled model only produces a central crack with no branches, and therefore only two macroscale fragments. The generation of fewer fragments leads to reduced energy dissipation at the macroscale and greater production of fragments at the microscale, exceeding experimental results.

The phase-field model is solved implicitly for every SIERRA/SM time-step. This solution scheme is computationally intensive and results in a significant increase in code execution time compared to the sequentially-coupled model (which employs an explicit algorithm to update the phase field). Conditioning of the phase field equations sometimes results in poor solution convergence and numerical instabilities, adding to the challenges arising from inaccurate physical fragmentation behavior.

Two paths forward will be discussed and pursued simultaneously over the next year that involve improvements in both the macroscale (phase-field) model and the microscale (1-D) model. The improvements will lead to a better representation of the physics and the ability to match experimental results.

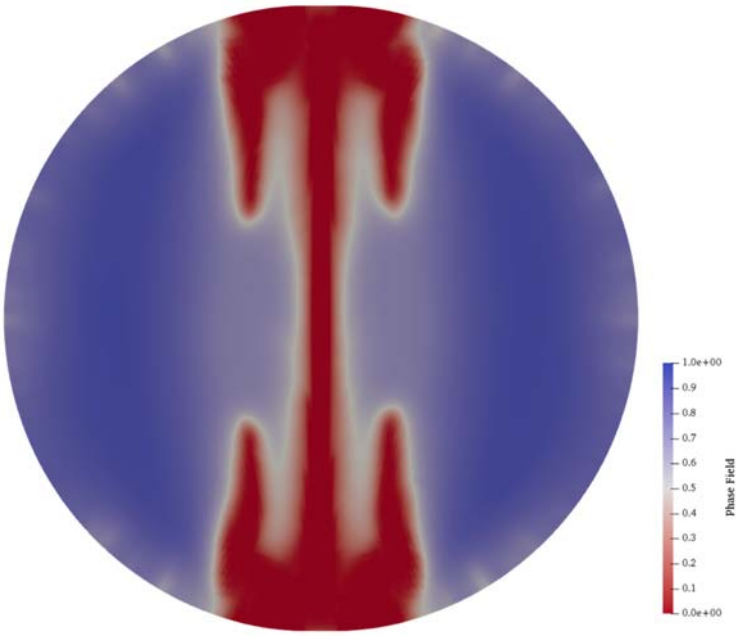

Figure 2-13 Representation of phase-field magnitude for a 1.2J/cm^3 UO_2 impact test 110 μs after impact with a mesh resolution of 0.125 mm. The phase-field currently implemented produced a single crack and only two macroscale fragments.

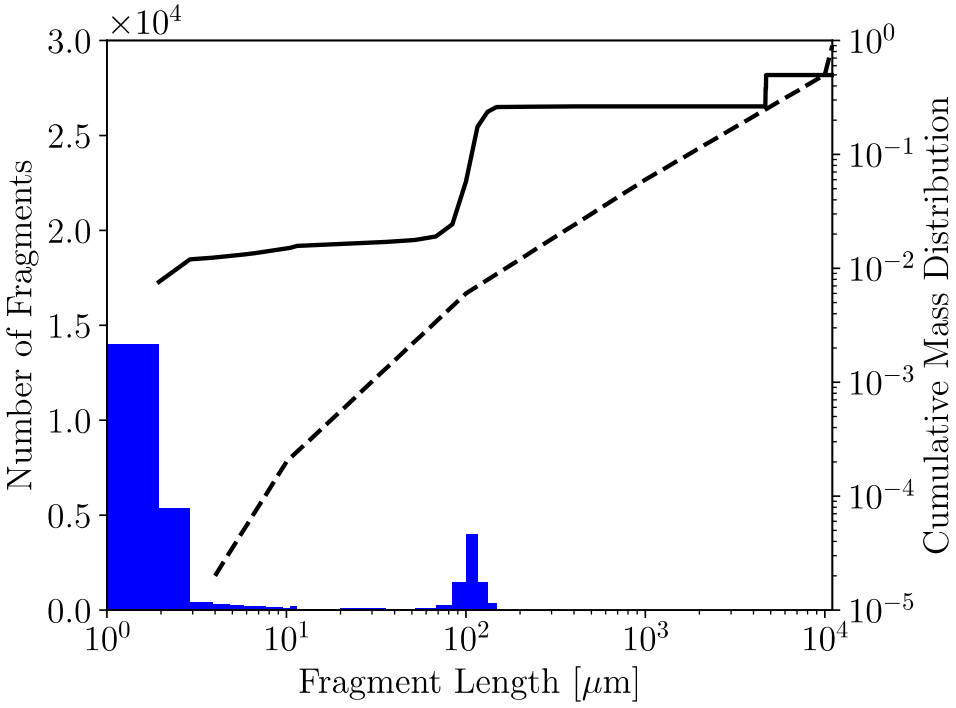

Figure 2-14 **Cumulative mass distribution determined from the concurrently-coupled model (solid line) compared with the UO_2 data of Jardin, et al. (broken line), using 0.125 mm mesh. The impact energy was 1.2 J/cm^3. The microfragment size distribution is plotted as a histogram with the hashed bar representing the cumulative number of fragments with length less than 20 *μ*m.**

2.1.10.2. Macroscale Model Improvements

There are a number of paths forward to improve the macroscale phase-field model. In FY18, we will pursue multiple paths to improve the model:

- Reformulate the phase-field model to better account for energy dissipation due to the opening of cohesive zones in the microscale model. Currently the dissipation of energy is accounted for by replacing the single continuum value for fracture energy with Eq. (2-4), that accounts for energy dissipation in cohesive zones. However, the phase-field model was not derived under the condition that the Γ term of Eq. (2-2) of could vary.
- Use a different formulation of the damage function (presently c^2) that will better reproduce linear elastic behavior before fracture. A quadratic form has been shown to better produce linear elasticity up to the critical stress [de Borst 2016] but requires an additional free parameter to be determined.
- Reformulate the model using a gradient damage approach similar to that utilized for the GDE model. This would have the added benefit requiring an implicit solve at each time-step.

2.1.10.3. Microscale Model Improvement

The model extensions described in the sections above will be provided through the implementation of a model based on the mechanics of generalized continua (also referred to as micromorphic model) in order to incorporate some effects of the characteristic lengths of the materials microstructure. The idea here is to endow the continuum with additional degrees of freedom that are supposedly independent from the usual translational degrees of freedom and representative of the microstructure [Forest 2006].

Within this paradigm in the microscale model presented in Section 2.1.4, the classical wave propagation equation that is used will be replaced by a micromorphic formulation. The adopted formulation accounts for the microstructural features complemented by an elastic model both at the 1-D bar and microstructural level.

Following [Dingreville 2014], the 1-D bar will be considered as a deformable continuous distribution of material points, each of them being geometrically represented by a point M and characterized kinematically by macroscopic (bar-level) and microscopic (microstructure-level) displacement fields. The 1-D bar displacement field u is defined classically based on the coordinates in the undeformed and deformed reference state, while the microdisplacement u' is defined by the coordinates of a point M' belonging to a microvolume around point M and measured from the center of mass of this microvolume.

In this context, the fundamental balance laws for a so-called microstructured materials are now defined both at the macroscopic (1-D bar) and microscopic (underlying microstructure) scale, such that the resulting equation of motion read:

$$\rho u_{tt} - \sigma_x = 0 \tag{2-18}$$

$$I_\mu \chi_{tt} - \mu_x + \eta = 0 \tag{2-19}$$

with σ defined as the macrostress (Piola stress), η is the interactive microforce, and μ the microstress (also referred to as the coupled stress). The symbol ρ denotes the macroscopic materials density and I_μ is the micro-inertia associated with the microvolune around the material point M. Subscripts in x and t denote the partial derivative with respect to space and time respectively. For example, μ_x denotes the first derivative of μ with respect to *x*, or u_{tt} denotes the second partial derivative of u with respect to *t*.

If we assume that the micromorphic medium is linear elastic, and defining the macroscopic velocity as $v = u_t$, the resulting wave equation for the 1-D micromorphic bar is given by,

$$\frac{c_{0\mu}^2}{c^4} v_{tt} = \left(1 - \frac{c_{0\mu}^2}{c^2}\right) v_{xx} - c_\mu^2 \tau^2 v_{xxxx} \tag{2-20}$$

where the characteristic velocities are defined as,

$$c_0^2 = \frac{E_0 + 2A_{0\mu} + B_{0\mu}}{\rho}\ , c_{0\mu}^2 = \frac{\left(A_{0\mu} + B_{0\mu}\right)^2}{\rho B_{0\mu}}\ , c_\mu^2 = \frac{E_\mu}{I_\mu} \tag{2-21}$$

and the characteristic microstructural time is given by,

$$\tau^2 = \frac{I_\mu}{B_{0\mu}} \tag{2-22}$$

The materials constant E_0, $A_{0\mu}$, $B_{0\mu}$ and E_μ defined the constitutive behavior both at the macro and micro-scale [Dingreville 2014]. Equation (2-20) is the 1-D equation that will replace the one used in Section 2.1.4. The material constant E_0 and E_μ are Young's modulus at the macro-scale and micro-scale respectively, and $A_{0\mu}$ and $B_{0\mu}$ are coupling materials constants

2.5. Summary and Conclusion

The fragmentation modeling task has developed two new modeling and analysis capabilities that will lead to better predictions of airborne particle releases during the impact or free-fall of ceramic fuel forms. These new capabilities enable the characterization of the final state of fragmentation (in terms of size and distribution of fragments) as a function of the materials properties, the energetic loading conditions and the intrinsic length scale associated with fragmentation (through scale separation with both the macro- and micro-scale models).

This novel hierarchical fragmentation modeling capability leveraged prior investments made by SNL in both fracture mechanics and in fine scale models to predict and better characterize fracture in structural analysis and was implemented within SIERRA/SM. The model exercised is a two-scale model simulating a weight dropped on a cylindrical ceramic specimen to predict the fragment size distribution under various boundary conditions. At the macroscale, the model uses a phase field formulation implanted in SNL legacy solid mechanics tools to simulate the dynamic fracture of the cylinder. Results from the macroscopic calculations are then passed (either concurrently or sequentially) to a one-dimensional lower length scale model that captures fine scale effects. This 1-D paradigm models the internal crack nucleation and opening process to predict the average fragment size and the fragment size distribution as a function of the materials properties, loading conditions. The implementation of the approach into a LAME material model in the SIERRA/SM code is particularly promising because it enables the direct inclusion of a two-way coupling between the micro- and macro- length-scale models. This coupling allows for a continuous update

of the fragmentation boundary conditions and on the fly characterization of the fragmentation at both scales.

This capability has been compared and validated with prior-year more simplistic sequential fragmentation model for consistency. After this first validation step, this hierarchical fragmentation model has been exercised to examine solid fragmentation in the case of an impaction experiment on unirradiated UO_2 fuel from ANL-82-39 referenced in Section 4.3.3 of the Handbook (for lower impact energies) and German tests conducted on spent fuel (for higher impact energies) as a validation of the implementation and later extended to other ceramic materials (Pyrex). Results of the sequentially-coupled fragmentation model against the Handbook impact tests on unirradiated UO_2 shows that the model bounds the experimental particle size distribution model relatively well, indicating that the modeling efforts are correctly capturing the fragmentation physical phenomena. However, the discrepancy observed at lower length scales points to certain limitations in the current state of the model. Notably, the sensitivity of the fragment size distribution on the strain rate boundary conditions in the microscale model necessitate a more careful handling of the two-way coupling between both scales. Additionally, the disagreement between the experimental fragmentation characterization and modeling prediction for Pyrex points to the fact that the inherent strain rate dependence of various materials properties used in the model is warranted for predictability over a wide range of material systems. The newly developed and implemented concurrently-coupled model allows for the continuous update of the microscale fragmentation model boundary conditions such as strain rate. This change is intended to allow the microscale fragmentation model to better reproduce the experimentally observed distribution of fragment sizes. However, the concurrently–coupled model is presently not reproducing experimental results, but a clear path forward is outlined to remedy the situation in the coming year with proposed solutions as described in Chapter 6 of this report.

In conclusion, the primary achievements made during this fiscal year and detailed in this report are:

- Implementation of the prior-year sequentially-coupled fragmentation model as a LAME material model within SIERRA/SM entitled *MicroFragmentation_Sequential*.
- Validation of the results of the sequentially-coupled model against the prior-year sequentially-applied model to show consistent behavior of the model.
- Comparison of the results of the sequentially-coupled model to two sets of experiments conducted by different entities on unirradiated UO_2 fuel and Pyrex borosilicate glass.
- Discussion of the weaknesses of the sequentially-coupled model and the aspects of a new model that are needed to overcome the limitations of the model.
- Development and implementation of a new concurrently-coupled fragmentation model within LAME entitled *MicroFragmentation_Concurrent.*
- Identification of the limitations of the concurrently-coupled model and outlined pathways to remediate the model.

3. Revision of Chapter 6 of DOE-HDBK-3010

Under appropriate accident conditions, fissile and fissionable radionuclides may undergo a self-sustaining nuclear reaction (chain reaction) called an inadvertent nuclear criticality. The initial airborne release from a nuclear criticality is estimated by use of relevant factors of the five-component linear equation used to estimate the airborne release from other events covered in the Handbook. However, because the evaluation of nuclear excursions is a complex process, some additional topics used in the equation are discussed below. Much of the information provided in this chapter can be found in a recent published master thesis [Skinner 2017].

3.1. Summary of Bounding Release Estimates

For nuclear criticalities, the Material-at-Risk (MAR) is determined by the fraction of fission products generated by the criticality and the fraction of the fissile/fissionable material that may be suspended by the event-generated conditions (primarily heat) [Note: since fissile materials (^{233}U, ^{235}U, ^{239}Pu) are also fissionable, the term fissionable will be used to refer to both fissile and fissionable materials]. The amount of fission products and actinides produced by the excursion is a function of the total fissions from the criticality and the specific fissionable radionuclide involved. The fraction that is at risk of airborne suspension depends upon the physical form of the fissionable materials involved. Estimation of fission product quantities can be done with computer codes, or by simple ratios (total fissions for scenario/reference fission yield for process type) to values from generic models as discussed in this chapter. The generic models are based on a review of historical criticality accidents and provide values replacing those in the previous edition of the Handbook.

The airborne release from nuclear excursions in various physical systems can be estimated for general purposes using the equations which follow. Unless otherwise noted, all respirable fractions are equal to 1.0 and are not specifically mentioned. The physical systems considered are: (1a) solutions in open containers; (1b) solutions in closed containers; (2) fully moderated/reflected solids; (3) bare, dry solids; and (4) large storage arrays. Fission yield estimates are based on bounding evaluations of historical process criticality accidents. Worldwide, there have been 22 process criticality accidents to date with nine fatalities. None of these has resulted in any significant mechanical energy release, and radiation exposure has been the only significant hazard. From criticality accidents to date, significant doses have only been received by workers in proximity to the accident site. Other facility workers, the public, and the environment have received insignificant exposures.

“There is a significant amount of available excursion data relevant to understanding the magnitudes of potential process criticality accidents” [McLaughlin 2003]. Rather than using scarce resources on speculative consequence modeling, meaningful enhancements in criticality safety are more appropriately accomplished through application of bounding data from historical excursions and implementation of required criticality safety evaluations in accordance with guidelines such as DOE-STD-3007-2007, “Guidelines for Preparing Criticality Safety Evaluations at Department of Energy Non-Reactor Nuclear Facilities” [DOE 2007].

Note that since this section is intended to summarize the bounding values based on the subsequent sections in this chapter, the appearance of these tables are not called out accordingly here.

3.1.1. Solutions

Solutions refers to fissile materials dissolved in a liquid solvent, typically aqueous acid solutions. The release of volatile radionuclides generated by the criticality is evaluated separately from the release of non-volatiles and fissile material originally present in the solution. For open containers or closed systems with connected piping, the criticality is assumed to be a single pulse with total fissions equal to 1×10^{15} fissions per liter of fissile solution in the container [Barbry 1987, McLaughlin 2003, ANS-8.23 2007]. The duration of the pulse is assumed to be 0.2 seconds, and the radionuclide activities are calculated at 10 and 60 minutes after the termination of the pulse. The shutdown mechanism in these excursions has been ejection of solution either into the room or back into the process piping.

For closed containers or systems where solution is not easily ejected, the criticality is assumed to consist of multiple pulses with an upper bound of 1.6×10^{16} fissions per liter based on results from solution criticality experiments [Barbry 1987, McLaughlin 2003, ANS-8.23 2007]. The total fissions were assumed to be over a 10-minute period, and the radionuclide activities are calculated at 10 minutes and 60 minutes after the termination of the excursion. The criticality may be terminated by dilution, mixing, evaporation of up to 50% of the solution, or by human intervention (e.g., the addition of neutron poison, tank draining).

Three of the accidents (Hanford 1964, Novosibirsk 1997, and Tokaimura 1999) continued for many hours. There were no experiments where the excursion continued for less than an hour. Based on these three accidents, it is estimated that the ratio of total fissions (over an 8-hour period) to first spike yield for these "slow cooker" excursions is about 30. The total specific fission yield was assumed to be 3×10^{16} fissions per liter, and the radionuclide activities are calculated at 1 hour, 2 hours, 3 hours, 4 hours, 5 hours, 6 hours, 7 hours, and 8 hours during the evolution of the excursion.

$$\text{Airborne Source Term} = (MAR_{c1}\times DR_{c1}\times ARF_{c1}) + (MAR_{s1}\times DR_{s1}\times ARF_{s1}) \qquad (3\text{-}1)$$

where:

MAR_{c1} = Inventory of gas and volatile (i.e., iodine) radionuclides generated from criticality in a solution based on liters of solution / 100 liters times values for Uranium Solutions in Table 3-7, Table 3-8, or Table 3-9; or times values for Plutonium Solutions in Table 3-10, Table 3-11, or Table 3-12 as appropriate for the excursion type, Curies.

DR_{c1} = Damage Ratio for gases and volatiles (i.e., iodine) generated in criticality, 1.0.

ARF_{c1} = Airborne Release Fractions for solution criticality drawn from (Table 3-7 through Table 3-12 as appropriate).

MAR_{s1} = Inventory of non-volatile fission products generated and radionuclides in solution prior to the nuclear excursion evaporated, Curies.

DR_{s1} = Damage Ratio of non-volatile fission products in solution, 1.0.

ARF_{s1} = Airborne Release Fractions for non-volatile fission products. 1×10^{-2} for ruthenium isotopes in fuel reprocessing solutions and based on accident experience and experiments, this value is zero for all other non-volatile fission products except short-lived bromine isotopes.

3.1.2. Fully Moderated/Reflected Solids

This configuration covers reflected bulk metal and metal pieces or solid fines, such as powders, that are moderated or reflected. The equation assumes some softening and local deformation of metals to allow fission product release, but no severe molten eructation, reactions, or vaporizations are considered credible for the configuration due to the limited time of the excursion and the significant heat transfer occurring to the moderator. The moderator and/or reflector typically assumed is water. A coherent solid cannot be moderated and solids < 100 μm in diameter must be intimately mixed with the moderator to be fully moderated. Excursions in these systems are assumed to be bounded by the fission values from solution systems. As there are no historical criticality accidents involving these configurations, the ARF values are assumed to be bounded by those spent fuel experiment [NUREG 1997]. Specific MAR values for fully moderated/reflected solids should be calculated using ORIGEN or other code systems.

Only one process criticality accident has involved solid metal with some reflection; this was the assembly of 4 pieces of plutonium metal. There was a single burst of 3×10^{15} fissions, followed by either intentional or mechanical disassembly of the configuration. There was no melting or deformation of the metal units. Although this was the only metal accident, and there are no plutonium metal experiments to provide a basis for comparison, the two Los Alamos critical accidents with a reflected plutonium metal sphere (1945 and 1946) exhibit similar specific spike yields.

$$\text{Airborne Source Term} = (MAR_{c2}\times DR_{c2}\times ARF_{c2}) \qquad (3\text{-}2)$$

where:

MAR_{c2} = Inventory of fissionable material and radionuclides from criticality in water reflected/moderated solids either from Table 3-7 or Table 3-10, or calculated by computer code systems such as ORIGEN.

DR_{c2} = Damage Ratio for radionuclides generated by criticality: metal pieces, 0.1 fines, (e.g., powders), 1.0.

ARF_{c2} = Airborne Release Fraction: fissionable material and non-volatile fission products can be neglected, Table 3-15 provides ARF values for Single Spike Excursions as might be hypothetically possible in fully water moderated/reflected metal systems. ARF values are given in Table 3-15 for a lesser spike followed by a delayed supercritical excursion over time.

3.1.3. Bare, Dry Solids and Large Storage Arrays

This configuration covers solids (e.g., metal fines, loose oxide powders) that may be reflected but have no moderation (i.e., not immersed in liquid). There is no accident data for such systems dominated by fast neutron fissions. For large storage arrays, it should be easy to protect against an accident by appropriately packaging individual items. For both of these fissile forms, the past criticality safety evaluations have been able to document no credible accident sequences, and it is expected that this will continue in the future.

3.1.3.1. Large Storage Arrays

This configuration deals with driving together large amounts of material by external forces (i.e., reactor fuel storage arrays, extremely large quantities of fissionable materials). The total fission

yield of 1×10^{20} is based on historical reactor excursions with moderation, and was originally developed in the Defense Programs Safety Survey solely for the purpose of evaluating criticalities in spent fuel storage pools when fuel was driven together. However, issues related to criticality and potential extreme excursions in storage environments are most appropriately handled in the arena of criticality safety evaluations performed by criticality safety professionals for the purpose of minimizing chances of occurrence. Design considerations relating to these issues should not be driven by unrealistic dose calculations from unattainable accident scenarios.

3.2. Total Fission Yield

The potential releases from criticality events are directly related to the total fission yield of the event. This section provides historical and analytical information relating to fission yields to assess bounding values.

3.1.4. Historical Excursions

To provide some perspective on the types of situation that have resulted in excursions in the past, lists compiled by various authors of the excursions that have actually taken place are presented. Several incidents are listed in multiple tables due to the diverse nature of sources used.

Stratton [Stratton 1967] reviewed information on 34 excursions that occurred between 1945 and 1965. Seven additional accidents were added in a revision by Smith [Smith 1989]. The material from both Stratton [Stratton 1967] and Smith [Smith 1989] was incorporated into the 2000 Revision of *A Review of Criticality Accidents* by McLaughlin et al. Of the 48 excursions in homogeneous systems, 5 occurred in Solution Experiments, 21 occurred in Solution Processing, 15 in Metal Experiments, 1 in Metal Processing, and 6 in Miscellaneous Experimental Systems. There were also 8 excursions in Inhomogeneous Water Moderated Systems, and 4 excursions in Inhomogeneous Heavy Water Moderated Systems.

Olsen et al. [Olsen 1974] reviewed Stratton's excursion data and experimental data from the French study Consequences Radiologiques d'un Accident de Criticite (CRAC). Material from Olsen [Olsen 1974] and McLaughlin et al. [McLaughlin 2000] is incorporated into Table 3-1 and Table 3-2 where the excursions are listed by system type. The total fission yield of the 26 excursions involving fissile solution ranges from 1×10^{15} to 4×10^{19} fissions. All but one is bounded by a total fission yield of 1.3×10^{18} fissions. The 16 excursions involving metal systems (including some reflection) range from ~ 3×10^{15} to 1×10^{19}fissions. All but one is bounded by a yield of 1×10^{18} total fissions. Only 6 excursions are listed for miscellaneous moderated foil and powder systems with total fission yield listed for only 4 excursions (~ 6×10^{15} to 4×10^{16} total fissions). Excursions in reactor and reactor experiments are incorporated into Table 3-1 and Table 3-2. A value of 1×10^{20} (rounding the coefficient to a single digit) bounds the reported values and may be considered partially representative of excursions that may occur in an array. For those accidents that destroyed the experimental apparatus, Table 3-3 provides information on Total Energy Release, Maximum Energy Density, Maximum Temperature and Maximum Pressure of the accident [Nyer 1965].

Table 3-1 Summary of Known Accidental Criticality Excursions (1945 to 2016) [Olsen 1974, McLaughlin 2000, USAEC 1975]

a) Solution Systems
b) Metal Systems
c) Miscellaneous Systems

a) Solution Systems										
Solution Experiments (SE xx)										
No.	**Date**	**Location**	**Title for Ref.**	**Fissionable Material**	**Arrangement**	**Initial Prompt Critical Burst, Fissions**	**Duration**	**Total Fissions**	**Cause**	**Physical Damage**
Open Systems										
SE 3	5/26/1954	ORNL - Oak Ridge , TN	Spider	UO_2F_2 (18.3 kg U235; 55.4 l)	Cylindrical annulus, unreflected	5.1×10^{16}	< 1 min.	1×10^{17}	Shift of poison	None
SE 4	2/1/1956	ORNL - Oak Ridge , TN	Scram blade	UO_2F_2 (27.7 kg U235; 58.9 l)	Cylinder, unreflected	1.6×10^{17}	Single burst, < 1 min.	1.6×10^{17}	Geometry change	Warping of bottom of cylinder
SE 5	1/30/1968	ORNL - Oak Ridge , TN	U-233	$UO_2(NO_3)_2$ (0.95 kg U233; 5.8 l)	Sphere, water-reflected	1.1×10^{16}	Single burst, < 1 min.	1.1×10^{16}	Air in line; solution surged from safe to unsafe geometry	None
Closed Systems										
SE 1	12/1/1949	LASL - Los Alamos, NM	Water Boiler	$U(93)O_2(NO_3)_2$ (about 1 kg U235; 13.6 l)	Sphere, graphite-reflected	$\approx 3 \times 10^{15}$ (about 3 cents above prompt critical)	< 1 min.	$3\text{-}4 \times 10^{16}$	Control rods withdrawn too fast	None
SE 2	11/16/1951	Hanford Works - Richland, WA	P-11	$PuO_2(NO_3)_2$ (1.15 kg Pu; 63.8 l)	Sphere, 93% full reflected	8×10^{16}	Single burst, < 1 min.	8×10^{16}	Cadmium rod removed too rapidly	None

Table 3-1 Summary of Known Accidental Criticality Excursions (continued)

Solution Processing Accidents (SP xx)										
No.	**Date**	**Location**	**Title for Ref.**	**Fissionable Material**	**Arrangement**	**Initial Prompt Critical Burst, Fissions**	**Duration**	**Total Fissions**	**Cause**	**Physical Damage**
Open Systems										
SP 2	4/21/1957	Mayak Production Association	Solution	$U(90)O_2C_2O_4$ precipitate solution (3.06 kg U-235; 30.0 l)	Cylinder, unreflected	1×10^{17}	10 min.	$\sim 1 \times 10^{17}$	Uranium accumulation in receiving vessel	None
SP 3	1/2/1958	Mayak Production Association	Solution	U(90) uranyl nitrate (22.0 kg U-235; 58.4 l)	Cylinder, unreflected	$\sim 2 \times 10^{17}$	Single burst, < 1 min.	$\sim 2 \times 10^{17}$	Vessel manually moved, shifting fluid	Contamination of experimental facility
SP 4	6/16/1958	ORNL, TN - Y-12 Processing Plant	Y-12	$U(93)O_2(NO_3)_2$ (2.10 kg U-235; 56 l)	Cylinder, concrete reflected below	$\approx 1 \times 10^{16}$	20 min.	1.3×10^{18}	Valve leaked or left open	None (loss: $1000)
SP 14	7/24/1964	Wood River Junction, RI - scrap recovery facility	Wood River	$U(93)O_2(NO_3)_2$ (2.07 kg U235, 41 l)	Cylinder, unreflected	1.1×10^{17}	1 hr. 30 min.	1.3×10^{17}	Procedure not followed	None
SP 17	12/10/1968	Mayak Production Association	Solution	Aqueous and organic Pu solutions (~1.589 kg Pu; 1.50 Pu-239; 28.8 l)	Cylinder, unreflected	3×10^{16}	Two excursions (75 min.), third caused by error	3.5×10^{16} (two), $\sim 1.3 \times 10^{17}$ (final)	Additional organic plutonium solution in vessel (changes in piping)	Contamination of experimental facility

Table 3-1 Summary of Known Accidental Criticality Excursions (continued)

No.	Date	Location	Title for Ref.	Fissionable Material	Arrangement	Initial Prompt Critical Burst, Fissions	Duration	Total Fissions	Cause	Physical Damage
Solution Processing Accidents - Closed Systems										
SP 1	3/15/1953	Mayak Production Association	Solution	Pu nitrate solution (0.842 kg Pu; 0.81 kg Pu-239; 31.0 l)	Cylinder, surrounded by cast iron	~ 2×10^{17}	Single burst, < 1 min.	~ 2×10^{17}	Too much material transferred to container	None
SP 5	12/30/1958	LASL, NM - Pu Processing Plant	Agitator	$PuO_2(NO_3)_2$ (3.27 kg Pu; 2.94 kg Pu-239; 160 l)	Cylinder, water-reflected below	1.5×10^{17}	Single burst, < 1 min.	1.5×10^{17}	Procedure not followed; agitator created critical geometry	None (Tank displaced about 10 mm)
SP 6	10/16/1959	Idaho Reactor Testing Area, Chemical Processing Plant	IF-1 (siphon)	$U(91)O_2(NO_3)_2$ (34.5 kg U235; 800 l)	Cylinder, concrete reflected below (approximated slab)	≈ 10^{17}	20 min.	≈ 4×10^{19}	Sparge gauge plugged, solution surged from safe to unsafe geometry	None (loss: $61,800 to recover contam. solution). Airborne FPs through venting.
SP 7	12/5/1960	Mayak Production Association	Solution	Pu carbonate solution (1.003 kg Pu; 0.85 kg Pu-239; 19 l)	Cylinder, concrete reflected below	Not known	1 hr. 50 min.	2.5×10^{17}	Mass limit of container deliberately exceeded	None
SP 8	1/25/1961	Idaho Reactor Testing Area, Chemical Processing Plant	IF-11 (air lift)	$U(90)O_2(NO_3)_2$ (7.2 kg U235; 40 l)	Cylinder, unreflected	6×10^{16}	< 3 min.	6×10^{17}	Instruction misinterpreted, solution pumped from safe to unsafe geometry	None (loss: $6000). Early Airborne FPs
SP 9	7/14/1961	Siberian Chemical Combine	Solution	$U(22.6)F_6$ accumulated in oil (1.68 kg U-235; 42.95 l)	Cylinder, unreflected	~ 2×10^{14}	Two distinct events, < 1 min.	~ 1.2×10^{15}	UF_6 accumulation in vacuum pump oil	None
SP 10	4/7/1962	Hanford Works - Richland, WA	Recuplex	Pu complex (1.5 kg Pu; 1.29 kg Pu-239; 45 l)	Cylinder, unreflected	≈ 10^{16}	37.5 hrs.	8×10^{17}	Valve leaked or opened; solution overflow down unsafe geometry	None (loss: $1000)
SP 11	9/7/1962	Mayak Production Association	Solution	Pu nitrate solution (1.324 kg Pu; 1.26 kg Pu-239; 80.0 l)	Cylinder, water-reflected	Not known	Three excursions, 1 hr. 40 min.	2×10^{17}	Incomplete dissolution in vessel	Minor contamination of facility
SP 12	1/30/1963	Siberian Chemical Combine	Solution	U(90) uranyl nitrate (2.27 kg U-235; 35.5 l)	Cylinder, unreflected	Not known	10 hrs. 20 min.	7.9×10^{17}	Error in recording uranium content	None

Table 3-1 Summary of Known Accidental Criticality Excursions (continued)

No.	Date	Location	Title for Ref.	Fissionable Material	Arrangement	Initial Prompt Critical Burst, Fissions	Duration	Total Fissions	Cause	Physical Damage
Solution Processing Accidents - Closed Systems (continued)										
SP 13	12/2/1963	Siberian Chemical Combine	Solution	U(90) organic solution (1.93 kg U-235; 64.8 l)	Cylinder with hemispherical bottom, unreflected	Not known	16 hrs.	6×10^{16}	Insufficient detection leading to buildup of fissile	None
SP 15	11/3/1965	Electrostal Machine Building Plant	Solution	U(6.5) oxide slurry (3.65 kg U-235; 100.0 l)	Cylinder, unreflected	~ 1×10^{16}	Single burst, < 1 min.	~ 1×10^{16}	Uranium oxide accumulation in vacuum system, no filtration	None
SP 16	12/16/1965	Mayak Production Association	Solution	U(90) uranyl nitrate (1.98 kg U-235; 28.6 l)	Cylinder with elliptical bottom, water reflected	Not known	11 excursions, 7 hrs.	5.5×10^{17}	Miscommunication on uranium inventory	None
SP 18	8/24/1970	Windscale Works, England	Windscale	Pu complex (2.15 kg Pu; 2.07 kg Pu-239; 40 l)	Cylinder, hemispherical bottom	No estimate	5-10 sec.	1×10^{15}	Pu accumulated in organic	None
SP 19	10/17/1978	Idaho Chemical Processing Plant	Solution	U(82) nitrate solution (6.08 kg U-235; 315.5 l)	Cylinder, unreflected	Not known	~ 2 hrs.	2.7×10^{18}	Partially closed loop steadily increasing uranium concentration	None, fission products in stack were released to outside.
SP 20	5/15/1997	Novosibirsk Chemical Concentration Plant	Solution	U(70) oxide slurry and crust (17.1 kg U-235)	Two parallel cylinders, unreflected	4.3×10^{15}	Six excursions, 27 hrs. 5 min.	5.5×10^{15}	Buildup of uranium in pipes	None
SP 21	9/30/1999	JCO Fuel Fabrication Plant	Solution	U(18.8) uranyl nitrate solution (3.12 kg U-235; 45.0 l)	Cylinder, unreflected	5×10^{16}	19 hrs. 40 min.	2.5×10^{18}	Weak understanding, multiple subcritical solution containers combined	Significant contamination due to tank vents

Table 3-1 Summary of Known Accidental Criticality Excursions (continued)

b) Metal Systems										
Metal Experiments (ME xx)										
No.	**Date**	**Location**	**Title for Ref.**	**Fissionable Material**	**Arrangement**	**Initial Prompt Critical Burst, Fissions**	**Duration**	**Total Fissions**	**Cause**	**Physical Damage**
Metal Experiments - Open Systems										
ME 1	8/21/1945	LASL - Los Alamos, NM	Hand Stacking Reflector Pu Core	Delta phase Pu metal (6.2 kg)	Sphere reflected by WC	≈ 1.8×10^{15} (10 cents over)	< 1 sec.	≈ 1×10^{16}	Dropped reflector block during hand-stacking	None
ME 2	5/21/1946	LASL - Los Alamos, NM	Screwdriver	Delta phase Pu metal (6.2 kg)	Sphere reflected by Be	≈ 1.8×10^{14}	< 1 min.	≈ 3×10^{15}	Screwdriver holding reflector away from Pu slipped	None
ME 3	2/1/1951	LASL - Los Alamos, NM	Aquarium machine	Separate cylinder and annulus, U(93) metal (24.4 kg and 38.5 kg)	Side by side in water tank	≈ 6×10^{15}	Perhaps several bursts, < 1 min.	1×10^{17}	Went critical during practice scram	Slight oxidation
ME 6	2/3/1954	LASL - Los Alamos, NM	Godiva I	U(93) metal (54 kg)	Sphere-unreflected	5.6×10^{16}	Single burst, < 1 min.	5.6×10^{16}	Assembled too rapidly	Slight warping of pieces (loss: $600)
ME 7	2/12/1957	LASL - Los Alamos, NM	Godiva II	U(93) metal (54 kg)	Sphere-unreflected	1.2×10^{17} (21 cents over)	Single burst, < 1 min.	1.2×10^{17}	Graphite fell against assembly	Warping, oxidation, near melting close to center (loss: $2400)
ME 8	6/17/1960	LASL - Los Alamos, NM	9-inch cylinder	U(93) metal (51 kg)	Cylinder, graphite-reflected	≈ 1×10^{15}	< 1 min.	6×10^{16}	Error in addition estimate	Trivial
ME 9	11/10/1961	ORNL - Oak Ridge , TN	U-Paraffin	U(93) metal (≈ 75 kg)	Cylinder, paraffin-reflected	≈ 1×10^{15}	< 1 min.	≈ 1×10^{16}	Error in addition estimate, too rapid assembly	None
ME 10	3/11/1963	Sarov (Arzamas-16)	Metal Core	Delta phase Pu metal (~17.35 kg)	Sphere, LiD reflected	Not known	< 1 min.	5×10^{15}	Violations of operating procedures, adjustments with the core in place	None
ME 13	4/5/1968	Chelyabinsk-70	Metal Core	U(90) metal (47.7 kg)	Sphere, natural uranium reflected	Not known	< 1 min.	6×10^{16}	Failure to reposition lower reflector prior to assembly	None
ME 15	6/17/1997	Sarov (Arzamas-16)	Metal Core	U(90) metal (~44 kg)	Sphere, copper reflected	4×10^{15}	6 days 13 hrs. 55 min.	(2×10^{17} in initial 3-5 min burst) ~ 1×10^{19}	Upper copper hemishell dropped onto assembly	None

Table 3-1 Summary of Known Accidental Criticality Excursions (continued)

No.	Date	Location	Title for Ref.	Fissionable Material	Arrangement	Initial Prompt Critical Burst, Fissions	Duration	Total Fissions	Cause	Physical Damage
Metal Experiments - Closed Systems										
ME 4	4/18/1952	LASL - Los Alamos, NM	Jemima	U(93) metal (92.4 kg)	Cylinder, unreflected	≈ 1×10^{15} (21 cents over)	< 1 sec	1.5×10^{16}	Computation error	None
ME 5	4/9/1953	Sarov (Arzamas-16)	Metal Core	Delta phase Pu metal (~8 kg)	Sphere, natural uranium reflected	Not known	< 1 min.	1×10^{16}	Operator mistakenly installed shorter stops, causing increased reflection	Portion of core melted, hemishells fused
ME 11	3/26/1963	LRL - Livermore, CA	LRL	U(93) metal (47 kg)	Cylinder, Be-reflected	1×10^{17}	< 1 min.	3.76×10^{17}	Ram caught reflector; lifted; fell	Metal melted and some burned, contamination (loss: $94,881)
ME 12	5/28/1965	WSMR - White Sands, NM	U-Mo Alloy	U(93)-10.0% Mo alloy (96 kg)	Cylinder, unreflected	1.5×10^{17}	< 1 min.	1.5×10^{17}	Incorrect operation, interlock bypassed	Assembly bolts broken, minor damage to coating
ME 14	9/6/1968	Aberdeen Proving Ground, Maryland	Metal Core	U(93)-Mo alloy (123 kg)	Sphere, unreflected	6.09×10^{17}	Single burst, < 1 min.	6.09×10^{17}	Burst rod passed through a reactivity maximum before seating	Fuel components damaged, warping, core components fusing
Metal Processing (MP xx)										
Metal Processing - Open Systems										
MP 1	12/13/1978	Siberian Chemical Combine	Metal Ingots	Alpha phase Pu metal (10.68 kg Pu)	Polyethylene block lined with cadmium	3×10^{15}	Single burst, < 1 min.	3×10^{15}	Lack of communication resulting in mass limit exceeded	None

Table 3-1 Summary of Known Accidental Criticality Excursions (concluded)

c) Miscellaneous Systems										
Miscellaneous Systems (Misc xx)										
Open Systems										
Misc 1	2/11/1945	LASL - Los Alamos, NM	Dragon	$U(93)H_{10}$ pressed in Styrex (UC_4H_{10})	Assembly of blocks	$\approx 6 \times 10^{15}$	Single burst, < 1 min.	$\approx 6 \times 10^{15}$	Excess reactivity addition	Cubes swollen and blistered
Misc 2	6/6/1945	LASL - Los Alamos, NM	Metal Cubes	U(79.2) metal as 1/2 in. cubes (35.4 kg)	Array of cubes; H_2O reflected	$\approx 3 \times 10^{15}$	Perhaps 3 bursts, < 1 min.	$\approx 4 \times 10^{16}$	Water leaked into array	None
Misc 3	11/29/1955	Idaho Reactor Testing Area	EBR-1	52 kg enriched U, 1/2 in. rods	Cylinder, rods NaK cooled	4.6×10^{17}	< 1 min.		Incorrect scram used	Core molten
Misc 4	7/3/1956	LASL - Los Alamos, NM	Honeycomb	58 kg U(93) metal foil sandwiched with carbon	Cylinder, Be-reflected	Not known	< 1 min.	3.2×10^{16}	Assembled too rapidly	None
Misc 5	11/18/1958	Reactor Testing Area, Idaho Falls, Idaho	Aircraft	U-235 oxide Ni-Cr elements, ZrH moderated	Cylinder, prototype aircraft engine	2.5×10^{19}	< 1 min.		Incorrect wiring in ion chamber circuit	Every fuel cartridge experienced melting
Misc 6	12/11/1962	LASL - Los Alamos, NM	ZEPO	U(93) metal foils sandwiched with carbon	Cylinder, C and Be reflected	3×10^{16} (12 cents prompt critical)	Single burst, < 1 min.	3×10^{16}	Excess fuel addition	None

Table 3-2 Inhomogeneous Water-Moderated Systems [Stratton 1967, McLaughlin 2000]

Water Moderated (W xx)						
Date	**Location**	**Active Material**	**Geometry**	**Total fissions**	**Cause**	**Physical damage**
W1 6/2/1952	ANL, Illinois	6.8 kg U-235 oxide particles in plastic	Inhomogeneous cylinder, water moderated	1.22×10^{17}	Manual withdrawal of central safety rod	Plastic destroyed
W2 7/22/1954	Reactor Testing Area, Idaho Falls, Idaho	4.16 kg U(93) as U-Al plates, Al clad	Inhomogeneous cylinder, water moderated	4.68×10^{18}	Estimate of expected excursion too low	Reactor destroyed
W3 3/15/1960	Saclay, France	2.2 tons $U(1.5)O_2$	Canned UO_2 rods in water	3×10^{18}	Control rod withdrawn	None
W4 1/3/1961	Reactor Testing Area, Idaho Falls, Idaho	U(93)-Al plates, Al clad	Inhomogeneous cylinder, water moderated	4.4×10^{18}	Quick manual withdrawal of control rod	Reactor destroyed, building contaminated
W5 11/5/1962	Reactor Testing Area, Idaho Falls, Idaho	U(93)-Al plates, Al clad	Inhomogeneous cylinder, water moderated	$\sim 1 \times 10^{18}$	Rapid energy transfer from molten fuel to water	Fuel, water, and core structure rapidly ejected from vessel
W6 2/15/1971	Kurchatov Institute	$U(20)O_2$	Rods, water moderated, beryllium reflected	2×10^{19}	Too much water added to core resulting in 50 pulses before pump turned off 5 to 7 minutes later.	None
W7 5/26/1971	Kurchatov Institute	$U(90)O_2$	Rods, water reflected	2×10^{18}	Water dumping resulted in plate bringing fuel elements closer	None
W8 9/23/1983	RA-2 Facility, Buenos Aires, Argentina	MTR type fuel elements	Pool type reactor	$\sim 4 \times 10^{17}$	Installation of control element with moderator and fuel present	None

Table 3-2 Inhomogeneous Water-Moderated Systems (Concluded)

Heavy Water Moderated (D xx)						
Date	**Location**	**Active Material**	**Geometry**	**Total fissions**	**Cause**	**Physical damage**
D1 ~1950	Chalk River, Canada	Natural U, Al clad	Rods, D2O moderated, graphite reflected	Unknown	Heavy water level rose too high	Minor
D2 12/12/1952	Chalk River, Canada	Natural U	Rods, D_2O moderated, graphite reflected	1.2×10^{20}	Safety circuits failed; control rod misoperation	Core and calandria ruined, building basement contaminated
D3 10/15/1958	Boris Kidrich Institute, Vinca, Yugoslavia	3995 kg natural U	Rods, D_2O moderated, unreflected	$\sim 2.6 \times 10^{18}$	Too much D_2O added in final step of experiment	None
D4 12/30/1965	Mol, Belgium	1200 kg $U(7)O_2$	Canned UO_2 rods in 70%H_2O, 30%D_2O	4.3×10^{17}	Manual withdrawal of control rod	None

Table 3-3 Destructive Power Excursion Summary [Nyer 1965]

Reactor	Reactivity addition, $	α, s^{-1}	Peak power, MW	Energy release, MWs	Maximum temp. °C	Maximum energy density, $W\text{-}s/cm^3$	Maximum pressure, psi	Remarks
BORAX I, July 22, 1954 *Same as W2 in Table 6.2*	3.1	384	≤ 19,000	135	≤ 1,800	≤ 6,500	6,000 - 10,000	Destroyed core, vessel, and some associated equipment. Small fission-product release. Steam explosion proposed as cause.
SL-I January 3, 1961 *Same as W4 in Table 6.2*	3	280	~ 19,000	133	> 2,075	> 7,300	10,000	Destroyed core, bulged vessel, local fission-product contamination. 10% fission-product release. Steam explosion - minor contribution from metal-H_2O reaction.
SPERT-I D-12/25 A series of tests, which progressed through limited melting of the core to the final destructive excursion (November 5, 1962). *Same as W5 in Table 6.2*	2.6	200	1,130	11	585	2,000	7	Melted ~ 0.3% of core.
	2.7	218	1,270	19	680	2,300	8	Melted ~ 3% of core.
	3.55	313	2,250	31	1,360	4,600	≤ 4,000	Melted ~35% of core. Destroyed core and associated equipment, bulged tank. ~ 4% fission-product release. Probable steam explosion - Al_2O_3 analysis indicates ~ 3.5 MWs energy release from metal-H_2O reaction.
SPERT I oxide core This covered 2 tests with the second having more reactivity added, but yielding essentially the same results. (November 10, 1963 and April 14, 1964)	2.6	455	17,400	155	1,800	2,200	70	Two fuel rods ruptured. Discoloration and/or deformation of 25% of fuel rods. Negligible fission-product release.
	3.3	645	35,000	155	1,800	2,200	130	Two fuel rods ruptured. Discoloration and/or deformation of 25% of fuel rods. Negligible fission-product release.
SNAPTRAN-3 April 1, 1964	3.5	1,400	~ 20,000	50	> 2,500	7,100	~ 4,000	Rapid water immersion of SNAP 10A/2 reactor with NaK. Burst pressure vessel. All fuel rods ruptured, ~half of fuel reduced to powder form. Negligible fission-product escape.

3.1.5. Analytical Models for Solution Criticalities

A number of empirical models have been developed to estimate total fissions generated in excursions involving fissile solutions. A literature review was completed that includes relevant or interesting data from a variety of located reports describing fission yield correlations for accidents or solutions processing.

Some important conclusions from the literature review include:

- Most of the data located involves solutions or processing accidents, including the CRAC and SILENE experiments.
- Both CRAC and SILENE utilized a 93% enriched uranyl nitrate solution.
- Very little information was found with respect to simple correlations for metal systems.
- The metal systems were independently analyzed with respect to fission yield values with the intent of determining a basic correlation to fit the data.

3.1.5.1. Fission Yields for Fissile Solutions

Appendix D of the ISO Standard [ISO 2011] presents a number of simplified formulae for estimating fission yield. Simple comparisons were performed using these various correlations for an integrated fission yield, denoted as N_f, determination from solutions. The correlations compared are limited to easily obtainable information about a system, such as solution volume V in units of liters or excursion duration t in units of seconds, with the intention of being used as a generic approximation without requiring detailed system analysis. Percent differences with respect to the reported value for fission yields for the solution accidents were evaluated to identify those correlations that represent the best bounding values. Two of the correlations: [Barbry 1987] and [Tuck 1974] seem to produce the best results.

The [Barbry 1987] formula presented in Equation (4-3) below:

$$N_f(t) = \frac{t}{3.55\times10^{-15} + 6.38\times10^{-17} \cdot t} \cdot V \tag{3-3}$$

has an average percent difference of 2618% over all of the 21 solution processing accidents. However, if the outliers (atypical events) are removed, then the average percent difference is decreased to 135% and tends to over-predict the total fissions. This was also the most commonly found correlation for solution criticality estimates throughout the literature review.

The empirical relationships in [Tuck 1974] were developed from data for experimental studies on solution criticalities in Kinetic Experiments on Water Boilers (KEWB) and the French study CRAC. The model calculates the maximum fissions during a 5 second burst, total fissions, and specific fission rate (the duration is assumed to range from 10 minutes to 40 hours based upon historical excursions). Over the 21 solution processing accidents, this formula has an average percent difference of 965%, or -52% when excluding outliers; showing a tendency to under-predict reported fission yields. Only the volume of the tank (V, in liters) is required to calculate the total integrated fission yield using the formula:

$$N_f = 2.4\times10^{15} \cdot V \tag{3-4}$$

Note that both Equations (3-3) and (3-4) were by far the most accurate of those tested on solutions accidents, and it can be assumed that the [Barbry 1987] formula in Equation (3-3) is generally more conservative for solution accident scenarios.

Nakajima [Nakajima 2003] also reviewed different formulae and concluded that Nomura and Okuno's formula [Nomura 1995] and Barbry's formula [Barbry 1987] with an infinitive duration agreed fairly well with known data for solution accidents as a function of solution volume. Olsen's formula and Barbry's formula as a function of duration reproduce the upper envelope with the exception of the ICPP 1959 and Tokaimura 1999 accidents. The conclusion is made that because the Tokaimura accident underwent a solution cooling process that produced a large amount of power for a long time, a new formula would be required which takes that into account.

This indicates that the use of Barbry's formula provides a good upper bound for the estimation of fission yield from a solution criticality accident.

3.1.6. Analytical Models for Metal Criticalities

It is important to note that very little information was found with respect to simple correlations for a metal system. Metal systems have been characterized according to HEU vs. Pu, and by reflector density. The Sarov 1997 accident is considered an outlier and atypical system, occurring over a time frame of 6.5 days and with a total fission yield of 1×10^{19}. Every other metal accident can be considered as a single burst excursion.

The most promising yield correlations were obtained from reflector density characterizations. A "heavy" reflector (tungsten carbide, natural uranium) provides a yield of:

$$N_f = 7.32\times10^{15} \cdot e^{4.41\times10^{-2}\cdot m} \tag{3-5}$$

A "light" reflector (graphite, beryllium, water) characterizes a yield of:

$$N_f = 1.86\times10^{15} \cdot e^{6.80\times10^{-2}\cdot m} \tag{3-6}$$

While a system with no reflector has the correlation:

$$N_f = 1.80\times10^{16} \cdot e^{2.65\times10^{-2}\cdot m} \tag{3-7}$$

Note that m is the term for the system mass in kilograms.

These formulas were derived based on the 15 metal criticality excursions (omitting Sarov – ME 15 in Table 3-1) and can be used to estimate fission bounds for hypothetical accidents.

3.1.7. Assessment of Fission Yields

Once it is determined that a postulated scenario may physically result in an excursion, it is necessary to determine the potential fission yield for the proposed excursion. The total fission yield is defined by the type of system and the fissile material involved. This section provides reference fission yields that may be used for general SAR purposes. Care should be taken to ensure that, as the NRC has noted, potentially unique situations do not exist at a given facility.

Table 3-4 provides a list of bounding criticality accident fission yields (based on [McLaughlin 2003] and [Barbry 2009]). These values bound most of the accidents listed in Table 3-1and Table 3-2. The few that are not bounded are considered unique in their accident scenario.

Table 3-4 Bounding Criticality Accident Fission Yields [McLaughlin 2003, Barbry 2009]

System	Initial Burst Yield (fissions)	Total Yield (fissions)
Solutions	1×10^{15} fissions/liter	1.6×10^{16} fissions/liter
Solutions Boiling (onset)		1.1×10^{16} fissions/liter
Fully Moderated Solids	No Historical Data	
Small Metal Pieces, Large Storage Arrays	No Credible Accident Sequence	
Solid Uranium	1×10^{18}	1×10^{19}
Solid Plutonium	1×10^{16}	1×10^{18}

3.1.7.1. Solutions

The twenty-one excursions that have occurred in processing plants (non-experimental facilities) are listed in Table 3-5 with part (a) being those involving uranium and part (b) those involving plutonium. The information represents a combination of data from tables in [McLaughlin 2000].

Total fission yields for uranium range from 8×10^{15} to 4×10^{19}, and for plutonium range from $\sim1\times10^{15}$ to 8×10^{17} fissions. All of the events had multiple causes; none were caused by a single failure. Fourteen involved inadvertent transfer to non-safe vessels or systems. A number involved organic extraction or concentration into a solvent layer with the aqueous component providing reflection. The human element was the dominant cause for all of the accidents.

The highest value (4×10^{19} fissions from SP6 in Table 3-1) resulted from the siphoning of a large volume (~ 800 liters) containing 34.5 kilograms of ^{235}U (approximately 70 times the minimum critical mass) from a safe to unsafe geometry with neutrons reflected by concrete below the cylinder.

For solution systems in Table 3-1 the accidents have been characterized as either open or closed systems, affecting the radioactive release from the system, and the duration of the excursion in the case of solution systems. Accidents occurring in open containers are typically single burst. Those with large spikes such as the Wood River Junction Accident (SP14) will result in 15 to 20 percent of the solution being ejected from the container. For those with smaller spikes, the continual addition of liquid may create smaller spikes or a slightly delayed supercritical system that may boil for an extended time.

Using the information from Barbry's paper [Barby 1987] as presented in McLaughlin's 2003 paper [McLaughlin 2003], accidents can be characterized by the number of fissions in the first spike, or if there are additional spikes/delayed supercritical configuration, then the accident duration should be limited to 2 hours. For those scenarios that are slow to develop, then an eight-hour bounding duration is suggested based on DOE-STD-3009-2014 [DOE 2014]. For the first spike, the number of fissions can be estimated as 1×10^{15} fissions per liter of solution. For a longer duration, use of Table 3-1 provides an estimate of the maximum specific fission yield (fissions per liter). The bounding value for total specific fissions appears to be 1.6×10^{16} fissions / liter. There are only 3 processing accidents with durations longer than 8 hours: [Hanford 1962] – SP10, [Novosibirsk 1997] - SP20, and [Tokai-Mura 1999] -SP21 in Table 3-5. Based on these 3 accidents, it is estimated that the ratio of the 8-hour fissions to first-spike fissions is perhaps a factor of 30.

Thus, there seem to be 3 categories of solution excursions: those with a single spike (typically open systems or those where material is forced into process piping), those with multiple excursions (typically closed systems or open systems with continuing solution transfer), and those lasting 8 hours or more.

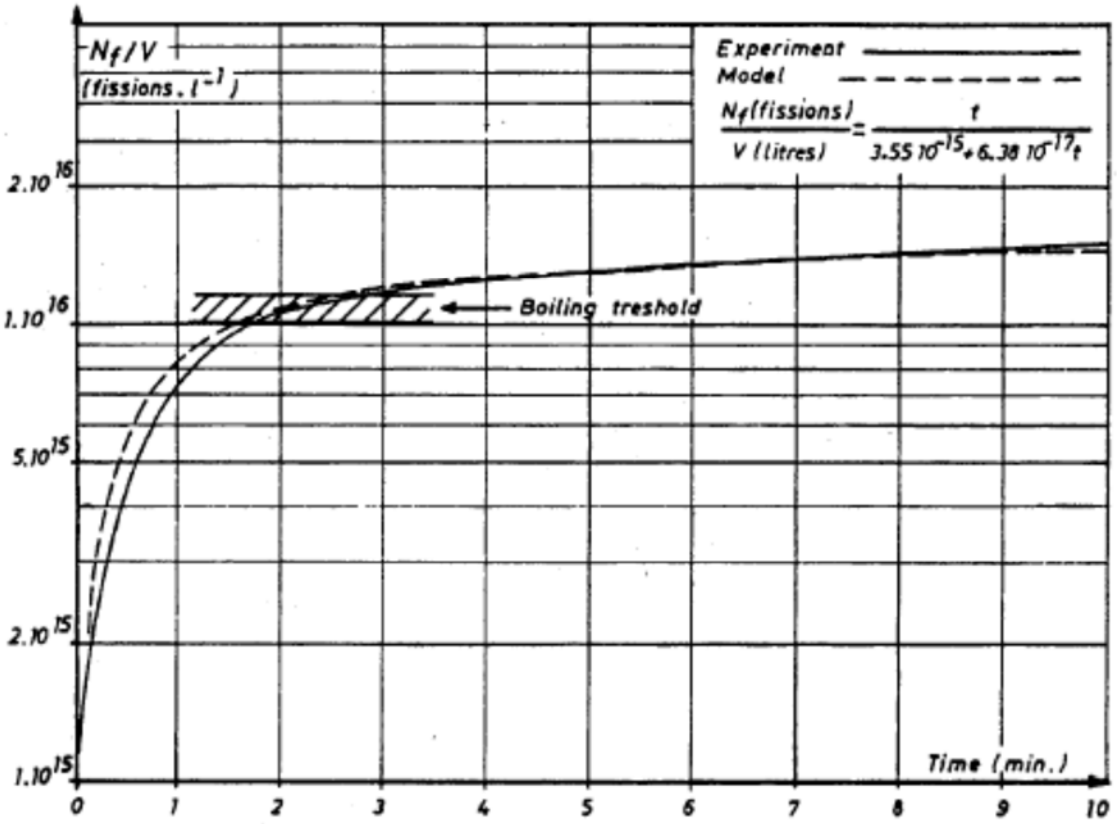

Figure 3-1 Maximum Specific Fission Yields Resulting from Solution Excursion Experiments in CRAC and SILENE [Barbry 1987].

According to [McLaughlin 2003], "For operations with significant quantities of fissile materials in solution form, there are significant reported experimental data, and more being generated. Practically all site- and process specific criticality accident characterizations and evaluations should be able to be performed by the direct use of these data. The absence of computer codes and software models of physical processes such as bubble generation does not appear to be an impediment to the implementation of well-founded emergency plans and procedures. On the contrary, it is always preferable to solve issues with directly applicable experimental data, and such data appear to be largely available for solution criticality accidents."

Table 3-5 Accident Fission Energy Releases (a) Uranium, (b) Plutonium Solution Criticality Accidents. [McLaughlin 2000]

(a)

No.	Site and Date	First Spike Yield (1E+17 fiss)	Fissile Volume (liters)	Specific Spike Yield (1E+15 fiss/lt)	Total Yield (1e17 fiss)	Fissile Mass (kg)	Fissile Concentration (g/lt)
SP2	Mayak (R.F.) Apr 21, 1957	unknown	30.0	unknown	~1.0	3.06	102
SP3	Mayak (R.F.) Jan 2, 1958	~2.0	58.4	3.4	~2.0	22.00	377
SP4	Y-12 (U.S.) June 16, 1958	~0.1	56.0	0.2	13.0	2.10	38
SP6	ICPP (U.S.) Oct 16, 1959	~1.0	800.0	~0.1	400.0	30.90	39
SP8	ICPP (U.S.) Jan 25, 1961	~0.6	40.0	1.5	6.0	7.20	180
SP9	Tomsk (R.F.) July 14, 1961	none	42.9	none	0.12	1.68	39
SP12	Tomsk (R.F.) Jan 30, 1963	unknown	35.5	unknown	7.9	2.27	64
SP13	Tomsk (R.F.) Dec 2, 1963	none	64.8	none	0.60	1.93	30
SP14	Wood River (U.S.) July 24, 1964	~1.0	41.0	2.4	~1.3	2.07	50
SP15	Electrostal (R.F.) Nov 03, 1965	none	100.0	none	~0.08	3.65	37
SP16	Mayak (R.F.) Dec 16, 1965	none	28.6	none	~5.5	1.98	69
SP19	ICPP (U.S.) Oct 17, 1978	unknown	315.5	unknown	27.0	6.08	19
SP20	Novosibirsk (R.F.) May 15, 1997	none	*	none	0.055	17.10	*
SP21	Tokai–mura (Japan) Sept 30, 1999	~0.5	45.0	1.1	25	3.12	69
* System description was not adequate to estimate parameter.							
		Maximum		**Maximum**	**Maximum**	**Range**	**Range**
		2.0 E+17		3.4	400 E+17	1.7 to 30.9	19 to 377

Table 3-5 Accident Fission Energy Releases (concluded)

(b)

No.	Site and Date	First Spike Yield (1E+17 fiss)	Fissile Volume (liters)	Specific Spike Yield (1E+15 fiss/lt)	Total Yield (1e17 fiss)	Fissile Mass (kg)	Fissile Concentration (g/lt)
SP1	Mayak (R.F.) Mar 15, 1953	unknown	31.0	unknown	~2.0	0.81	26
SP5	LASL (U.S.) Dec 30, 1958	1.5	160.0	0.94	1.5	2.94	18
SP7	Mayak (R.F.) Dec 05, 1960	unknown	19.0	unknown	~2.5	0.85	45
SP10	Hanford (U.S.) Apr 7, 1962	~0.1	45.0	0.2	8.0	1.29	29
SP11	Mayak (R.F.) Sept 9, 1962	none	80.0	none	~2.0	1.26	16
SP17	Mayak (R.F.) Dec 10, 1968	0.3	28.8	1.0	~1.3	1.50	52
SP18	Windscale (R.F.) Aug 24, 1970	none	40.0	none	0.01	2.07	52
		Maximum		**Maximum**	**Maximum**	**Range**	**Range**
		1.5 E+17		1.0	8 E+17	0.8 to 2.94	16 to 52

3.1.7.2. Fully Moderated/Reflected Solids

This configuration covers reflected bulk metal and metal pieces or solid fines, such as powders, that are moderated or reflected (the material for which is assumed to be water as it is typically present in most processing facilities and can assume any shape needed for close fitting reflection). These systems are assumed to be bounded by the values from solution systems as given in Table 3-6 for uranium and Table 3-9 for plutonium assuming the bounding numbers of fissions given in Table 4-4. For a Single Spike, these are 1×10^{18} for uranium and 1×10^{16} for plutonium. For Multiple Excursions, 1×10^{19} for uranium and 1×10^{18} for plutonium.

Only one process criticality accident has involved solid metal with some reflection; this was the assembly of 4 pieces of plutonium metal. There was a single burst of 3×10^{15} fissions, followed by either intentional or mechanical disassembly of the configuration. There was no melting or deformation of the metal units. Although this was the only metal accident, and there are no plutonium metal experiments to provide a basis for comparison, the two Los Alamos critical accidents with a reflected plutonium metal sphere (1945 and 1946) exhibit similar specific spike yields.

The sixteen metal excursions listed in Table 3-1 are bounded by the values given in Table 3-4. Given the types of situation encountered in DOE facilities where it is difficult to accumulate the quantity of materials required, to contain the material and moderator, and to assume any shape that would be unfavorable, a reference value of 1×10^{18} fission in a single burst is assessed to be the bounding reference value and is believed to be very conservative.

3.1.7.3. Bare, Dry Solids and Large Storage Arrays

This configuration covers solids (e.g., metal fines, loose oxide powders) that may be reflected but have no moderation (i.e., not immersed in liquid). There is no accident data for such systems dominated by fast neutron fissions. For large storage arrays, it should be easy to protect against an accident by appropriate packaging of individual items. For both of these fissile forms, the past Criticality Safety Evaluations have been able to document no credible accident sequences, and it is expected that this will continue in the future.

"Criticality accidents with solid metal systems (including alloys) should be readily controlled at a likelihood of occurrence that is vanishingly small. ... Only rarely are there operational requirements which necessitate working with more than the water reflected spherical critical mass (^{233}U 6.0 kg, ^{235}U 20.1 kg, ^{239}Pu 5.0 kg) ... " [McLaughlin 1991]. Issues related to criticality and potential extreme excursions in storage environments are most appropriately handled in the arena of criticality safety evaluations performed by criticality safety professionals for the purpose of minimizing chances of occurrence. Design considerations relating to these issues should not be driven by unrealistic dose calculations from unattainable accident scenarios. If it is necessary to consider an upper bound of consequence, then 1×10^{17} seems acceptable for use based on a review of the metal systems excursions.

3.2. Material Release in Criticality Excursions

The radionuclides generated by an excursion are a function of the fissionable material undergoing the reaction. The quantity of each fission product or actinide formed is a function of the total fission yield. Bounding values for the fission yields of various systems were designated in the previous

section. Estimation of fission product quantities was done with the SCALE 6.2 computer code [Rearden 2016] using the "t-depl" sequence [Rearden 2016]. The scenarios were done for solution systems, but can be applied to the moderated reflected systems to determine upper bounds. The three scenarios are:

1. Single pulse of 0.2 second duration for a total of 1×10^{17} fissions (100 liters of solution) based on 1×10^{15} fissions per liter of fissile solution in the container [Barby 1987, McLaughlin 2003, ANS-8.23 2007]. The radionuclide activities are calculated at 10 and 60 minutes after the termination of the pulse.

2. Multiple pulses for a total of 10 minutes. The total fissions were 1×10^{18} fissions (100 liters of solution) based on 1×10^{16} fissions per liter [Barbry 1987, McLaughlin 2003, ANS-8.23 2007]. ARF values were determined for both non-boiling and boiling scenarios, but it was assumed that the radionuclide activities depended only on total number of fissions. The radionuclide activities are calculated at 20 minutes and 60 minutes after the termination of the excursion.

3. A slow cooker excursion (delayed supercritical) over an eight-hour period. The total specific fission rate was assumed to be 3×10^{16} fissions per liter. The radionuclide activities are calculated at 1 hour, 2 hours, 3 hours, 4 hours, 5 hours, 6 hours, 7 hours, and 8 hours after the start of the excursion, during the excursion evolution.

For any specific scenario, the activities need to be multiplied by the ratio of the volume of the container to 100 liters. In addition, if the scenario involves multiple pulses and boiling then the activities from multiple pulse excursions also need to be multiplied by 1.6 to account for these additional fissions.

The provided tables do not list any particulate fission products as the historical data shows minimal release of fission products in these excursions. The quantity of particulate fission products is normally small, their potential release fractions are likewise small, and – unlike noble gases and iodine – they are subject to facility filtration. Accordingly, not accounting for them is typically an adequate approximation. If these might be of concern in a scenario, then specific scenarios need to be analyzed with appropriate computer models. Site personnel should perform whatever background work they believe is warranted to verify that unusual or unique circumstances do not exist at their facilities.

3.2.1. Solutions

Airborne release values for the noble gases and radioactive iodine generated in a solution excursion have been taken from [Barbry 2009] based on estimates from the CRAC and SILENE experiments. In most cases, the amount of energy generated by the excursion is not sufficient to disable the engineered gaseous effluent treatment devices on the facility exhaust, but no DOE non-reactor facility is known to have gaseous effluent treatment device to attenuate the noble gases. All the noble gases generated in a liquid are assumed to be released to the atmosphere, generally through the facility effluent treatment system. According to [Barbry 2009], "Noble gas (Xe and Kr) release rates are virtually 100% for half-lives exceeding 1 minute. They vary between 10 and 50% for half-lives ranging from a few seconds to 1 minute (^{90}Kr to ^{98}Kr) and are of the order of 10% for very short half-lives (< 2 seconds). These rates are not affected by the type of fissile medium or its

acidity." The ARF for radioactive iodine and generated in a single spike excursion will be less than 0.01 while that for the short-lived radioactive isotopes of ruthenium and bromine will be around 0.01 and 0.2 respectively. These values are given in Table 3-6.

Table 3-6 Estimated ARF Values for Solution Excursions. [Barbry 2009]

Fission Product	Half-Life $\left(t_{\frac{1}{2}}\right)$	Maximum Release Rate
Noble Gases	$t_{\frac{1}{2}}$ > 1 minute	100%
^{91}Kr	2 seconds < $t_{\frac{1}{2}}$ < 1 minute	25%
^{140}Xe	2 seconds < $t_{\frac{1}{2}}$ < 1 minute	50%
^{141}Xe, ^{92}Kr	$t_{\frac{1}{2}}$ < 2 seconds	10%
Iodine	$t_{\frac{1}{2}}$ < 2 seconds	20% (boiling) 1% (no boiling)
Bromine	$t_{\frac{1}{2}}$ < 2 seconds	20%
Ruthenium	$t_{\frac{1}{2}}$ < 2 seconds	1%

These values seem appropriate for use with solutions free of fission products.

Source terms for the three uranium solution scenarios are given in Table 3-7 through Table 3-9.

Table 3-7 provides values for the noble gases, iodine, and short-lived bromine (half-lives less than 2 seconds) in a single spike excursion involving uranium solutions.

Table 3-8 provides values for the noble gases, iodine, and short-lived bromine (half-lives less than 2 seconds) for multiple excursions involving uranium solutions.

Table 3-9 provides values for the noble gases, iodine, and short-lived bromine (half-lives less than 2 seconds) in a "slow cooker" excursion involving uranium solutions.

"For the other volatile fission products – bromine and ruthenium isotopes – the estimated maximum release rates were 20% and 1%, respectively" [Barbry 2009]. The activities of the short-lived ruthenium isotopes in a solution free of fission projects showed little or no activity. For the formation of radiolytic gases, [Barbry 1993] indicates that the threshold is 1.5×10^{15} fissions per liter. Only 2 historical accidents were above this value. Both of these (SP3 and SP14) had significant overpressures and splashing/loss of 10 to 20 percent of the solution. There was contamination in both cases due to the fluid ejection, but there were no reports of significant airborne releases from either excursion. Based on this, it seems unlikely that a single spike excursion will generate significant radiolytic gases or associated activities. Based on solution experiments, the ARFs for halogens are expected to be minimal (i.e., less than 0.01) unless the excursion involves boiling. For those cases where boiling occurs (typically after the first spike in solutions above the 1.6E16 fissions per liter threshold), then the ARF for iodine will be 0.20.

Table 3-7 Curies of Important Nuclides Released from First Spike in Uranium Solution Criticality (based on 10^{17} fissions and 100 liters of solution)

Nuclide	Half-Life	Radioactivity, Curies			ARF (1)
		At end of Spike	10 min after spike	60 min after spike	
Krypton					
Kr-83m	1.8 hr	5.31E-06	1.76E-02	2.09E-01	1.0
Kr-85	10.8 yr	1.60E-07	4.94E-07	2.36E-06	1.0
Kr-85m	4.5 hr	7.27E-03	1.36E+00	1.34E+00	1.0
Kr-87	76.3 min	1.91E+00	9.84E+00	6.25E+00	1.0
Kr-88	2.8 hr	3.30E+00	6.37E+00	5.20E+00	1.0
Kr-89	3.2 min	3.49E+02	5.08E+01	8.48E-04	1.0
Kr-90 to Kr-98	<35 sec	4.40E+04	7.17E-03	0.00	0.25
Xenon					
Xe-133	5.2 days	2.82E-05	2.13E-04	4.14E-03	1.0
Xe-133m	2.2 days	1.92E-04	2.04E-04	4.77E-04	1.0
Xe-135	9.1 hr	4.64E-02	1.30E-01	4.49E-01	1.0
Xe-135m	15.3 min	3.02E+00	2.22E+00	9.27E-01	1.0
Xe-137	3.8 min	2.68E+02	8.78E+01	1.00E-02	1.0
Xe-138	14.1 min	1.09E+02	8.71E+01	7.43E+00	1.0
Other isotopes	<40 sec	2.97E+04	1.72E-01	5.46E-06	0.25
Iodine					
I-131	8.0 days	1.29E-04	2.73E-03	3.57E-02	0.01 (2)
I-132	2.3 hr	2.08E-02	3.17E-02	9.47E-02	0.01 (2)
I-133	20.8 hr	2.34E-02	3.80E-01	1.18E+00	0.01 (2)
I-134	52.5 min	3.04E+00	1.04E+01	1.97E+01	0.01 (2)
I-135	6.6 hr	2.38E+00	4.99E+00	4.57E+00	0.01 (2)
Other isotopes	< 40 sec	1.85E+04	1.91E+00	1.03E+00	0.01 (2)
Short-lived Bromine	< 2 seconds	1.37E+04	0.00	0.00	0.20

(1) Values from [Barbry 2009]

(2) ARF will be less than 0.01 for the single spike case

Table 3-8 Curies of Important Nuclides Released from Multiple Excursions in Uranium Solution Criticality (based on 10^{18} fissions and 100 liters of solution)

Nuclide	Half-Life	Radioactivity, Curies			ARF (1)
		At end of 10 Min Excursion	20 min after Excursion End	60 min after Excursion End	
Krypton					
Kr-83m	1.8 hr	7.30E-01	6.67E+00	2.28E+01	1.0
Kr-85	10.8 yr	3.11E-05	1.07E-04	2.54E-04	1.0
Kr-85m	4.5 hr	8.66E+01	1.46E+02	1.32E+02	1.0
Kr-87	76.3 min	9.12E+02	8.58E+02	5.97E+02	1.0
Kr-88	2.8 hr	6.37E+02	5.99E+02	5.09E+02	1.0
Kr-89	3.2 min	1.84E+04	2.27E+02	3.42E-02	1.0
Kr-90 to Kr-98	<35 sec	4.67E+04	1.44E-07	0.00	0.25
Xenon					
Xe-133	5.2 days	9.48E-03	1.01E-01	4.67E-01	1.0
Xe-133m	2.2 days	1.96E-02	2.59E-02	5.13E-02	1.0
Xe-135	9.1 hr	8.84E+00	2.38E+01	4.75E+01	1.0
Xe-135m	15.3 min	2.59E+02	1.53E+02	8.92E+01	1.0
Xe-137	3.8 min	2.33E+04	6.59E+02	4.63E-01	1.0
Xe-138	14.1 min	1.12E+04	4.20E+03	5.86E+02	1.0
Other isotopes	<40 sec	4.76E+04	1.83E-05	0.00	0.25
Iodine					
I-131	8.0 days	1.10E-01	1.17E+00	3.85E+00	(2)
I-132	2.3 hr	2.56E+00	5.21E+00	1.00E+01	(2)
I-133	20.8 hr	2.07E+01	7.65E+01	1.21E+02	(2)
I-134	52.5 min	7.14E+02	1.58E+03	1.96E+03	(2)
I-135	6.6 hr	4.91E+02	4.86E+02	4.53E+02	(2)
Other isotopes	< 40 sec	4.51E+04	1.88E+02	9.69E+01	(2)
Br 90, 91	< 2 sec	3.56E+03	0.00	0.00	0.20

(1) Values from [Barbry 2009]

(2) ARF will be less than 0.01 for multiple excursions without boiling and less than 0.20 for excursions involving boiling.

Table 3-9 Curies of Important Nuclides Released from a Slow Cooker Event Over 8 Hours in Uranium Solution (based on 10^{18} fissions and 100 liters of solution)

(a) After 1-4 hour into Excursion

Nuclide	Half-Life	Radioactivity, Curies				ARF (1)
		After 1 hour into Excursion	After 2 hours into Excursion	After 3 hours into Excursion	After 4 hours into Excursion	
Krypton						
Kr-83m	1.8 hr	1.15E+00	5.05E+00	1.06E+01	1.66E+01	1.0
Kr-85	10.8 yr	1.58E-05	5.80E-05	1.23E-04	2.07E-04	1.0
Kr-85m	4.5 hr	1.66E+01	3.21E+01	4.54E+01	5.67E+01	1.0
Kr-87	76.3 min	1.01E+02	1.61E+02	1.96E+02	2.16E+02	1.0
Kr-88	2.8 hr	7.33E+01	1.31E+02	1.76E+02	2.11E+02	1.0
Kr-89	3.2 min	4.32E+02	4.32E+02	4.32E+02	4.32E+02	1.0
Kr-90 to Kr-98	<35 sec	9.75E+02	1.01E+03	1.04E+03	1.06E+03	0.25
Xenon						
Xe-133	5.2 days	2.00E-02	1.14E-01	3.01E-01	5.86E-01	1.0
Xe-133m	2.2 days	3.75E-03	1.27E-02	2.80E-02	4.99E-02	1.0
Xe-135	9.1 hr	3.31E+00	1.08E+01	2.15E+01	3.49E+01	1.0
Xe-135m	15.3 min	1.96E+01	2.95E+01	3.79E+01	4.55E+01	1.0
Xe-137	3.8 min	5.77E+02	5.77E+02	5.77E+02	5.77E+02	1.0
Xe-138	14.1 min	5.70E+02	6.00E+02	6.01E+02	6.01E+02	1.0
Other Xenon	<40 sec	9.93E+02	1.01E+03	1.04E+03	1.07E+03	0.25
Iodine						
I-131	8.0 days	2.00E-01	8.17E-01	1.61E+00	2.45E+00	(2)
I-132	2.3 hr	7.26E-01	2.28E+00	4.41E+00	6.94E+00	(2)
I-133	20.8 hr	9.62E+00	2.61E+01	4.42E+01	6.29E+01	(2)
I-134	52.5 min	1.92E+02	4.16E+02	5.69E+02	6.56E+02	(2)
I-135	6.6 hr	6.00E+01	1.14E+02	1.63E+02	2.07E+02	(2)
Other isotopes	< 40 sec	9.62E+02	9.89E+02	1.03E+03	1.07E+03	(2)

(1) Values from [Barbry 2009]

(2) ARF will be less than 0.01 for without boiling and less than 0.20 for excursions involving boiling.

Table 3-9 Curies of Important Nuclides Released (concluded)

(b) After 5-8 hour into Excursion

Nuclide	Half-Life	Radioactivity, Curies				ARF (1)
		After 5 hours into Excursion	After 6 hours into Excursion	After 7 hours into Excursion	After 8 hours into Excursion	
Krypton						
Kr-83m	1.8 hr	2.25E+01	2.77E+01	3.23E+01	3.61E+01	1.0
Kr-85	10.8 yr	3.08E-04	4.22E-04	5.49E-04	6.87E-04	1.0
Kr-85m	4.5 hr	6.65E+01	7.48E+01	8.20E+01	8.81E+01	1.0
Kr-87	76.3 min	2.28E+02	2.34E+02	2.38E+02	2.41E+02	1.0
Kr-88	2.8 hr	2.39E+02	2.61E+02	2.78E+02	2.91E+02	1.0
Kr-89	3.2 min	4.32E+02	4.32E+02	4.32E+02	4.32E+02	1.0
Kr-90 to Kr-98	<35 sec	1.08E+03	1.10E+03	1.12E+03	1.14E+03	0.25
Xenon						
Xe-133	5.2 days	9.69E-01	1.45E+00	2.02E+00	2.68E+00	1.0
Xe-133m	2.2 days	7.86E-02	1.14E-01	1.55E-01	2.02E-01	1.0
Xe-135	9.1 hr	5.03E+01	6.74E+01	8.57E+01	1.05E+02	1.0
Xe-135m	15.3 min	5.22E+01	5.83E+01	6.38E+01	6.88E+01	1.0
Xe-137	3.8 min	5.77E+02	5.77E+02	5.77E+02	5.77E+02	1.0
Xe-138	14.1 min	6.01E+02	6.01E+02	6.01E+02	6.01E+02	1.0
Other Xenon	<40 sec	1.10E+03	1.12E+03	1.14E+03	1.16E+03	0.25
Iodine						
I-131	8.0 days	3.30E+00	4.15E+00	5.00E+00	5.85E+00	(2)
I-132	2.3 hr	9.76E+00	1.28E+01	1.59E+01	1.92E+01	(2)
I-133	20.8 hr	8.13E+01	9.95E+01	1.17E+02	1.34E+02	(2)
I-134	52.5 min	7.03E+02	7.26E+02	7.38E+02	7.44E+02	(2)
I-135	6.6 hr	2.47E+02	2.82E+02	3.14E+02	3.43E+02	(2)
Other isotopes	< 40 sec	1.10E+03	1.13E+03	1.16E+03	1.19E+03	(2)

(1) Values from [Barbry 2009]

(2) ARF will be less than 0.01 for without boiling and less than 0.20 for excursions involving boiling.

Source terms for the three plutonium solution scenarios are given in Table 3-10 through Table 3-12.

- Table 3-10 provides values for the noble gases, iodine, and short-lived bromine (half-lives less than 2 seconds) in a single spike excursion involving plutonium solutions.
- Table 3-11 provides values for the noble gases, iodine, and short-lived bromine (half-lives less than 2 seconds) for multiple excursions involving plutonium solutions.

- Table 3-12 provides values for the noble gases, iodine, and short-lived bromine (half-lives less than 2 seconds) in a "slow cooker" excursion involving plutonium solutions.

All of the analyses were based on 100 liters of solution with a first spike yield of 10^{17} fissions or a total yield of 10^{18} fissions.

Table 3-10 Curies of Important Nuclides Released from First Spike in Plutonium Solution Criticality (based on 10^{17} fissions and 100 liters of solution)

Nuclide	Half-Life	Radioactivity, Curies			ARF (1)
		At end of Spike	10 min after spike	60 min after spike	
Krypton					
Kr-83m	1.8 hr	2.83E-07	3.66E-05	3.98E-04	1.0
Kr-85	10.8 yr	1.90E-09	2.38E-09	5.09E-09	1.0
Kr-85m	4.5 hr	9.61E-06	1.97E-03	1.94E-03	1.0
Kr-87	76.3 min	4.00E-03	1.28E-02	8.13E-03	1.0
Kr-88	2.8 hr	4.71E-03	7.66E-03	6.25E-03	1.0
Kr-89	3.2 min	3.76E-01	5.50E-02	9.18E-07	1.0
Kr-90 to Kr-98	<35 sec	2.96E+01	6.52E-06	0.00	0.25
Xenon					
Xe-133	5.2 days	1.34E-06	2.72E-06	1.89E-05	1.0
Xe-133m	2.2 days	1.15E-05	1.16E-05	1.26E-05	1.0
Xe-135	9.1 hr	6.16E-04	1.33E-03	3.03E-03	1.0
Xe-135m	15.3 min	5.27E-02	3.45E-02	6.02E-03	1.0
Xe-137	3.8 min	1.03E+00	2.87E-01	3.28E-05	1.0
Xe-138	14.1 min	3.00E-01	2.41E-01	2.05E-02	1.0
Other isotopes	<40 sec	6.83E+01	1.30E-03	6.13E-08	0.25
Iodine					
I-131	8.0 days	2.13E-06	1.96E-05	1.49E-04	0.01 (2)
I-132	2.3 hr	1.03E-03	1.10E-03	1.36E-03	0.01 (2)
I-133	20.8 hr	4.79E-04	2.11E-03	4.47E-03	0.01 (2)
I-134	52.5 min	3.92E+00	5.29E-03	2.84E-03	0.01 (2)
I-135	6.6 hr	2.93E-02	5.83E-02	6.47E-02	0.01 (2)
Other isotopes	< 40 sec	4.45E+00	5.29E-03	2.84E-03	0.01 (2)
Bromines	< 2 sec	1.27E+01	0.00	0.00	0.20

(1) Values from [Barbry 2009]

(2) ARF will be less than 0.01 for the single spike case

Table 3-11 Curies of Important Nuclides Released from Multiple Excursions in Plutonium Solution Criticality (based on 10^{18} fissions and 100 liters of solution)

Nuclide	Half-Life	Radioactivity, Curies			ARF (1)
		At end of 10 Min Excursion	20 min after Excursion End	60 min after Excursion End	
Krypton					
Kr-83m	1.8 hr	1.54E-03	1.32E-02	4.35E-02	1.0
Kr-85	10.8 yr	1.27E-01	2.12E-01	1.92E-01	1.0
Kr-85m	4.5 hr	2.12E-07	3.23E-07	5.34E-07	1.0
Kr-87	76.3 min	1.21E+00	1.12E+00	7.77E-01	1.0
Kr-88	2.8 hr	7.70E-01	7.21E-01	6.13E-01	1.0
Kr-89	3.2 min	1.99E+01	2.46E-01	3.70E-05	1.0
Kr-90 to Kr-98	<35 sec	3.54E+01	1.31E-10	0.00	0.25
Xenon					
Xe-133	5.2 days	1.94E-04	6.45E-04	2.09E-03	1.0
Xe-133m	2.2 days	1.15E-03	1.18E-03	1.27E-03	1.0
Xe-135	9.1 hr	9.90E-02	2.05E-01	3.13E-01	1.0
Xe-135m	15.3 min	4.29E+00	1.90E+00	5.35E-01	1.0
Xe-137	3.8 min	7.70E+01	2.15E+00	1.51E-03	1.0
Xe-138	14.1 min	3.09E+01	1.16E+01	1.62E+00	1.0
Other isotopes	<40 sec	8.48E+01	7.08E-03	2.68E-06	0.25
Iodine					
I-131	8.0 days	9.94E-04	5.85E-03	1.60E-02	(2)
I-132	2.3 hr	1.06E-01	1.19E-01	1.38E-01	(2)
I-133	20.8 hr	1.53E-01	3.29E-01	4.56E-01	(2)
I-134	52.5 min	4.74E+00	6.69E+00	6.33E+00	(2)
I-135	6.6 hr	1.73E+00	1.70E+00	1.58E+00	(2)
Other isotopes	< 40 sec	7.71E+01	7.50E-01	2.67E-01	(2)
Bromines	< 2 sec	0.00	0.00	0.00	0.20

(1) Values from [Barbry 2009]

(2) ARF will be less than 0.01 for multiple excursions without boiling and less than 0.20 for excursions involving boiling.

Table 3-12 Curies of Important Nuclides Released from a Slow Cooker Event Over 8 Hours in Plutonium Solution Criticality (based on 10^{18} fissions and 100 liters of solution)

(a) After 1-4 hour into Excursion

Nuclide	Half-Life	Radioactivity, Curies				ARF (1)
		After 1 hour into Excursion	After 2 hours into Excursion	After 3 hours into Excursion	After 4 hours into Excursion	
Krypton						
Kr-83m	1.8 hr	6.35E-01	2.74E+00	5.70E+00	8.92E+00	1.0
Kr-85	10.8 yr	1.25E-05	3.59E-05	6.86E-05	1.09E-04	1.0
Kr-85m	4.5 hr	6.87E+00	1.33E+01	1.88E+01	2.35E+01	1.0
Kr-87	76.3 min	3.76E+01	5.99E+01	7.28E+01	8.03E+01	1.0
Kr-88	2.8 hr	2.52E+01	4.50E+01	6.05E+01	7.26E+01	1.0
Kr-89	3.2 min	1.33E+02	1.33E+02	1.33E+02	1.33E+02	1.0
Kr-90 to Kr-98	<35 sec	2.10E+02	2.38E+02	2.42E+02	2.43E+02	0.25
Xenon						
Xe-133	5.2 days	3.08E-02	1.43E-01	3.52E-01	6.59E-01	1.0
Xe-133m	2.2 days	4.25E-02	9.02E-02	1.44E-01	2.04E-01	1.0
Xe-135	9.1 hr	7.52E+00	2.02E+01	3.58E+01	5.37E+01	1.0
Xe-135m	15.3 min	7.11E+01	8.44E+01	9.31E+01	1.01E+02	1.0
Xe-137	3.8 min	5.45E+02	5.45E+02	5.45E+02	5.45E+02	1.0
Xe-138	14.1 min	4.49E+02	4.73E+02	4.74E+02	4.74E+02	1.0
Other isotopes	<40 sec	4.74E+02	5.32E+02	5.32E+02	5.32E+02	0.25
Iodine						
I-131	8.0 days	2.62E-01	9.69E-01	1.85E+00	2.79E+00	(2)
I-132	2.3 hr	4.32E+00	9.45E+00	1.48E+01	2.02E+01	(2)
I-133	20.8 hr	1.17E+01	2.90E+01	4.75E+01	6.62E+01	(2)
I-134	52.5 min	2.25E+02	4.21E+02	5.43E+02	6.10E+02	(2)
I-135	6.6 hr	1.09E+02	1.14E+02	1.63E+02	2.07E+02	(2)
Other isotopes	< 40 sec	8.57E+02	9.65E+02	9.99E+02	1.01E+03	(2)

(1) Values from [Barbry 2009]

(2) ARF will be less than 0.01 for without boiling and less than 0.20 for excursions involving boiling.

Table 3-12 Curies of Important Nuclides Released (concluded)

(b) After 5-8 hours into Excursion

Nuclide	Half-Life	Radioactivity, Curies				ARF (1)
		After 5 hours into Excursion	After 6 hours into Excursion	After 7 hours into Excursion	After 8 hours into Excursion	
Krypton						
Kr-83m	1.8 hr	1.20E+01	1.48E+01	1.72E+01	1.93E+01	1.0
Kr-85	10.8 yr	1.57E-04	2.10E-04	2.69E-04	3.32E-04	1.0
Kr-85m	4.5 hr	2.75E+01	3.10E+01	3.39E+01	3.65E+01	1.0
Kr-87	76.3 min	8.47E+01	8.72E+01	8.86E+01	8.95E+01	1.0
Kr-88	2.8 hr	8.21E+01	8.96E+01	9.54E+01	1.00E+02	1.0
Kr-89	3.2 min	1.33E+02	1.33E+02	1.33E+02	1.33E+02	1.0
Kr-90 to Kr-98	<35 sec	2.44E+02	2.44E+02	2.44E+02	2.83E+02	0.25
Xenon						
Xe-133	5.2 days	1.06E+00	1.57E+00	2.16E+00	2.84E+00	1.0
Xe-133m	2.2 days	2.70E-01	3.42E-01	4.20E-01	5.03E-01	1.0
Xe-135	9.1 hr	7.33E+01	9.42E+01	1.16E+02	1.39E+02	1.0
Xe-135m	15.3 min	1.07E+02	1.13E+02	1.19E+02	1.24E+02	1.0
Xe-137	3.8 min	5.45E+02	5.45E+02	5.45E+02	5.45E+02	1.0
Xe-138	14.1 min	4.74E+02	4.74E+02	4.74E+02	4.74E+02	1.0
Other isotopes	<40 sec	5.32E+02	5.32E+02	5.32E+02	5.02E+02	0.25
Iodine						
I-131	8.0 days	3.74E+00	4.69E+00	5.65E+00	6.61E+00	(2)
I-132	2.3 hr	2.54E+01	3.05E+01	3.53E+01	4.00E+01	(2)
I-133	20.8 hr	8.47E+01	1.03E+02	1.20E+02	1.37E+02	(2)
I-134	52.5 min	6.46E+02	6.63E+02	6.72E+02	6.76E+02	(2)
I-135	6.6 hr	2.46E+02	2.82E+02	3.13E+02	3.42E+02	(2)
Other isotopes	< 40 sec	1.02E+03	1.03E+03	1.03E+03	1.06E+03	(2)

(1) Values from [Barbry 2009]

(2) ARF will be less than 0.01 for without boiling and less than 0.20 for excursions involving boiling.

For fuel reprocessing solutions, the releases depend on the fissile material driving the excursion. Both uranium and plutonium driven systems were analyzed with fission product and transuranic composition indicated in Table 3-13.

Table 3-13 Assumed Fission Product and Transuranic Nuclide Atom Density and Activity in Spent Fuel Solution Based on (ORIGEN calculations for 33 GWd/MT and 150-day cooling)

Nuclide	Atom Density $\left(\frac{\text{atoms}}{\text{barn-cm}}\right)$	Activity $\left(\frac{\text{Curies}}{\text{liter}}\right)$
Strontium-90	1.409E-06	31.58
Ruthenium-106	3.157E-07	188.96
Iodine-129	3.277E-07	0.000011
Cesium-137	2.206E-06	44.17
Cerium-144	5.068E-07	387.83
Promethium-147	2.985E-07	68.50
Plutonium-238	1.496E-07	1.01
Plutonium-239	5.879E-06	0.14
Plutonium-240	2.333E-06	0.21
Plutonium-241	1.269E-06	55.88
Americium-241	6.475E-08	0.083
Curium-242	5.894E-09	7.82
Curium-244	2.782E-08	0.92

The release amounts for the noble gases, iodine, and bromine will be the same as those for the driving excursion. That is, if the reprocessing system is dominated by uranium, then the values from Table 3-7, Table 3-8, or Table 3-9 should be applied as applicable. For a plutonium driven system, the values from Table 3-10, Table 3-11, or Table 3-12 should be applied as applicable. In any system containing plutonium, there is the potential for the plutonium release from any evaporated solution.

Following the assumptions given in BNWL-1697, Rev. 1 [BNWL 1975], it is assumed that 10 liters of solution are evaporated and that 0.02% of the plutonium mass in the solution is released. For example: if a solution has a concentration of 100 g Pu/liter, then:

$$100\frac{\text{g Pu}}{\text{liter}} \cdot 10 \text{ liters} \cdot 2\times10^{-4}\frac{\text{g Pu released}}{\text{g Pu}} = 0.2 \text{ g Pu released} \qquad (3\text{-}8)$$

The activity of the released plutonium is highly dependent on its isotopes, particularly on the ^{241}Pu content. Table 3-14 provides information on the specific activities of the plutonium isotopes and the approximate activities for a specified Weapons Grade (WG) and for a specified Reactor Grade (RG) composition. Based on a review of associated literature, these are typical values for the compositions of WG and RG fuels, and the specific activities were determined from published values for the isotopic half-life.

Table 3-14 Plutonium Isotopes, Specific Activities, and Estimated Activities per Gram of Weapons Grade and Reactor Grade Material

Nuclide	Specific Activity $\left(\frac{\text{Curies}}{\text{gram}}\right)$	Weapons Grade Atom Fraction	Activity per gram WG (Curies)	Reactor Grade Atom Fraction	Activity per gram RG (Curies)
Plutonium-238	17.13	0.0002	3.426E-03	0.0200	3.426E-01
Plutonium-239	0.06206	0.9424	5.849E-02	0.6220	3.860E-02
Plutonium-240	0.2271	0.0570	1.294E-02	0.2390	5.428E-02
Plutonium-241	103.73	0.0001	1.037E-02	0.1190	1.234E+01
Plutonium-242	0.003955	0.0003	1.187E-06	0.0000	0.000E+00
Total Activity/gram			8.523E-02		1.278E+01

[Barbry 2009] assumes a maximum release fraction of 1E-2 for the radioactive ruthenium in solution excursions as given in Table 3-6. It is expected this would be applicable to reprocessing solutions. For the reprocessing solution composition shown in Table 3-13 and assuming a 10- liter evaporation, this assumption gives a released activity of 17 Curies for ^{106}Ru. For solutions that do not contain ruthenium prior to the criticality, the small quantities generated in the criticality will not typically increase potential dose consequences outside of the facility.

As previously noted, the heat generated by the excursion results in heating of the liquid and the combination of density changes/micro-bubble creation rapidly terminates the reaction. Some of the liquid is assumed lost by evaporation and splashing. If the system again becomes critical with multiple excursions, then there is the potential for boiling. The assumption is that the boiling of 10 liters from a nominal 100 liter solution is sufficient to terminate the excursion.

3.2.2. Fully Moderated and Reflected Solids

As there are no historical criticality accidents involving these configurations, the ARF values are based on those from Table 3.2 of [NUREG 1997] and detailed in the Immediate Release Column of Table 3-15. Specific MAR values for fully moderated/reflected solids should be calculated using ORIGEN or other code systems.

The fission and activation products formed by an excursion in a solid are enclosed within the matrix of the solid fissionable material. The fissionable solids that are generally found in DOE non-reactor nuclear facilities are metal and ceramic oxides of the metals that may be clad in metal (e.g., aluminum, zircaloy, stainless steel). Because of the wide range of fissionable mixtures that may be used for fuel in the production, experimental, and test reactors at DOE sites, each generating its own spectra of irradiation products, fuel (unirradiated or spent) is not covered in this discussion.

It is postulated that the radionuclides generated by the criticality and present as fissionable material are in the solid matrix but covered by water, which acts as a moderator and reflector. Heat generated by the excursion is assumed to be dissipated in the water surrounding the fissionable

material resulting in boiling of the water. The criticality is ultimately terminated by density changes within the metal itself and the moderator due to heat generated.

The products contained in the matrix of the solid fissionable materials are not exposed to the ambient environment and would not constitute a source term hazard unless released from the matrix. Of the 16 historical excursions involving metal systems listed on Table 3-1(b), only 2 (with a total fission yields of 1.0×10^{16} and 3.8×10^{17}) exhibited any melting of the metal. Warping/oxidation are listed as consequences of 3 additional events (total fission yields ranging from 6×10^{16} to 6×10^{17} fissions). Therefore, a limited amount of softening/melting of the solid could be anticipated at the reference yield level of 1×10^{18} fissions, although this level is likely to be conservative. This softening/melting would not, however, cause significant disruption of the solid mass itself. It would most likely produce physical distortion of the material due to almost instantaneous melting and congealing from heat transfer to and interaction with water.

It is assumed that 1% (0.01 fraction) of the metal melts/softens due to the heat generated with most absorbed in the solution, thus allowing noncondensible gases and volatile radionuclides (radioactive iodine) in that fraction to be released. For powders or fines in solutions, the surface area to volume ratio of individual particles is considered sufficiently large that all noncondensible gases and radioactive iodine will escape.

For fully moderated and reflected metal solutions, Table 3-15 may be used. The values for the Immediate Spike are applicable to an immediate release of nuclides, while the values for the Lesser Spike bound the releases from criticality accidents in fully moderated metal systems with multiple excursions. Unless a criticality in a metal system melts some of the solid material, only the noble gases and iodine will be released. For metal system criticality accidents where a small amount of melt might occur, there might be some particulate release. The source terms for these scenarios are calculated using the new RF values from Table 3-15, but only applied to the amount of fission products in the melted mass.

Table 3-15 Release Fractions for Solid Systems Based on Table 3.2 from [NUREG 1997]

Nuclide Group	Release Fraction by Release Type	
	Immediate Release (Single Spike)	Lesser Spike followed by delayed supercritical excursion
Noble Gases (Kr, Xe)	0.4	0.4
Halogens (Br, I)	3.00E-03	3.00E-02
Alkali Metal (Cs, Rb)	3.00E-03	3.00E-02
Tellurium Group (Te, Sb, Se)	1.00E-04	1.00E-03
Barium, Strontium (Ba, Sr)	6.00E-07	6.00E-06
Noble Metals (Ru, Rh, Pd, Mo, Tc, Co)	6.00E-07	6.00E-06
Cerium Group (Ce, Pu, Np)	6.00E-07	6.00E-06
Lanthanides (La, Zr, Nd, Eu, Nb, Pm, Pr, Sm, Y, Cm, Am)	6.00E-07	6.00E-06

A review of work done on release fractions (RF) on spent fuel pool accidents under contract with the NRC [NUREC 1987 and NUREG 1997], indicates that these RF values are conservative and applicable to criticality accidents.

A small fraction (5E-4) of all non-volatile materials released to the moderator may be released to the ambient environment. Since quantities will be small and the excursion does not generate sufficient energy to fail particulate filters on the exhaust system, the contribution of the airborne nonvolatile materials to ex-facility doses is generally ignored.

If the material involved is a ceramic oxide powder, no melting/softening is postulated and no significant fraction of the non-volatile fission products generated are released. Due to the size of the individual particles in a powder, it is assumed that the fraction of volatile fission products (noble gases, iodine, ruthenium) present are so close to the surface that they are released in the fractions shown in Table 3-15 for the appropriate excursion type.

3.2.3. Dry Powder and Metal

This configuration covers solids (e.g., metal fines, loose oxide powders) that may be reflected but have no moderation (i.e., not immersed in liquid). There is no accident data for such systems dominated by fast neutron fissions. For large storage arrays, it should be easy to protect against an accident by appropriate packaging of individual items. For both of these fissile forms, the past Criticality Safety Evaluations have been able to document no credible accident sequences, and it is expected that this will continue in the future.

3.2.4. Large Storage Arrays

This configuration deals with driving together by external forces large amounts of material (i.e., reactor fuel storage arrays, extremely large quantities of fissionable materials). The total fission yield of 1×10^{20} is based on historical reactor excursions with moderation, and was originally developed in the Defense Programs Safety Survey solely for the purpose of evaluating criticalities in spent fuel storage pools when fuel was driven together. However, issues related to criticality and potential extreme excursions in storage environments are most appropriately handled in the arena of criticality safety evaluations performed by criticality safety professionals for the purpose of minimizing chances of occurrence. Design considerations relating to these issues should not be driven by unrealistic dose calculations from unattainable accident scenarios. If it is necessary to consider an upper bound of consequence, then a sire-specific analysis should be completed.

3.3. Summary and Conclusion

Changes in the Handbook – Regulatory Guides 3.33, 3.34, and 3.35 were relied on for the accident description and associated releases from solution criticalities. These three Regulatory Guides were withdrawn in 1999 and replaced by Regulatory Guide 3.71. However, Regulatory Guide 3.71 does not indicate that it incorporates the withdrawn Regulatory Guides although communication with the NRC specifies that is the case. The accident description remains the same in Regulatory Guide 3.71 (1998) and in revision 1 of the document (2005) by excepting the accident description of the ANS 8.10 standard. Revision 2 of the document (2010) drops the exception to the description of an accident in ANS 8.10 and implicitly accepts the accident descriptions provided in the ANS 8 Standards.

To accommodate the analyses of all reported process criticality accidents, a revision of the accident description was made. The accidents are now divided into 3 types: single spike, multiple excursions over a 10-minute period, and a slow cooker delayed supercritical system over 8 hours. Each of these was analyzed with the SCALE package using the TRITON-Depletion sequence to determine the activities of specific radionuclides at the end of the excursion and at various times after the shutdown of the excursion. For an excursion involving reprocessing solutions, ORIGEN-ARP runs were made to determine the actinide and fission product activities of such a solution. Then an excursion in this solution was modeled. It was determined that the addition of initial actinide content had negligible effect on the resulting activities.

A review of excursions other than those in solution systems indicated that assumptions in the previous version of the Handbook were overly conservative. Using information from the excursions, the accident scenarios and releases were updated.

All of the tables were updated if kept in the new version of the Handbook. Some new ones were added. Table 6-4 of the Handbook was combined into Table 3-1. Table 6-3 of the Handbook became Table 3-2 and Table 6-2 of the Handbook became Table 3-3. All tables were updated with the newly available information. Table 6-5 of the Handbook was revised to include information from [McLaughlin 2003] and [Barbry 2009] to become Table 3-4. Table 6-6 of the Handbook was replaced with a new Table 3-5 incorporating material for Tables 9 and 10 in McLaughlin et al. [McLaughlin 2000]. Table 3-5 was separated into two parts: one for uranium solutions and one for plutonium solutions. A new figure, Figure 3-1, was added to show maximum total specific fission yields [Barbry 1987]. A new table, Table 3-6, was added to provide ARF values from solution excursions [Barbry 2009]. Tables 6-7, 6-8, and 6-9 from the Regulatory Guides were replaced by Table 3-7 through Table 3-9 for uranium excursions and Table 3-10 through Table 3-12 for plutonium excursions. Data in the Tables was derived from the output of the T-DEPL sequence in SCALE. Table 3-13 was added, providing initial atom densities and activities for a reprocessing solution. These values were derived from ORIGEN-ARP calculations. Table 3-14 was added to provide plutonium isotopic, specific activities, and activities per gram of weapons grade (WG) and reactor grade (RG) material. Values were derived from published half-lives and averages of given compositions for WG and RG materials.

We reviewed the analytical models for fission yield in solution criticalities and selected [Barbry 1987, Tuck 1974] as the two that best fit the existing data from solution criticality excursions.

A review of work done on release fractions (RF) on spent fuel pool accidents [NUREG 1987 and NUREG 1997], indicates that these RF values are conservative and applicable to criticality accidents. These RF values are less conservative than those identified by [Restrepo 1992] in Table 6-10 of the previous edition of the Handbook, but after a review of the NUREG reports and what is likely to occur during criticality accidents (based on past accidents), these RF values are expected to be more realistic. These values were included as Table 3-15, replacing Table 6-10 of the Handbook.

4. Drum Fire Release Simulation using SIERRA/SM/FM

To enhance Chapter 5 of the Handbook, a simulation was added for a breach and combustion scenario involving the content of a 7A (55-gallon) waste drum. We proposed this addition because no such data existed previously and because a drum accident occurred recently at the Waste Isolation Pilot Plant, which prompted the review of any potential breach of waste drums. Using recent pipe over pack fire experiments conducted at SNL, a simulation using SIERRA/FM (Aria, Fuego) and SM (Presto) codes was completed to predict DR, ARF and/or RF.

The goal was to predict ARF values from a 7A steel drum, filled with contaminated trash, in or near a fuel fire. The physics required to capture a drum rupture due to over-pressurization are too complex to capture in a single code, nor does such a code exist. This work coupled three simulations (heat transfer, solid mechanics, and fluid dynamics) to encompass the full behavior of the drum failure. Real-time coupling of all three simulations was outside the scope of this work, so a one-way coupling scheme was adopted. The coupling method began by simulating the trash decomposition in the drum using Aria, which also provided the temperature distribution and internal pressure.

Aria is a finite element, multi-physics, heat transfer code capable of simulating transient, implicit and nonlinear equations in three dimensions, solving thermal energy and species transport equations [SIERRA 2017]. The temperature and pressure data output from Aria were then transferred to Presto which predicted the thermal mechanical response of the drum and decomposition of the lid gasket.

Presto is a Lagrangian code capable of solving explicit dynamic, implicit quasi-static and dynamic problems in three dimensions. As with all Sierra tools used in this study, Presto can be run in parallel on high-performance computing architectures. An iterative method was employed to effectively calculate the area of the vented region after the drum ruptured, as the opening of the drum would result in a reduction in pressure due to the breach. Using a choked flow assumption, the internal pressure was recalculated around the time of rupture. The Presto simulation was rerun with the ventilated pressure values, and provided a revised vented opening area vs. time history. Finally, the breach area was used as an input to the Fuego to predict the contaminant release.

Fuego is a low Mach, Eulerian fire code which solves the Naiver-Stokes equation for reacting flows, capable of simulating particle dynamics using a Lagrangian/Eulerian two-way coupling scheme. Fuego is coupled with the SIERRA Participating Media Radiation Module, Syrinx, a discrete ordinate method radiation code. Figure 4-1 illustrates how the three codes interact and transfer information.

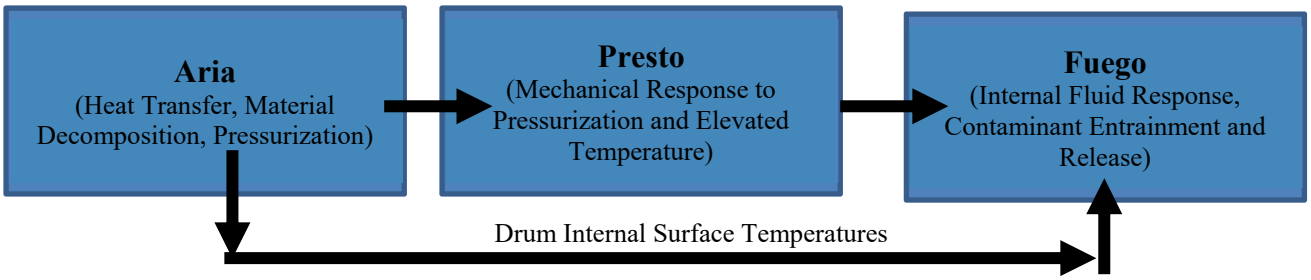

Figure 4-1. Sierra Coupling Scheme

4.1. Problem Definition

In order to conduct this simulation using code coupling as described in Figure 4-1 for the drum rupture release due to a fire scenario, two experimental sets were drawn upon for simulation parameters, specifically the applied heat flux to the drum, drum geometry, an initial mass for the trash, and a contaminant injection parameter based off of the amount of trash decomposition. One experimental data set [Figueroa 2017]relates to the response of a drum in a fuel fire environment, while the other [Mishima 1973] informs the contaminant release from burning contaminated trash.

A specific study regarding contaminant release from a drum surrounded by a fire was not found in a review of the literature. Various studies have investigated contaminant release from burning trash materials [Mishima 1973], 55-gallon drums in fires [Figueroa 2017, Yang 2007] or contaminant release from historical accidents [Wilson 2014]. Lacking a fully representative experimental study which exactly matched the desired scenario, inference was drawn from the obtainable data sets. The estimated ARF and RF values presented here cannot be considered validated, but they can provide some insights.

4.1.1. FLAME Pool Fire Experiments

Several studies on steel 55-gallon (7A) drums containing trash were performed in the FLAME facility located at the Thermal Test Complex at SNL in March of 2016. These tests were similar to the desired simulations, and were performed under an unrelated effort. The tests lacked only the contaminant release. The drums were filled with waste typically produced in facilities which handle radioactive contaminants, mostly plastics and cellulosic materials and placed at various locations around a three-meter pool fire of Jet-A fuel, which burned for 30 minutes. An image of the tests can be seen in Figure 4-2. The anticipated heat flux at the front face of the drums was 55 kW/m^2, and the actual value was quite close, roughly 60 kW/m^2. The drums were not instrumented for temperature measurements; however, their pre- and post-test weights were recorded.

Figure 4-2. Four 55-gallon drums containing assorted trash on the circumference of a three-meter pool fire.

The contents of the drum were examined pre- and post-test, and it was observed that the trash had settled, decomposed, and charred, as seen in Figure 4-3. The composition of the materials was not examined in detail as shown in this figure. Post-test measurements determined that the drum had lost 4 lbs. (2 kg) of mass, which was assumed to be exclusively related to the trash decomposition and gas venting. The interior paint was in various states of decomposition and had flaked off from the side nearest the flames. The gasket seated in the drum lid had decomposed completely on the side that faced the fire, creating a potential leak path.

(a) (b)

Figure 4-3. a) Pre-test drum trash b) Trash remnants inside a 55-gallon steel drum after being exposed to a 30-minute fire.

4.1.2. RART Trash Fire Experiments

Previous work investigating contaminant release from a trash containment vessel was performed by Mishima & Schwendiman in 1973 in the Radioactive Aerosol Release Facility (RART) at Pacific Northwest Laboratories in Richland, Washington [Mishima 1973]. Eleven experiments were performed where a corrugated cardboard box was lined with a polyethylene bag, which was subsequently filled with general laboratory trash and either uranium dioxide (UO_2) powder or uranium nitrate (UNH) solution was distributed throughout the trash. The cardboard carton was tested in two configurations: unsealed and sealed with masking tape. The box was placed on a metal screen inside the RART and ignited remotely by an oil soaked cloth fuse and coil.

The trash composition in the RART experiments was similar in nature to the trash composition in the FLAME pool fire experiments. The compositions for both sets of experiments are listed in Table 4-1, where the FLAME values stem from a single experiment and the RART values represent an average of the eleven tests.

Table 4-1. Average mass fraction composition of waste materials in FLAME and RART contaminant release experiments

Material	FLAME Experiment (2016)	RART Experiment (1973)
Cardboard	Included in paper weight	17.5% (15.7-20.9%)
Paper	17.6% (4.98 lbs.)	41.1% (31.7-43.9%)
Plastic	75.7% (21.47 lbs.)	9.7% (8.0-14.4%)
Rubber	6.7% (1.9 lbs.)	2.4% (1.8-4.2%)
Miscellaneous (Rags, Oil, Tape, Other)	None	29.3% (23.8-38.2%)

In the RART experiment, contaminant was collected on foil strips taped to the walls and with fallout trays on the floor containing a thin oil layer. Glass fiber and cascade impact filters were inserted regularly into the chamber during the test to analyze the size distribution and quantity of airborne contaminant. Various solutions were used to extract the deposited contaminant post-test. A 9N nitric-0.1N hydrofluoric acid solution was used to remove the contaminant from the filters, glass impactor dishes, and general residue, then evaporated. 6N nitric acid was used to take up the residue. For the fallout trays, the oil was filtered through #41 Whatman filter paper. The Aluminum foil wall strips were soaked in a dilute sodium hydroxide solution until the foil dissolved completely. The resultant liquid was filtered through #41 Whatman filter paper and rinsed with distilled water. Both Whatman filter paper sets were treated as the above filters and glass dishes. The amount of contaminant was measured by fluorimetry. From these measurements, an ARF and RF were determined.

The measured deposition on the air filters (representing the ARF) ranged from 0.003 to 0.053 wt%, while the wall deposition ranged from 0.0029 to 0.23 wt%. The floor had the highest concentration of contaminant ranging from 0.01 to 1.7 wt%. The contaminant deposited on the walls could be considered airborne in absence of an enclosure; therefore, combining the Airborne mass and the wall mass, the maximum ARF seen in the experiments was 0.24 wt%. Mishima and Schwendiman report no appreciable difference in the ARF between the various packaging configurations.

One note from the RART experiments is that the report mentions that the standard packaging configuration was transitioning from corrugated cardboard boxes to the metal drums currently used while the experiments were being performed.

4.2. Simulation Methods

Based on the simulation strategy as described in Figure 4-1 this section describes a detailed approach used for the modeling the problem definition discussed in the previous section.

Various simulation tools were used to capture the complex physics involved for a drum failure caused by a fire. The SIERRA (version 4.44) computational suite enabled the necessary transfers for coupling between various physics codes by providing the underlying communication and transfer framework required to pass information between codes. The SIERRA/Thermal Fluids (TF) tool Aria calculated the thermal response on the drum, trash decomposition, and pressurization from a fire-like radiation flux of 61 kW/m^2. The pressure and temperature output was then passed to the SIERRA/Solid Mechanics (SM) tool Presto as respectively as internal and external boundary conditions to predict the thermal mechanical response as the pressure and temperature increased. Presto provided a breached area vs. time correlation calculated once a ventilation path opened and as the gasket decomposed. An adjustment to the pressure vs. time correlation was made based on the breach area vs. time from the Presto simulation. As the vented area increased, the internal drum pressure was recalculated using the choked flow assumption shown below,

$$\dot{m} = C_d A_i P_i \sqrt{\frac{k}{R_g T_i} \frac{2}{k+1}^{\frac{k+1}{k-1}}} \tag{4-1}$$

where $\dot{m}$ is the mass flux through the vent, C_d is the discharge coefficient (taken to be 0.72), A_i, P_i, and T_i are the vented area, pressure, and temperature at the current time-step respectively, k is the heat capacity ratio for the fluid, R_g is the gas constant. Equation 4-2 must be satisfied for the choked flow equation to be valid,

$$\frac{P_{atm}}{P_i} < C_r \tag{4-2}$$

where P_{atm} is the atmospheric pressure and C_r is the critical ratio defined in Equation 4-2 (0.528 for air).

$$C_r = \frac{2}{k+1}^{\frac{k}{k-1}} \tag{4-3}$$

Presto was rerun with the new pressure values, producing a modified breach area vs. time result. Once the Presto simulation calculated a significant and persistent rupture area, the vented area vs. time relation was passed to the SIERRA/TF CFD tool Fuego, which uses Lagrangian particles to simulate the behavior of the contaminant. The particles were injected inside the drum model based on the material mass loss calculated by Aria. The injection parameters were generated assuming that particles were entrained as the trash decomposed. Using the initial contaminant to trash ratio from Mishima & Schwendiman [1973], a value was determined for the entrained contaminant mass of 0.011 kg over the 500 seconds prior to the ventilation path opening. The CFD simulation for the contaminant particle release was run with a vent area of 2.0×10^{-3} m^2, corresponding to the highest breach area peak observed in the Presto simulation.

4.3. Drum Thermal Fluid Model: Heat Transfer

SIERRA/Thermal Fluids (TF) tool Aria was used to model the heat transfer from a fire-like boundary condition. A flux of 61 kW/m^2 was applied to the outer drum surface to simulate incident radiation from a nearby fire. The interior of the drum contained two regions: an air region and a trash region. The air region occupied 90% of the interior volume and was allowed to pressurize as the temperature increased. The trash region had reaction kinetics to model the decomposition as the temperature increased. The pressure and temperature results were passed to the thermal mechanical model after the simulation ran for an hour of real time, twice the experimental duration in the FLAME study. The pressure values are needed for an internal boundary condition in the thermal-mechanical model, while the temperature values were used in thermal expansion calculations and for prediction of the gasket degradation.

4.1.3. Model Description

This section describes the model used in the drum fire release simulation. The intent is detailed models of the input parameters needed, trash decomposition, computational meshes, and boundary/initial conditions for the simulation.

4.1.3.1. Model Input Parameters

The drum walls were modeled as carbon steel [Bergman 2011] and the interior of the drum was divided into two regions, one for air and the other for the trash. A decision was made to deviate from the composite trash mixture in the FLAME test series to a purely cellulosic trash material for consistency, despite the greater mass fraction of various plastics. The reasoning was that the numerous plastics were not explicitly documented, therefore ascribing kinetic values to the types of plastics would not be accurate. Cellulose kinetics represented the entirety of the "cellulosic materials" and were therefore chosen for their certainty. It was also assumed that the ventilation plug was clogged and could not release any built-up pressure, representing the presumed "most stressing scenario" which also localized the release to a failure around the drum lid.

4.1.3.2. Trash Decomposition

A two-step Arrhenius reaction (Eq. 4-4) for cellulose was employed to model the trash decomposition as a function of temperature.

$$r_n = \bar{\rho} Y_R A_n e^{\frac{E_n}{R_u T}} \tag{4-4}$$

where r_n is the reaction rate, A_n and E_n are the reaction-specific pre-exponential factor and activation energy respectively, R_u is the universal gas constant, T is temperature, Y_R is the mass fraction of the trash, and $\bar{\rho}$ is the average density. The parameters for the reaction can be seen in Table 4-2 [Diebold 1994, Lewellen 1976]. The second reaction produces a variety of gases, outlined in Table 4-3, which are included in the internal pressurization calculation as they are produced.

Table 4-2. Arrhenius Reaction Values for Two-Step Cellulose Decomposition

Value	Reaction 1	Reaction 2
Pre-exponential Factor (A_n, s^{-1})	2.80E19	6.79E9
Activation Energy (E_n, kJ/kmol)	2.4E5	1.45E5

Table 4-3. Trash Decomposition Gases

Gas Species	Mass Fraction
CO	0.487%
CO_2	0.418%
Lignocellulose (represented as $C_{12}H_{23}$ due to the similarities in molecular weight)	0.080%
H_2	0.015%

4.1.3.3. Computational Mesh

The mesh was modeled after a steel 55-gallon drum, described in detail in a later section. The mesh, shown below in Figure 4-4, consisted of 1,213,579 hexahedral elements to represent the drum components and internal air and trash regions. The element volume ranged from 3.41×10^{-9} to 5.36×10^{-7} m^3, with an average size of 1.81×10^{-7} m^3. The mesh had an average aspect ratio of 3.36, with a minimum and maximum of 1.0 and 14.1 respectively. The average skew was 0.093, with a maximum skew of 0.76.

Figure 4-4. Drum Assembly Thermal Fluid: Heat Transfer Mesh

4.1.3.4. Boundary and Initial Conditions

The heat transfer simulation started at ambient conditions, with a 61 kW/m^2 peak flux boundary condition applied to the surface nearest the fire, decreasing in intensity around the perimeter to the back face, as seen in Figure 4-5. The light blue region represents the air inside the drum, while the light green region represents the contaminated trash.

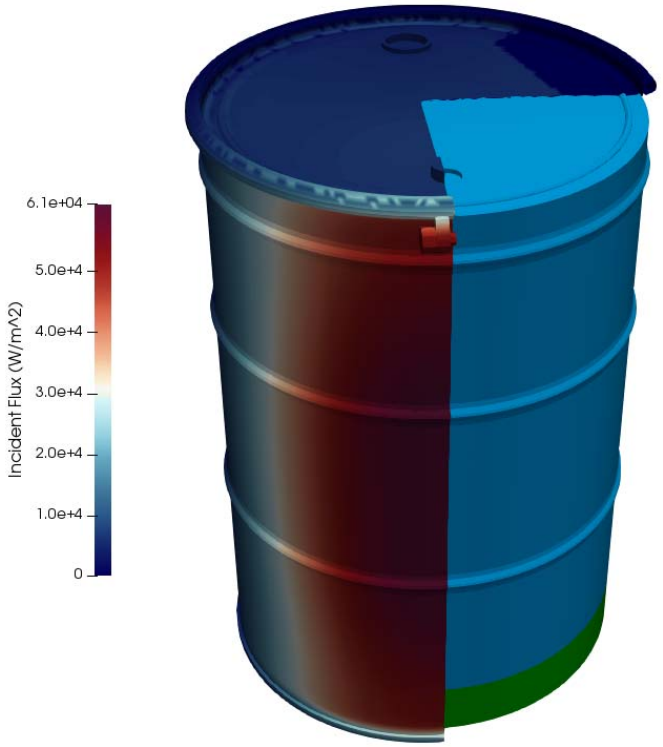

Figure 4-5. Cutaway Aria drum mesh with applied fire heat flux. Blue block is air region; green block is cellulosic waste.

4.1.4. Results

Direct comparisons of the Aria results to the FLAME experiments can be made with regard to the approximate mass loss. While the material was modeled as pure cellulose, the mass loss was comparable to the FLAME experiments. The experimental mass loss was 1.8 kg, while the simulation predicts a mass loss of 2 kg at half an hour (Figure 4-6). The temperature of the fluid (Air) region as a function of time was fit to a cubic equation, seen below, where t is time and T is temperature.

$$T = 2.7\times10^{-7}t^3 - 6.6\times10^{-4}t^2 + 0.62t + 298 \quad (4\text{-}5)$$

The mass loss values matched reasonably to the experimental values. This agreement builds confidence in the model.

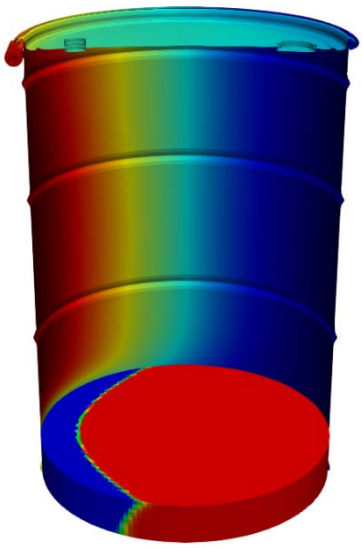

Figure 4-6.Trash decomposition at 30 minutes and drum temperature. The red in the lower layer represents unreacted trash, while the blue represents reacted trash.

4.4. Drum Thermal Mechanical Model

SIERRA/Solid Mechanics (SM) was utilized to determine the thermal-mechanical response of the drum and to predict the formation of ventilation paths resulting from the internal pressurization and heating of the drum. While the internal pressurization process and resulting formation of leakage paths is directly coupled (i.e., the formation of leakage pathways produces a drop in the internal pressure of the drum, which in turn affects the leakage path formation and the internal pressure), only two simulations were performed for this work, with the first simulation making use of the internal pressure determined from the Aria simulation (which assumed a sealed drum enclosure), and a second simulation using a modified time-pressure relationship that accounts for the depressurization of the drum that would result from the formation of the vent paths predicted by the first simulation. The resulting time versus drum breach area relationship predicted by the second simulation was used in the subsequent SIERRA/TF particle transport simulation. Two simulations are sufficient as the formation of even a relatively small vent path produces a relatively quick depressurization of the drum. Due to time constraints and the challenges associated with getting an implicit dynamics solver to work for this problem, a mass-scaled explicit dynamics simulation was performed instead.

4.1.5. Model Description

This section describes the drum's thermal-mechanical model, which includes the input parameters, mesh, initial and boundary conditions, and gas gasket failure assumption.

4.1.5.1. Model Input Parameters

The drum assembly consists of a carbon steel (ASTM A1008) drum body, drum lid (with bung hole/cap, and vent hole/vent-assembly), and closure ring; a cellular expanded sponge rubber

(ASTM D1056) gasket (attached to the lid); and a carbon steel (ASTM A307) closure ring bolt - Figure 4-6. The thermal-mechanical model makes use of the *thermoelastic_plastic_fail* material model (SIERRA/SM 4.44) which is a metal plasticity model that allows for temperature dependences to be defined for the elastic constants, yield stress, hardening behavior, and failure parameters. Temperature dependent material model parameters for each material were derived from several sources, including the American Society of Mechanical Engineers (ASME) Boiler and Pressure Vessel Code (ASME BPVC 2015), various material specifications (ASTM A1008, ASTM D1056, and ASTM A307), and in the case of the drum body and lid steel, material test data obtained for another program (Wilson et. al, 2015). Additionally, thermal expansion/contraction-versus-temperature behavior was defined for each material based on data obtained from the ASME Boiler and Pressure Vessel Code (ASME BPVC 2015). It is worth noting that numerical issues stemming from contact between the relatively soft gasket material elements and the drum body were observed in several of the simulations. Such issues are not uncommon in finite element simulations involving contact between two components with widely differing stiffness. These issues stem from how the contact interactions are enforced between the two components. While there are techniques to alleviate these issues, the can be time consuming to implement correctly. Instead, for the purposes of the simulations described here, the gasket material was arbitrarily stiffened and assigned a higher density. (In particular, the gasket was modeled as a linear elastic material with a modulus of elasticity, Poisson's ratio, and density equal to steel). While not technically correct, earlier simulations demonstrated that the behavior of the drum system for this particular problem is relatively insensitive to the gasket material properties.

4.1.5.2. Computational Mesh

Dimensions for the drum utilized in the thermal-mechanical simulations were derived from the ANSI MH2-1991 specification (ANSI MH2-1991). The half-symmetry mesh consists of a total of 469,396 hexahedral elements. The element volume ranged from 1.72×10^{-8} to 1.80×10^{-6} m^3, with an average of 2.26×10^{-7} m^3. The aspect ratio averaged 9.75, with a minimum of 1.1 and a maximum of 18.2.

4.1.5.3. Boundary and Initial Conditions

The first thermal-mechanical simulation made use of the internal pressure loading (Figure 4-7) and drum component temperatures derived from the Aria simulation (Figure 4-8 and Figure 4-9). The internal pressure was applied to the inner surfaces of the drum body and lid using a tabular time-versus-pressure function. The internal pressure function was derived directly from the Aria simulation output data. The internal pressure calculated by Aria is absolute, so a compensating external pressure equal to atmospheric pressure was applied to all exterior surfaces of the drum body and lid. Material temperatures were mapped from the Aria mesh results using an internal mapping algorithm for dissimilar meshes within SIERRA/SM.

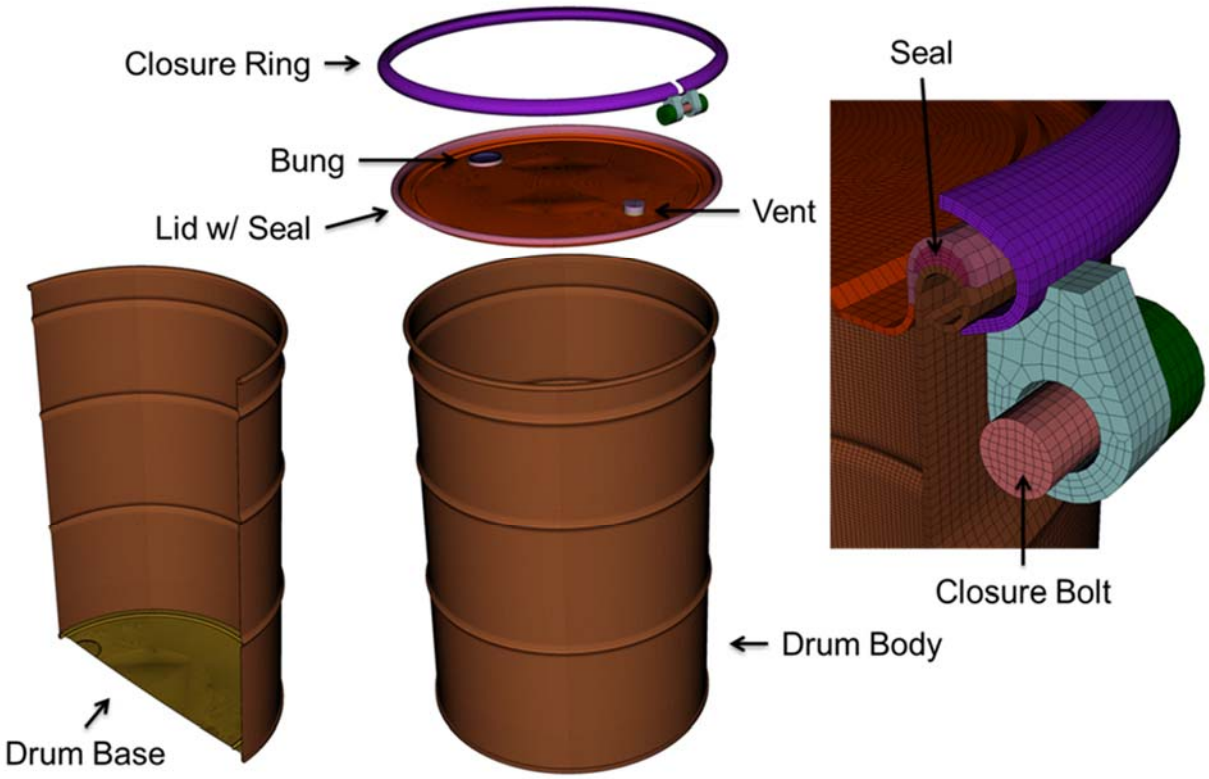

Figure 4-7 Drum Assembly Thermal-Mechanical Model Mesh.

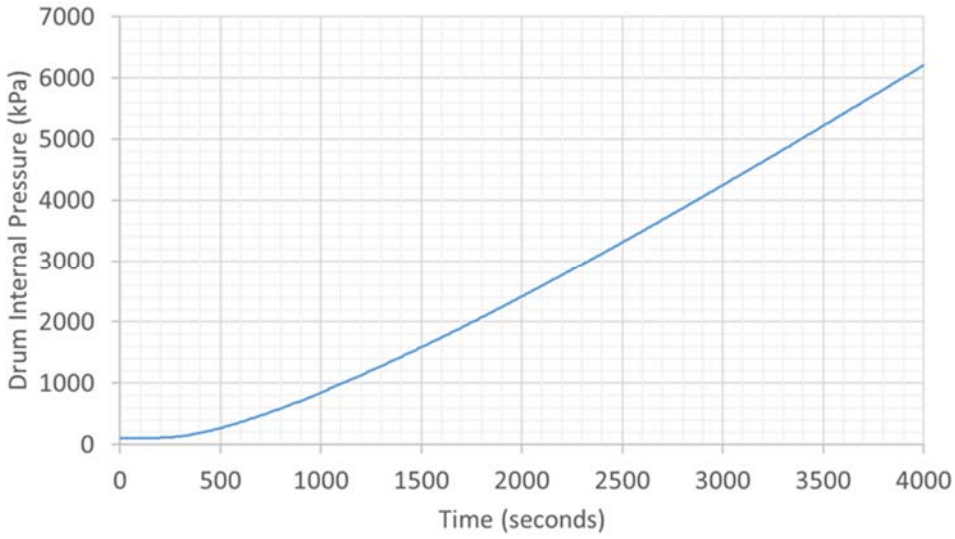

a) Time: 0 to 4000 Seconds

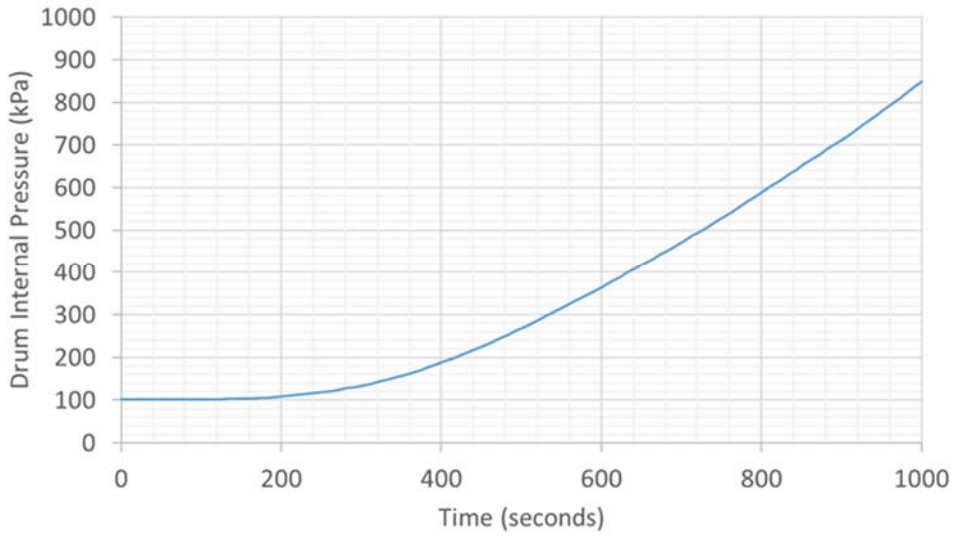

b) Time: 0 to 1000 Seconds

Figure 4-8. Predicted Drum Internal Pressure from Aria Simulation.

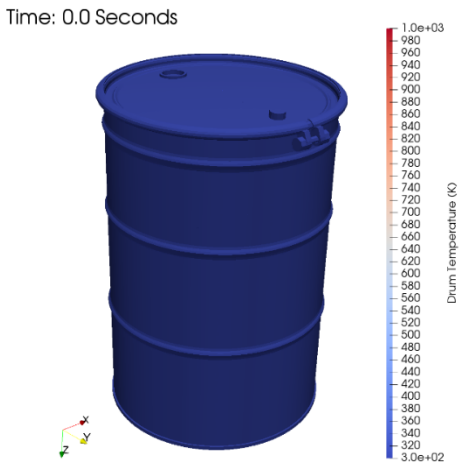

a) Time: 0 Seconds

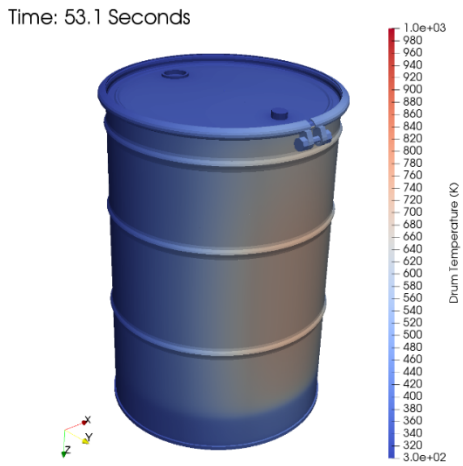

b) Time: 53.1 Seconds

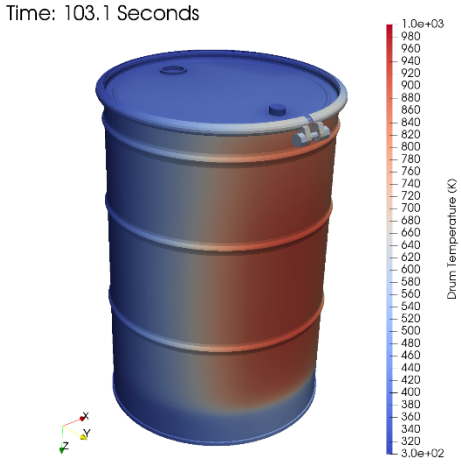

c) Time: 103.1 Seconds

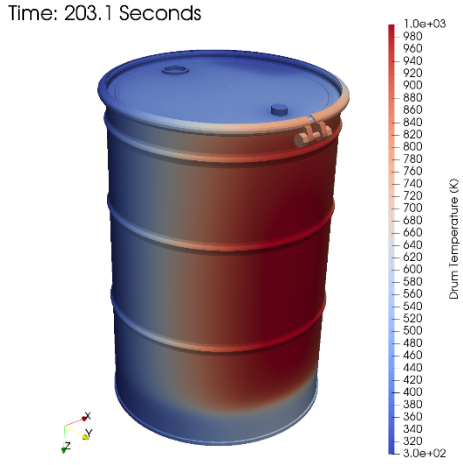

d) Time: 203.1 Seconds

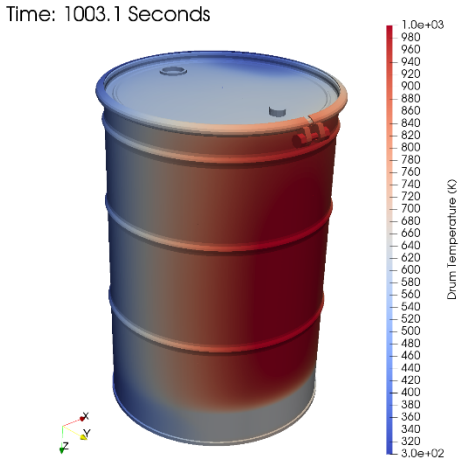

e) Time: 1003.1 Seconds

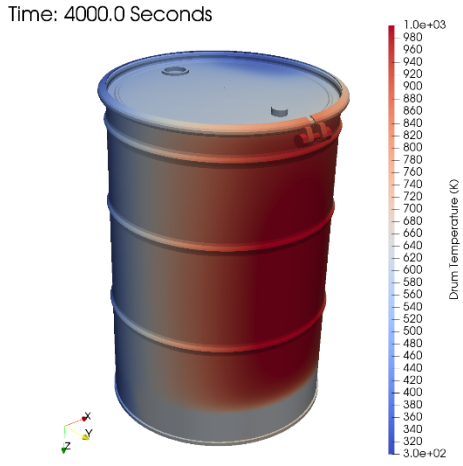

f) Time: 4000.0 Seconds

Figure 4-9. Drum Temperatures from Aria Simulation (Several Snapshots in Time).

In both simulations, the drum was restrained from vertical translation along a single circumferential line of nodes at the base of the drum. As the model is half-symmetric, symmetry boundary conditions were applied to all drum body, drum lid, closure ring, and closure bolt nodes that lie on the symmetry plane. To restrain the drum model against lateral motion parallel to the symmetry plane, a single node at the center of the drum body base was fixed against translation parallel to the symmetry plane. The drum lid, closure ring, and closure bolt were secured in place on the drum through contact interactions. Contact was established between these components during the first ten seconds of each simulation by reducing the closure ring bolt length, simulating the preloading of the bolt. The amount of bolt preload was selected to produce a closure of the ring that left an approximately 6 mm gap between the ends of the closure ring at the bolt. This gap was selected to match the closure ring gap observed on the drum of interest from the FLAME facility test. A low (0.05) coefficient of friction was assumed to ensure proper seating of the closure ring.

4.1.5.4. Gasket Failure

During the FLAME facility tests, decomposition of the cellular expanded sponge rubber gasket was observed. To approximate the degradation of the seal resulting from its exposure to high temperatures, the thermal-mechanical model included a temperature based criterion that removed gasket elements from the simulation when their temperature exceeded 675 °K. This failure temperature was selected based on an approximate decomposition temperature for (high Density Polyethylene (HDPE) [Kumar 2013].

4.1.6. Results

This section describes the results for two simulations – one assumes no depressurization, and one assumes with depressurization.

4.1.6.1. Simulation 1: No Depressurization

The first simulation shows how the drum behaves if no depressurization is assumed. Figure 4-10 shows the resulting behavior of the drum in this simulation from the point before lid failure (a) and lid loss (b). As shown in (a) of this figure, by 675 seconds, the continuously increasing internal pressure has overwhelmed the ability of the closure ring to retain the lid, at which point the lid and remaining portion of the gasket fly free. Yielding in the closure ring at the bolt is the failure mechanism precipitating loss of the lid (see (b) of this figure). However, significantly before the lid is lost, at about 254 seconds, portions of the gasket begin to experience temperatures in excess of its decomposition temperature. This results in the loss of seal integrity at 384 seconds and breach of the drum at the seal (Figure 4-11). Figure 4-12 shows the calculated breach area versus time resulting from the simulation. It is interesting to note that after the initial growth of the breach area resulting from continued decomposition of the gasket, mechanical deformation of the lid acts to reduce the overall breach area, as evidenced by the precipitous drop in breach area between 500 and 510 seconds (Figure 4-13). Figure 4-12 also includes an estimate of the drum internal pressure taking into account venting of the drum internal gases that would occur as a result of the breaching of the drum (green dotted line versus green solid line, respectively). Despite the breach area being relatively small (ranging between 15 mm^2 and 40 mm^2 during the depressurization), the drum completely depressurizes, taking about 56 seconds (spanning form 384 seconds to 440 seconds) to do so. This depressurization will preclude failure of the closure ring and loss of the lid later in the simulation; however, Figure 4-12 does indicate that as the breach area is again reduced due to

mechanical deformation of the lid (dropping to about 20 mm^2 at time 508 seconds), the reduced ability to vent gases from the drum and the continued introduction of decomposition gases within the drum, produce a pressure increase (from about 101 kPa at 505 seconds to 108 kPa at 562 seconds) that is only relieved when the breach area again increases around 570 seconds. The resulting behavior of the drum for the updated pressure loading was determined in a subsequent simulation (simulation #2), the results of which are described in the next section.

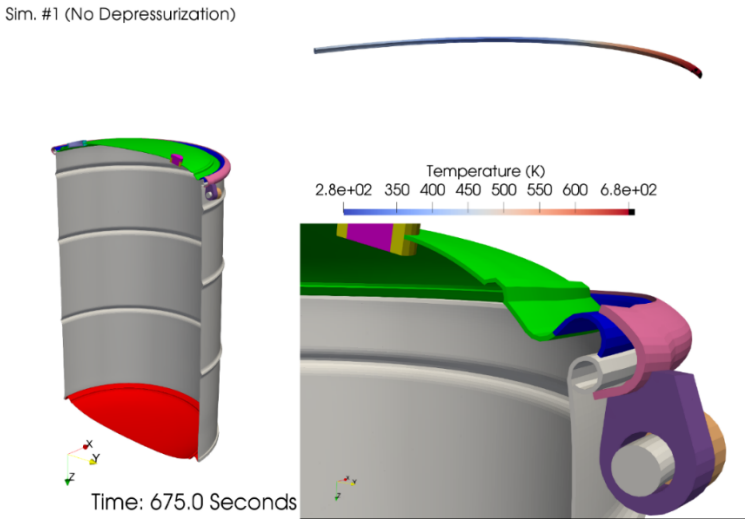

a) 675 Seconds – Yielding in Closure Ring and Loss of Lid

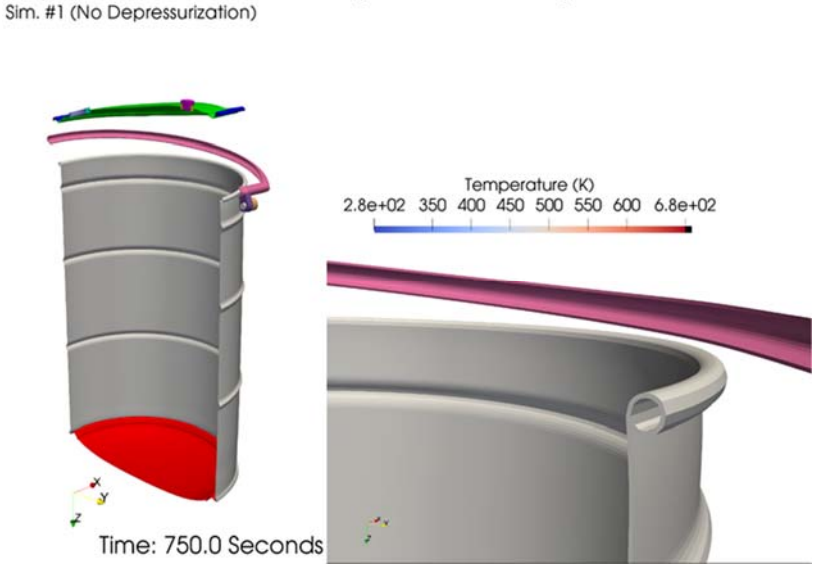

b) 750 Seconds – Free Flying Lid

Figure 4-10 Simulation 1: Loss of Lid.

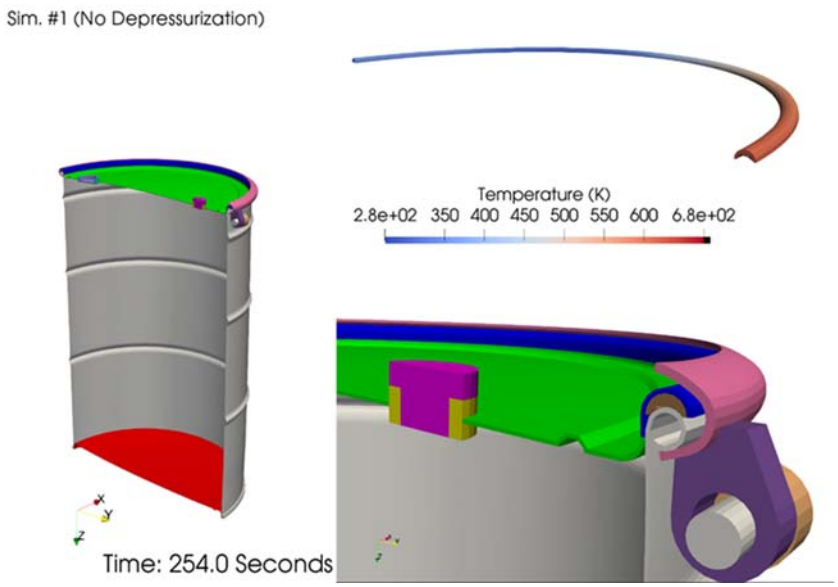

a) 254 Seconds – Seal Temperature First Exceeds Decomposition Temperature (675 °K)

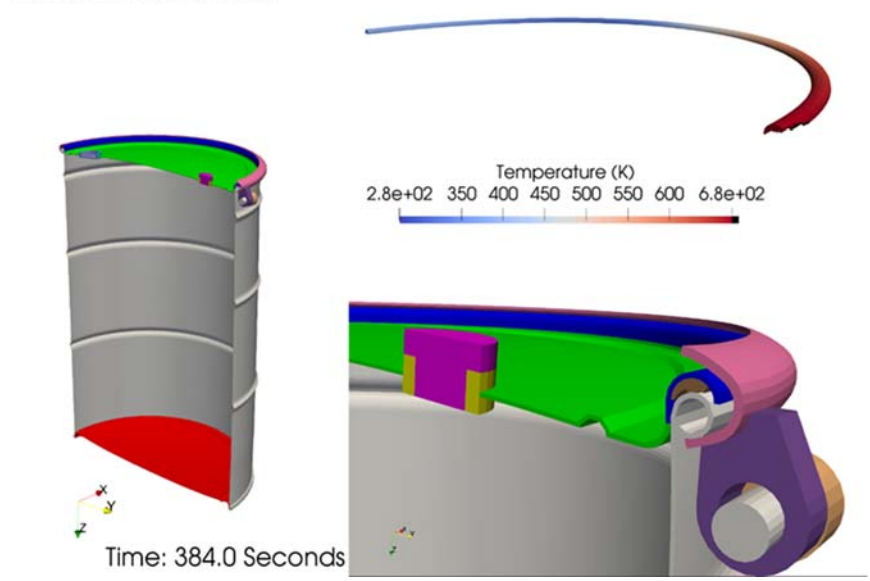

b) 384 Seconds – First Loss of Seal Integrity

Figure 4-11 Simulation 1: Loss of Seal Integrity.

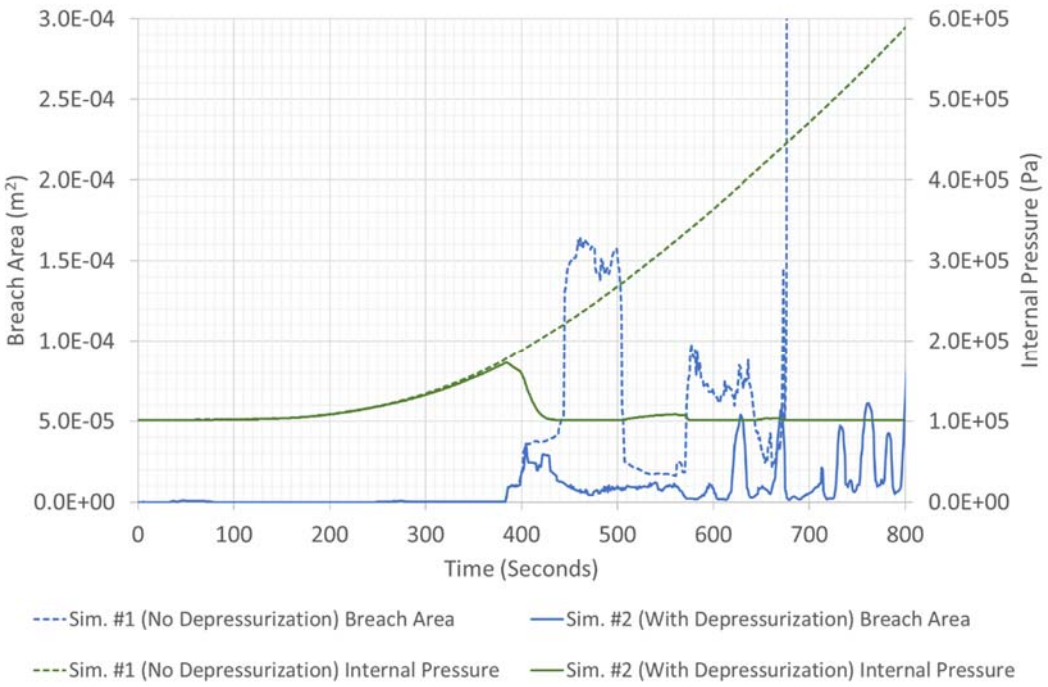

Figure 4-12 Internal Pressure and Breach Area vs. Time (Simulations #1 and #2).

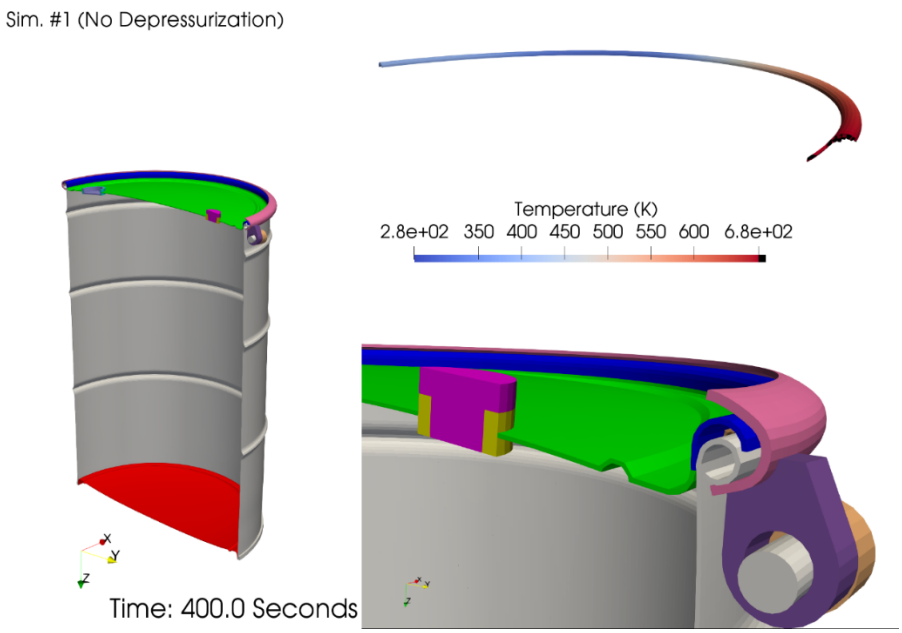

a) 400 Seconds – Significant Breach at Seal Due to Seal Decomposition

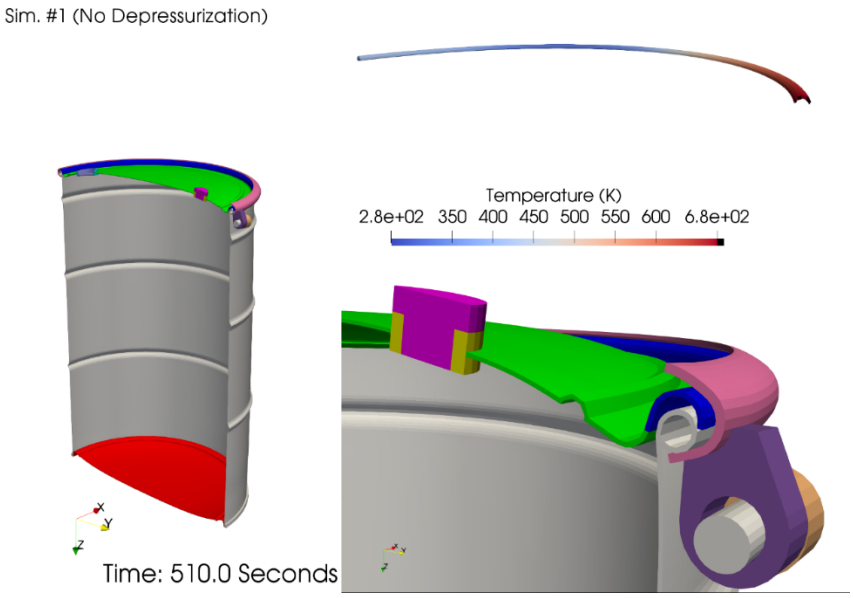

b) 510 Seconds – Reduced Breach at Seal Due to Mechanical Deformation of Lid

Figure 4-13 Simulation 1: Reduction in Breach Area Due to Mechanical Deformation of the Drum Lid.

4.1.6.2. Simulation 2: With Depressurization

This section provides the results for the simulation that accounts for depressurization of the drum. Figure 4-14 shows the behavior of the drum in the second simulation. Depressurization of the drum between 384 seconds and 440 seconds (Figure 4-15) eliminates the possibility of failure of the closure ring and loss of the lid. As was true in the first simulation, decomposition of the seal begins

to occur at 254 seconds, with loss of seal integrity occurring at 384 seconds. Loss of seal integrity produces a reduction in the internal pressure of the drum and a change in the breach area versus time response. Figure 4-12 includes the resulting breach area for the drum following the depressurization. At about 405 seconds (during the depressurization) the breach area in simulation #2 begins to diverge from that of simulation #1, with the breach area in simulation #2 dropping below that predicted in the first simulation. Following the depressurization, the breach area in simulation #2 stabilizes at a value of approximately 10 mm^2 and remains constant at that value for over 100 seconds (from about 450 seconds to 560 seconds). The subsequent behavior of the drum and the resulting breach area is driven almost exclusively by the dynamic response of the lid resulting from the depressurization event. Unfortunately, because a significant amount of mass scaling has been employed to allow a reasonably large time-step to be used with the explicit solver, the dynamic response of the lid cannot be trusted (the lid essentially respond dynamically as if it was very massive), and therefore, the calculated breach area much past about 550 seconds, where the lid response clearly dominates the breach area, is not reliable.

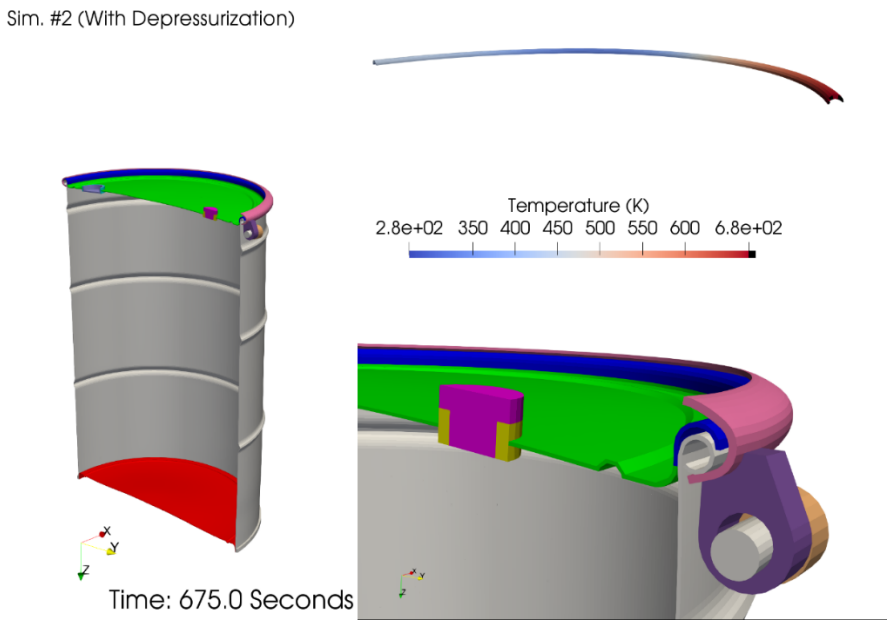

a) 675 Seconds – Time at Which the Closure Ring Failed in Sim. #1 (Compare Figure 4-10a)

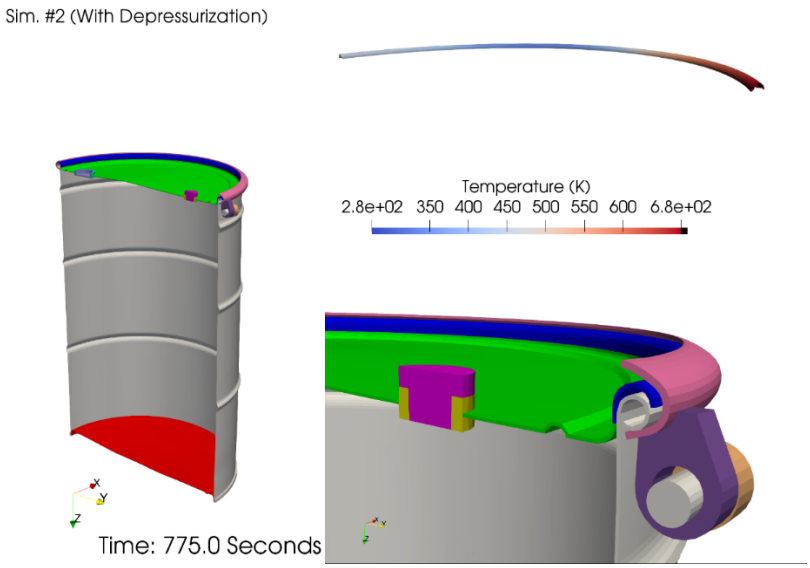

b) 775 Seconds – Time at Which the Lid Was Clearly Seen to be Flying Free in Sim. #1 (Compare Figure 4-10b)

Figure 4-14 Simulation 2: Lid Retained Following Drum Depressurization.

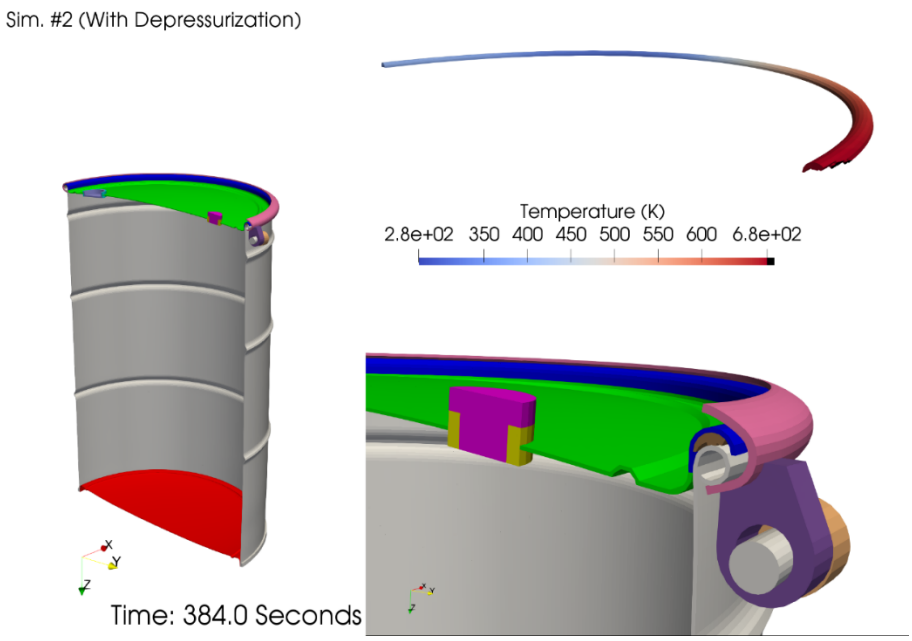

a) 384 Seconds – Beginning of Drum Depressurization (Compare Figure 4-11b)

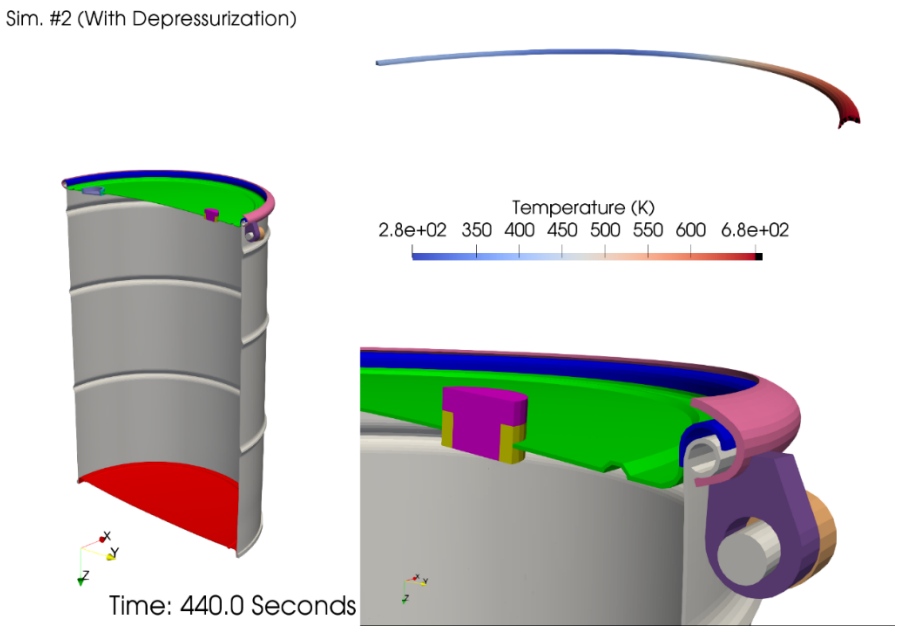

b) 440 Seconds – Drum Fully Depressurized

Figure 4-15 Simulation 2: Depressurization of Drum.

4.5. Drum Thermal Fluid Model: CFD and Release

SIERRA/TF was utilized to determine the release fraction of contaminant through the predicted ventilation paths as the drum undergoes a fire environment. Due to time constraints and the comparatively small (1×10^{-5} m^2) predicted ventilation area to the drum surface area, only a preliminary simulation was completed. The preliminary simulation utilized a significantly larger ventilation area (2×10^{-3} m^2) based on early Thermal Mechanical predictions. The initialization time of 507 seconds originates from the same predictions. The final release predictions presented here are results from the preliminary simulation, as time did not permit the simulation to be rerun with the corrected ventilation area and corresponding time (450 seconds).

4.1.7. Model Description

4.1.7.1. Model Input Parameters

The release model utilized several parameters from the previous two simulations as input parameters. The predicted material decomposition rate from Aria of 0.0023 kg/s was used to determine that 1.17 kilograms of trash had converted to gas at the time of first breach (508 seconds). The Mishima and Schwendiman RART tests [Mishima 1973] provided an initial, average mass loading of 0.97% contaminant compared to the total mass. This loading was multiplied by the mass loss at the time of breach to estimate a predicted mass for the entrained contaminant (11.4 g).

4.1.7.2. Computational Mesh

The TF/CFD mesh was greatly simplified from the TF/HT and SM/TM meshes. Figure 4-16 and Figure 4-17 illustrate the mesh used; shown is half of the domain. The mesh was comprised of 692,064 hexahedral elements. The element volume ranged from $3.06\text{x}10^{-6}$ to $1.09\text{x}10^{-4}$ m^3, with an average size of $2.39\text{x}10^{-5}$ m^3. The mesh had an average aspect ratio of 2.8, with a maximum of 11.3. The average skew was 0.032, with a maximum skew of 0.36. Unfortunately, time did not permit a full analysis with the calculated vent area from the second thermal-mechanical simulation, as seen in Figure 4-15. To demonstrate the release physics, a vent area of $2\text{x}10^{-3}$ m^2 was chosen which provided stable calculations, calculated before the release area was calculated by Presto. Likewise, the start time of 507 seconds stemmed from a preliminary Presto simulation.

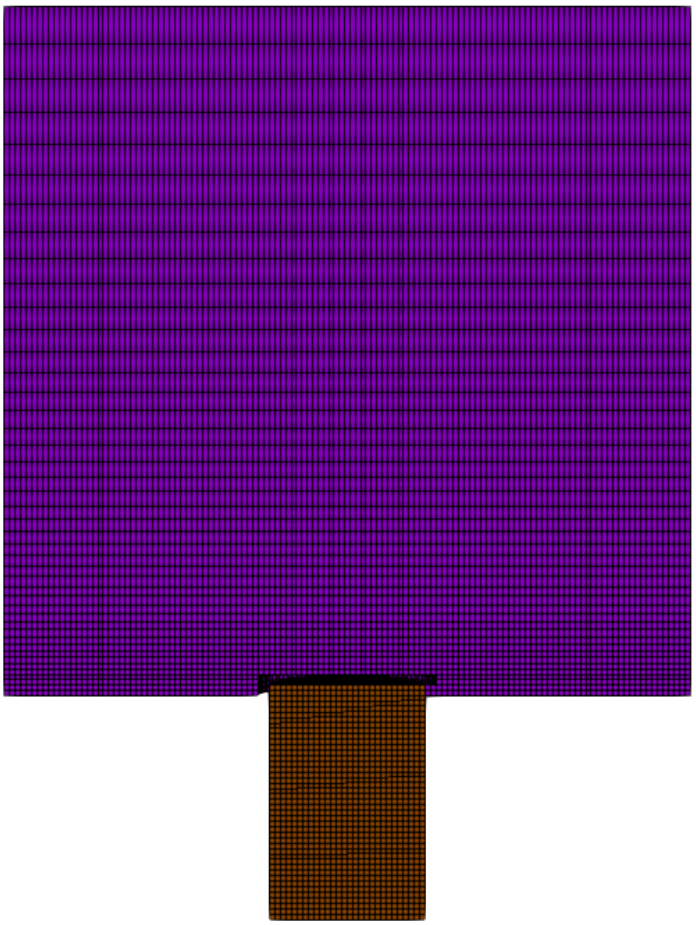

Figure 4-16. Thermal Fluids CFD Mesh (Half Domain)

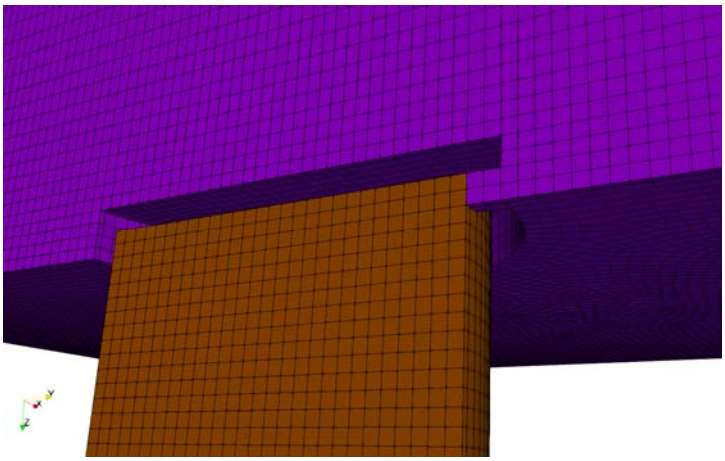

Figure 4-17. CFD Mesh Vent Release Area (Half Domain)

4.1.7.3. Boundary and Initial Conditions

The TF/CFD simulation utilized the inner surface temperature values from the Aria predictions as a boundary condition. The simulation starts at the 507 second mark compared to the Aria simulation, starting after the internal pressure equilibrates in order to encompass the release without using excess computational time. The initial temperature of the air (478 K) was taken from the average air region temperature in Aria at 507 seconds. The orange surface in Figure 4-18 was modeled as an open boundary condition, while the drum (green surface) was represented by a wall boundary condition, where the temperature was mapped from the internal surface of the Aria drum results. The blue surfaces were also modeled as wall boundaries to increase the solution stability. The initial pressure of the drum was taken to be atmospheric, as the drum would equilibrate after the initial rupture.

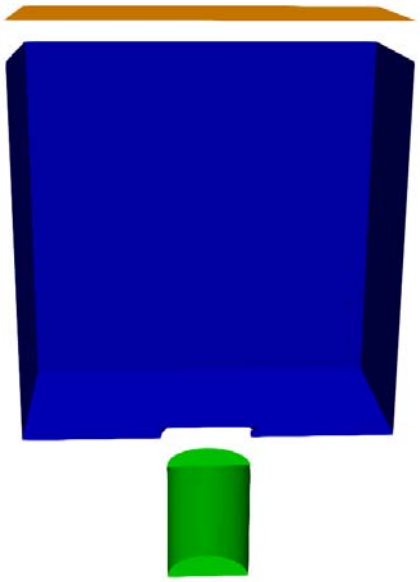

Figure 4-18 CFD Mesh Boundaries (Exploded View for Clarity).

4.1.7.4. Particle Release

In order to model contaminant release, particles must include in the simulation. To do that, entrainment mechanisms must be accounted when the trash is being decomposed, the ability for the contaminant can be entrained. In this section, the entrainment mechanisms will be described, followed by the particle injection method used in the simulation.

4.1.7.4.1. Entrainment Mechanisms

A search of the literature did not reveal an entrainment mechanism directly related to this scenario. It is believed that contaminant particles are entrained by either resting on flakes of char lofted from the trash bulk due to the convective flows or solely the contaminant particle can be entrained by shear flow resuspension. The resuspension method has been discussed at length in previous work [Zepper 2017]. A capability to model the 'char' entrainment mechanism was being incorporated

to the CFD code Fuego while this study was occurring, but was not available for use in the simulations presented here [Koo 2017].

4.1.7.4.2. Particle Injection Method

In order to model contaminant release, particles sized similar to the contaminant used in the RART experimental study were injected into the fluid mesh, starting at 507 seconds, which coincides with the opening of the vent path in the SM simulation. The contaminant was represented by Lagrangian particles coupled to the Eulerian flow. The density of the particles was set to 10970 kg/m^3, the density of uranium dioxide. A size distribution comparison between the experimental particle distribution used by Mishima and Schwendiman and that used in the simulation is shown below in Figure 4-19. Particle parcels are used to represent a grouping of particles. The $5.3x10^{10}$ contaminant particles injected into the code were represented by 839 parcels, injected randomly throughout the drum volume. Parcels were injected into the volume at the onset of the simulation through an input data file. The details of parceling in the TF/CFD code have been previously reported by Brown et al. [2015, 2016]. All surfaces were assumed to be 'stick' boundaries which collect parcels as they collide with that boundary. Total deposited mass and total number of particles were recorded on the boundary nodes. It is acknowledged that the decomposing trash block would interfere with the internal flows and particle transport. A method to model solidus trash using particles is under development, but was not available at the time of this study [Koo 2017].

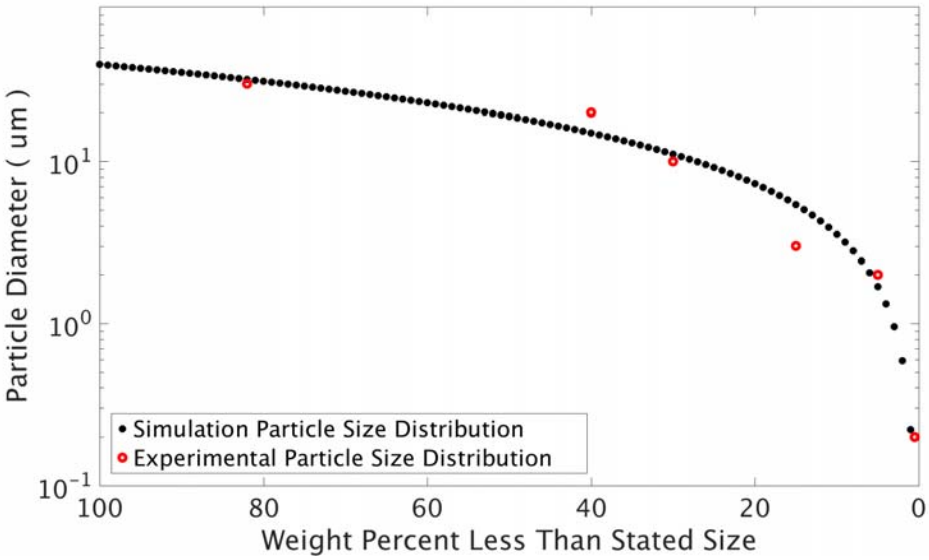

Figure 4-19. Contaminant Input Size Distribution. Red Circles: Experimental Size Distribution from RART, Black Line: Simulation Input Size Distribution

4.1.8. Results

Due to time constraints and limited resources, a detailed study of simulating the release using Fuego could not be performed. An analysis using a choked flow assumption showed that, for the peak vent area observed in the Presto results ($1x10^{-5}$ m^2) and the internal drum pressures from the Aria results (275 kPa), the flow exiting through the breach exceeded the low Mach assumption

Fuego (< 0.3Ma). An effort was made to simulate the release after the high-pressure had vented, as the convective flows inside the drum have the potential to loft particles.

The simulation shows some contaminant does release from the drum vented opening (see Figure 4-20). The initial contaminant release is shown in Figure 4-20a. The particles in the drum interior are experiencing counter-clockwise vortex flow as the heated (right) edge drives the particles upwards towards the vent. The majority of the mass deposits onto the drum walls, as seen in Figure 4-20b.

An evaluation of the ARF from the sole CFD simulation was performed. It is emphasized that, while this demonstrates the unique coupling capability provided by the SIERRA suite of simulation tools, the values reported do not represent a full parametric analysis of the release. Table 4-4 lists the mass end states for the contaminant. An original contaminant mass of 300 grams suspended in the trash was chosen to represent the Material at Risk (MAR), using the same contaminant-to-trash loading ratio used by Mishima and Schwendiman. Particles were assumed to be entrained into the drum volume as the trash decomposed, and as such, only a small fraction (11.3 grams) were suspended at the vent time.

The majority of the contaminant was predicted to deposit back onto the drum surface. The contaminant released through the vent represents the ARF multiplied by the DR, found to be 0.02% for the described scenario. A hesitant comparison to the values determined in [Mishima 1973] shows agreement with the average ARF (0.019%) from the experiments looking at solid contaminants, however, it should be noted that the scenarios are markedly different. As mentioned previously, the predicted ARF should not be taken as a final value, as a complete sensitivity study was not performed. All of the released parcels were below 10 microns, resulting in an RF of 1.0.

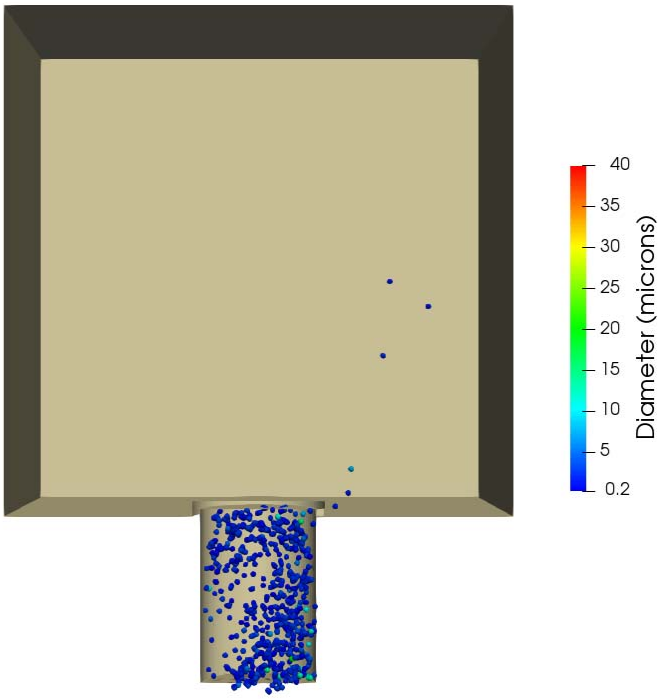

Time: 510.00 sec

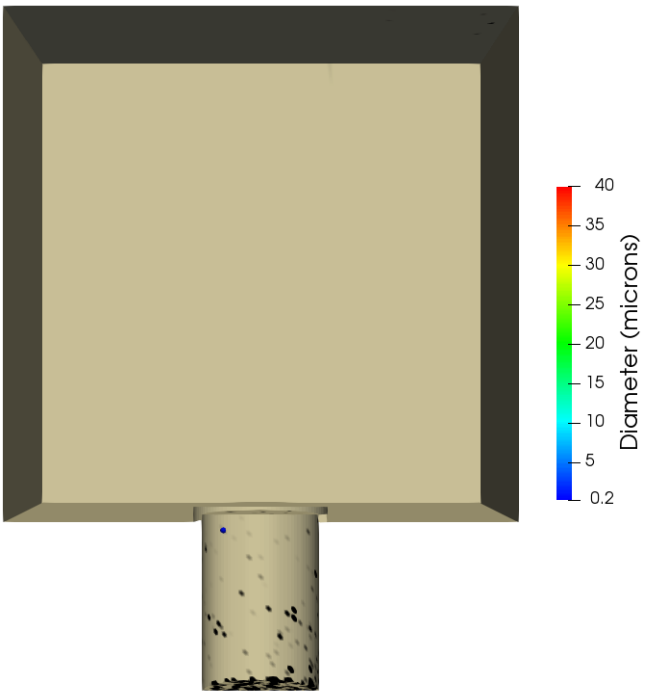

Time: 600.00 sec

Figure 4-20. a) Particle Release from Vented 7A Drum and b) Mass Deposition Location

Table 4-4. Predicted Mass Deposition Location and ARF from TF/CFD Simulation

Parcel Deposition Location	Mass Deposition (kg)	Mass Fraction (%)
Drum Walls	0.0113	99.49%
Released (DR×ARF)	5.85×10^{-5}	0.02%

4.6. Summary and Conclusion

Multiple physics codes within the SIERRA framework (e.g., Aria, Presto, and Fuego) were used in a coupled manner to simulate a contaminant release from a 55-gallon drum adjacent to a three-meter pool fire. The intent of this work was to demonstrate the ability of the SIERRA codes to simulate these types of accident scenarios and to provide useful information about hazardous material release. The simulation was loosely based on a drum fire experiment performed in SNL's FLAME facility.

Aria was used to solve the heat transfer, internal material decomposition, and pressurization of the drum subjected to a heat flux boundary condition. Temperature and pressure data from the Aria simulation was used to solve for the thermal/mechanical response of the drum, including decomposition and failure of the seal, using Presto. Breach areas determined from the Presto simulations were used to calculate the internal fluid response, contaminant entrainment, and release, using Fuego. For the selected scenario, a DRxARF=0.02% was calculated. However, it should be emphasized that, due to time constraints, the DRxARF value was determined using a preliminary ventilation area, not the final predicted area from Presto.

The successful use of the SIERRA codes to calculate a DRxARF clearly demonstrates the ability of the SIERRA codes to simulate these types of accident scenarios and to provide useful information about hazardous material release. The process also identified several limitations of the codes and approach taken. Targeted model improvements to address these limitations include:

- Time constraints necessitated that the explicit solver within Presto be used, and that mass scaling be employed. To improve the accuracy of the predicted dynamic behavior of the drum following depressurization, an implicit transient dynamic solution strategy should be employed.

- To more accurately predict the ejection of particles during the relatively quick depressurization of the drum through the relatively small opening, a high Mach CFD code should be used.

- A Sierra/Fuego capability to better model the contaminant released from decomposing materials. The capability was undergoing verification at the time of this study.

- Given more time, a revised CFD simulation with a more representative ventilation area could have been performed to model the contaminant release more accurately.

5. Summary and Conclusion

This report summarizes the accomplishments made in the first two years of the project as well efforts and results made during the third year. In the third year of the project, we improved existing computational capabilities to better model fragmentation situations to capture small fragments during an impact accident and fire releases. In addition, we revised Chapter 6 of the Handbook to document recent literatures and provided an estimate of the ARF and RF for the inadvertent nuclear criticality. Finally, we simulated a postulated drum failure during a fire accident. The summary and conclusion of each of the three tasks are described below.

Fragmentation Model Development (Task 1)

For task 1, we developed the capability of SIERRA/SM code to model the fragmentation experiment of a fracture of a UO_2 pellet using an improved two-scale model approach from that described in Year 2 (previously referred as a sequentially-applied fragmentation model) and for the Pyrex experiments described in the Handbook.

In FY17, as described in Chapter 2 of this report, we developed two new modeling and analysis capabilities that will lead to better predictions of airborne particle releases during impact or free-fall of ceramic fuel forms. These new capabilities enable the characterization of the final state of fragmentation (in terms of size and distribution of fragments) as a function of the materials properties, the energetic loading conditions and the intrinsic length scale associated with fragmentation (through scale separation with both the macro- and micro-scale models). These models were used to predict the fragments in the range of 10 microns or less, that result from impact loading of a brittle material as reported in [Louie 2016] which in that case was a ceramic cylinder of commercial UO_2 nuclear fuel.

The two new models are described, compared with each other, and were validated using the Handbook data on fragmentation (for lower impact energies) and German tests conducted on spent fuel (for higher impact energies).

The validation results of the sequentially-coupled fragmentation model against the Handbook impact tests on unirradiated UO2 show that the model bounds the experimental particle size distribution model relatively well. This indicates that the modeling efforts are correctly capturing the fragmentation's physical phenomena. However, the discrepancy observed at lower length scales points to certain limitations in the current state of the model. Notably, the sensitivity of the fragment size distribution on the strain-rate boundary conditions in the microscale model necessitate a more careful handling of the two-way coupling between both scales. Additionally, the disagreement between the experimental fragmentation characterization and modeling prediction for Pyrex points to the fact that the inherent strain-rate dependence of various materials' properties used in the model is warranted for predictability over a wide of material systems. The newly developed and implemented concurrently-coupled model allows for the continuous update of the microscale fragmentation model boundary conditions such as strain-rate. This change is intended to allow the microscale fragmentation model to better reproduce the experimentally observed distribution of fragment sizes. However, the concurrently-coupled model is presently not reproducing experimental results, but a clear path forward is outlined in order to remedy the situation in the coming year with proposed solutions as described in Chapter 6.

For this task, we completed the following:

1. Implementation of the prior-year sequentially-coupled fragmentation model as a LAME material model within SIERRA/SM entitled MicroFragmentation_Sequential.
2. Validation of the results of the sequentially-coupled model against the prior-year sequentially-applied model to show consistent behavior of the model.
3. Comparison of the results of the sequentially-coupled model to two sets of experiments conducted by different entities on unirradiated UO_2 fuel and pyrex borosilicate glass.
4. Discussion of the weaknesses of the sequentially-coupled model and the aspects of a new model that are needed to overcome the limitations of the model.
5. Development and implementation of a new concurrently-coupled fragmentation model within LAME entitled MicroFragmentation_Concurrent.
6. Identification of the limitations of the concurrently-coupled model and outlined pathways to remediate the model.

Revision of Chapter 6 of Handbook (Task 2)

Chapter 6 of the Handbook "Inadvertent Nuclear Criticality" was updated as described in Chapter 4 of this report. The original Chapter 6 of the Handbook was enhanced, which included updating the historical excursion (criticality) accidents with more recent criticality accidents (e.g., Tokaimura accident in Japan) and new information. The discussion of the various types of criticality accidents was updated, including the fission yield models and historical yields.

To accommodate the analyses of all reported process criticality accidents, the accident description was also revised. The accidents are now divided into 3 types: single spike, multiple excursions over a 10-minute period, and a slow cooker delayed supercritical system over 8 hours. Each of these was analyzed with the SCALE package using the TRITON-Depletion sequence to determine the activities of specific radionuclides at the end of the excursion and at various times after the shutdown of the excursion. For an excursion involving reprocessing solutions, ORIGEN-ARP runs were made to determine the actinide and fission product activities of such a solution. Then an excursion in this solution was modeled. It was determined that the addition of initial actinide content had negligible effect on the resulting activities.

A review of excursions other than those in solution systems indicated that assumptions in the previous version of the Handbook were overly conservative. The accident scenarios and releases were updated using the information from the excursions,. The number of the fission yield tables in Chapter 6 of the Handbook have been updated (using more recent literature information and source term analyses) or deleted.

We reviewed the analytical models for fission yield in solution criticalities and selected [Barbry 1987, Tuck 1974] as the two that best fit the existing data from solution criticality excursions.

A review of work done on release fractions (RF) on spent fuel pool accidents under contract with the NRC [NUREG 1987 and NUREG 1997], indicates that these RF values are conservative and applicable to criticality accidents. These RF values are less conservative than those identified by [Restrepo 1992] in Table 6-10 of the previous edition of the Handbook. However, after a review of the NUREG reports and what is likely to occur during criticality accidents (based on past

accidents), these RF values are expected to be more realistic. These values are included as Table 3-15 replacing Table 6-10 of the Handbook.

Drum Fire Release Simulation (Task 3)

Finally, as part of this third-year efforts as shown in Chapter 3 of this report, we simulated a breach and combustion scenario involving the contents of a 7A (55-gallon) waste drum. No such data existed previously. The review was prompted by a recent drum accident at the Waste Isolation Pilot Plant. The drum fire release simulation used the existing drum model from the WIPP study and recent pipe over pack fire experiments conducted at SNL. SIERRA/FM and SM codes (Aria, Fuego and Presto) simulated in real-time the coupling of the heat transfer, solid mechanics, and fluid dynamics to predict DR, ARF and RF.

Aria, Presto, and Fuego were coupled to simulate the contaminant release from a 55-gallon drum adjacent to a three-meter pool fire. Our intent was to demonstrate the ability of the SIERRA codes to simulate these types of accident scenarios and to provide useful information about hazardous material release. The simulation was loosely based on a drum fire experiment performed in SNL's FLAME facility.

Aria was used to solve the heat transfer, internal material decomposition, and pressurization of the drum subjected to a heat flux boundary condition. Temperature and pressure data from the Aria simulation was used to solve for the thermal/mechanical response of the drum, including decomposition and failure of the seal, using Presto. Breach areas determined from the Presto simulations were used to calculate the internal fluid response, contaminant entrainment, and release, using Fuego. For the selected scenario, a DRxARF=0.02% was calculated.

The SIERRA codes successfully calculated a DRxARF, demonstrating the ability of the SIERRA codes to simulate these types of accident scenarios and to provide useful information about hazardous material release. However, several limitations of the codes and approach were identified. Targeted model improvements to address these limitations include:

- Time constraints necessitated that the explicit solver within Presto be used, and that mass scaling be employed. To improve the accuracy of the predicted dynamic behavior of the drum following depressurization, an implicit transient dynamic solution strategy should be employed.
- To more accurately predict the ejection of particles during the relatively quick depressurization of the drum through the relatively small opening, a high Mach CFD code should be used.
- One identified model improvement was undergoing verification at the time of this study: A capability in Sierra/Fuego to better model the contaminant released from decomposing materials.
- Given more time, a simulation with a more representative vented area could have been performed to model the contaminant release more accurately.

6. Recommendation for Future Works

Based on the tasks we completed this year, we recommend the following:

From the fragmentation modeling as described in Chapter 2, the following model improvement are recommended:

- Improve the phase field formulation for consistency between both scales to better account for energy dissipation due to the opening of cohesive zones in the microscale mode.
- Use a different formulation of the damage function (presently c^2) that will better reproduce linear elastic behavior before fracture.
- Implement the micromorphic microscale model presented in Section 2.4.3.3 within both the concurrently- and sequentially-coupled models.
- The developments of the concurrently-coupled model listed above will be the focus of FY18 efforts in order to accurately reproduce the available experimental results and enable predictive capabilities to predict airborne releases for in circumstances not representative of existing experiments.

From the drum fire simulation as described in Chapter 4, the following model improvements should or could be made:

- An implicit dynamic (instead of the mass scaled explicit dynamic) simulation could be performed to more accurately capture the true dynamic behavior of the drum following depressurization.
- A high Mach CFD code could be employed in future work to properly simulate the release of particles in the high pressure environment.
- Include the new capability being implementing into Sierra/Fuego to better model contaminant released from decomposing materials, which was undergoing verification at the time of this study.
- Perform a simulation with a more representative vented area to model the contaminant release more accurately.

In the coming year, we will:

1. Simulate a free-fall spill and impact stress on two containers to investigate the possible releases in terms of DR, ARF and RF for 7A drums (55 gallons) and other containers.
2. Revise Equation 4-1 of the Handbook based on the work accomplished in FY17 regarding fragmentation code development and validation. Based on the recommendation above, the fragmentation model development should be improved before this revision is done.

In the first task, we will review and revise the free-fall spill and impact stress sections in Chapter 4 and Chapter 5 of the Handbook, since these accidents are associated with human errors with an annual frequency of between 10^{-2} to 10^{-1} and may result in significant dose to workers. For these chapters, we propose to examine the DR. In the Handbook, the concept of DR is discussed with respect to the determination of the source term in the five-factor formula. DR has the potential to significantly affect the source term to workers that must be considered in the safety evaluation for a particular accident and facility. While values for DR are provided for a few of the scenarios discussed in the Handbook, in particular criticality accidents, no guidance is provided on damage ratios for the majority of the scenarios, including the free fall spill and impaction stress accidents. These types of accidents typically occur where the material of interest is contained in some sort of packaging, such as a metallic can or drum container. Extensive testing of hazardous materials transportation packages performed at SNL, in conjunction with a wide range of associated analyses, has demonstrated that packaging for these materials, if properly designed, can be robust, limiting the release of hazardous materials even in severe beyond-design basis accident conditions [10,11]. The intent here is to cover a range of conditions that are reasonable that can happen across the DOE complex to estimate the DR. Once this DR value is non-zero, then the consideration of the ARF and RF from the Handbook can be applied.

In the second task, we will revise Equation 4-1 in the Handbook to expand this equation to include a number of micromorphic phenomena. The source term ARF×RF for environmental release from the fragmentation of glass and oxide ceramic radioactive materials forms is quantified through Equation 4-1 in the Handbook which is a simple empirical correlation accounting for fall height (rate effects) and specimen density. However, the fragmentation behavior of such brittle materials is also dependent on other factors such as temperature and material structural variables such as grain size and porosity. While the empirical bounding values obtained through this correlation are very conservative and prove satisfactory to comply with the regulatory process for handling and transporting these materials, they are based on test data for only a few materials subjected to a limited range of loading conditions. Because the final state of fragmentation (in terms of the size and distribution of fragments) is strongly dependent not only on the density of the material and the energetic loading conditions that lead to breakup (which are accounted for in Eq. 4-1), but also on the operating temperature and many length scales (porosity, grain size) associated with the material, it is difficult to precisely predict fragmentation characteristics for other brittle solid wastes forms subjected to a wider range of loading conditions based on the available test data alone. We propose to revisit Eq. 4-1 of Section 4.3.3 of the Handbook to include a dependence on both the temperature and porosity characteristics (volume fraction, characteristic size of pores) by exercising a two-scale fragmentation model developed in the SIERRA SM model.

7. References

[ANS-8.23 2007] **American National Standard – Nuclear Criticality Accident Emergency Planning and Response,** ANSI/ANS-8.23-2007 (R2012), American Nuclear Society, La Grange Park, IL.

[ANSI MH2 1991] ANSI MH2-1991, "American National Standard for Materials Handling (Containers) – Steel Drums and Pails," American National Standards Institute (ANSI), New York, NY, 1991.

[ASTMa 2014] ASTM A1056 – 14, "Standard Specification for Flexible Cellular Materials – Sponge or Expanded Rubber," American Society of Testing and Materials, ASTM International, West Conshohocken, PA, 2014.

[ASTMb 2014] ASTM A307 – 14, "Standard Specification for Carbon Steel Bolts, Studs, and Threaded Rod 60000 psi Tensile Strength," American Society of Testing and Materials, ASTM International, West Conshohocken, PA, 2014.

[ASTM 2015] ASME BPVC, "ASME Boiler and Pressure Vessel Code," American Society of Mechanical Engineers, New York, NY, 2015.

[ASTM 2016] ASTM A1008/A1008M – 16, "Standard Specification for Steel, Sheet, Coled-Rolled, Carbon, Structural, High-Strength Low-Alloy, High-Strength Low-Alloy with Improved Formability, Solution Hardened, and Bake Hardenable," American Society of Testing and Materials, ASTM International, West Conshohocken, PA, 2016.

[Barbry 1987] Barbry, F. , "Model to Estimate the Maximum Fission Yield in Accidental Solution Excursions," Transactions of the American Nuclear Society, San Francisco, CA, Vol. 55, pg. 142, November 1987.

[Barbry 1993] Barbry, F, "Review of the SILENE Criticality Excursions Experiments," Rapport SRSC 93 (220), IPSN, Commissariat à l'Energie Atomique, December 1993.

[Barbry 2009] Barbry, F, Fouillaud, P., Grivot, P. and Reverdy, L.,"Review of the CRAC and SILENE Criticality Accident Studies." Nuclear Science and Engineering, Vol 161, No. 2, pp 160-187, 2009.

[Batdorf 1978] Batdorf, S. B. and H. L. Heinisch, "Fracture statistics of brittle materials with surface cracks." Engineering Fracture Mechanics 10: 831-841, 1978.

[Bergman 2011] Bergman, T. L., Lavine, A. S., Incropera, F. P., Dewitt, D. P., Fundamentals of Heat and Mass Transfer. 7th ed., John Wiley & Sons, 2011.

[Borden 2012] Borden, M. J., C. V. Verhoosel, M. A. Scott, T. J. R. Hughes and C. M. Landis, "A phase-field description of dynamic brittle fracture." Computer Methods in Applied Mechanics and Engineering 217-220: 77-95, 2012.

[Diebold 1994] Diebold, J. P., "A Unified, Global Model for the Pyrolysis of Cellulose," Biomass and Bioenergy, Vol. 7, Nos. 1-6, pp. 75-85, 1994.

[Dingreville 2014] Dingreville, R., Robbins, J. and Voth, T.E., "Wave Propagation and Dispersion in Elasto-Plastic Microstructured Materials," International Journal of Solids and Structures, 51(11), page 2226-2237. 2014.

[DOE 1994] U.S. Department of Energy, **Airborne Release Fractions/Rates and Respirable Fractions for Nonreactor Nuclear Facilities,** DOE-HDBK-3010, December 1994.

[DOE 2007] DOE, **Guidelines for Preparing Criticality Safety Evaluations at Department of Energy Nonreactor Nuclear Facilities,** DOE-STD-3007-2007, U.S. Department of Energy, Washington, DC, February 2007.

[DOE 2014] DOE**, Preparation Guide for U.S. Department of Energy Nonreactor Nuclear Facility Safety Analysis Reports,** DOE-STD-3009-2014, U.S. Department of Energy, Washington, DC, November 2014.

[Forest 2006] Forest, S., and Sievert, R., "Nonlinear Microstrain Theories," International Journal of Solids and Structures, 43(24), page 7224-7245, 2006.

[Figueroa 2017] Figueroa, V.G., et al, Pipe Overpack Container Fire Testing: Phase I & II, SAND2017-5684, Sandia National Laboratories, Albuquerque, NM, May 2017.

[ISO 2011] ISO, **Nuclear Criticality Safety – Estimation of the Number of Fissions of a Postulated Criticality Accident,** International Organization for Standardization, ISO/CD 16117, 2011.

[Jardine 1982] Jardine, L. J., W. J. Mecham, G. T. Reedy and M. J. Steindler, **Final Report of Experimental Laboratory-Scale Brittle Fracture Studies of Glasses and Ceramics,** Argonne National Laboratory, 1982.

[Lewellen 1976] Lewellen, P. C., Peters, W. A., Howard, J. B., "Cellulose Pyrolysis Kinetics and Char Formation Mechanism," Fire and Explosion Research, 1976.

[Linger 1968] Linger, K. R. and D. G. Holloway, "The fracture energy of glass." Philosophical Magazine 18: 1269-1280, 1968.

[Lorentz 2011] Lorentz, E., S. Cuvilliez and K. Kazymyrenko, "Convergence of a gradient damage model toward a cohesive zone model." Comptes Rendus Mecanique 339(1): 20-26, 2011.

[Lorentz 2012] Lorentz, E., S. Cuvilliez and K. Kazymyrenko, "Modelling large crack propagation: From gradient damage to cohesive zone models." International Journal of Fracture 178: 85-95, 2012.

[Louie 2015] Louie, D.L.Y. and Brown, A. **NSRD-6: Computational Capability to Substantiate DOE-HDBK-3010 Data,** SAND2015-10496, Sandia National Laboratories, Albuquerque, NM, November 2015.

[Louie 2016] Louie, D.L.Y., et.al, **NSRD-11: Computational Capability to Substantiate DOE-HDBK-3010 Data,** SAND2016-12167, Sandia National Laboratories, Albuquerque, NM, November 2016.

[Kumar 2013] Kumar, S. and Singh, R.K., "Thermolysis of High-Density Polyethylene to Petroleum Products," Journal of Petroleum Engineering, Vol 2013, Article ID 987568, DOI:10.1155/2013/987568, 7 pages, 2013.

[McLaughlin 1991] McLaughlin, T.P., **Process Criticality Accident Likelihood, Consequences, and Emergency Planning,** LA-UR-91-2325, Los Alamos National Laboratory, Los Alamos, NM, 1991.

[McLaughlin 2000] McLaughlin, T.P, Monahan, S.P., Pruvost, N.L., Frolov, V.V., Ryazanov, B.G., and Sviridov, V.I., **A Review of Criticality Accidents,** LA-13638, 2000 Revision, Los Alamos National Laboratory, Los Alamos, NM, 2000.

[McLaughlin 2003] McLaughlin, T.P., "Process Criticality Accident Likelihoods, Magnitudes and Emergency Planning – A Focus on Solution Accidents," Proceedings 7th International Conference on Nuclear Criticality Safety (ICNC 2003)

Tokaimura, Ibaraki, Japan, Oct. 20-24, 2003 JAERI Conf 2003-019, pp 831-836, 2003.

[Mecham 1981] Mecham, W. J., L. J. Jardine, R. H. Pelto, G. T. Reedy and M. J. Steindler, **Interim Report of Brittle-Fracture Impact Studies: Development of Methodology,** Argonne National Laboratory, 1981.

[Minana 2012] Minana, M., Turgeon, J., Lujan, C., Pilch, M., and Hackney, P., **Sandia National Laboratories Advanced Simulation and Computing (ASC) Software Quality Plan – ASC Software Quality Engineering Practices, Version 3.1,** SAND2008-5517, Sandia National Laboratories, Albuquerque, NM, March 2012.

[Mishima 1973] Mishima, J., and Schwendiman, L. C., "Fractional Airborne Release of Uranium (Representing Plutonium) During the Burning of Contaminated Wastes," BNWL-1730, April 1973.

[Nakajima 2003] Nakajima, K., "Applicability of Simplified Methods to Evaluate Consequences of Criticality Accident Using Past Accident Data," Proceedings 7th International Conference on Nuclear Criticality Safety (ICNC 2003) Tokaimura, Ibaraki, Japan, Oct. 20-24, 2003 JAERI Conf 2003-019, pp 746-751, 2003.

[Nomura 1995] Nomura, Y. and Okuno, H., "Simplified Evaluation Models for Total Fission Number in a Criticality Accident," in Nuclear Technology, Vol. 109, pp. 142-152, January 1995.

[NUREG 1987] NUREG/CR-4982 **Severe Accidents in Spent Fuel Pools in Support of Generic Safety Issue 82,** Brookhaven National Laboratory, BNL-NUREG-52093, July 1987.

[NUREG 1997] NUREG/CR-6451, **A Safety and Regulatory Assessment of Generic BWR and PWR Permanently Shutdown Nuclear Power Plants ,** Brookhaven National Laboratory, BNL-NUREG-52498, August 1997.

[Nyer 1965] Nyer, N.E., Bright, G.O. and McWhorter, R.J. "Reactor Excursion Behavior" in Proceedings of the Third International Conference on the Peaceful Uses of Atomic Energy, Vol 13. Nuclear Safety, United Nations, New York, NY, 1965.

[Olsen 1974] Olsen, A.R., Hooper, R.L., Uotinen, V.O., and Brown, C.L., **Empirical Method for Estimating the Total Number of Fissions From Accidental Criticality in Uranium and Plutonium Systems,** BNWL-1840, Pacific Northwest Laboratory, Richland, Washington, July 1974.

[Rearden 2016] Rearden, B.T. and Jessee, M.A., Eds., SCALE Code System, ORNL/TM-2005/39, Version 6.2.1, Oak Ridge National Laboratory, Oak Ridge, Tennessee, 2016.

[Restrepo 1992] Restrepo, L.F., **The Annular Core Research Reactor (ACRR) Limiting Event for Workers and Public Consequences,** SAND91-0572, Sandia National Laboratory, Albuquerque, NM, August 1992.

[Ruhmann 1985] Ruhmann, H., A. Beleier, G. Kaspar, G. Hofmann, H. Löscher and M. Peehs, **Research Program on the Behaivor of Burn-up Fuel under Strong Mechanical Impacts,** Kraftwerk Union A.G.: 98, 1985.

[Scherzinger 2016] Scherzinger, W. M., B. T. Lester and P. Newell, **Library of Advanced Materials for Engineering (LAME) 4.42,** Sandia National Laboratories, 2016

[Selby 1975] Selby, J.M., et. al, **Considerations of the Assessment of the Consequences of Effluents from Mixed Oxide Fuel Fabrication Plants,** BNWL-1697, rev.1, Pacific Northwest Laboratories, Richland, Washington, June 1975.

[SIERRA 2016] Sierra Thermal Fluids Development Team, "Sierra Fuego User Manual – Version 4.40," Sandia National Laboratories, SAND 2016-4157, (2016).

[SIERRA 2017] http://compsim.sandia.gov/compsim/Docs/Sierra/4.44/GeneralRelease

[SIERRA 2017a] SNL, **SIERRA/Solid Mechanics 4.44 User's Guide,** SAND2017-4016, Sandia National Laboratories, Albuquerque, NM, April 18, 2017.

[SIERRA 2017b] SIERRA Solid Mechanics Team, **Sierra/Solid Mechanics 4.44, User's Guide: Addendum for Shock Capabilities,** SAND2017-4014, Sandia National Laboratories, Albuquerque, NM, April 18, 2017.

[SIERRA 2017c] Sierra Structural Dynamics Development Team, **Sierra/SD – Theory Manual,** SAND2017-3554, Sandia National Laboratories, Albuquerque, NM, April 6, 2017.

[SIERRA 2017d] Sierra Thermal/Fluid Development Team, **SIERRA Low Mach Module: Fuego User Manual – Version 4.44,** SAND2017-3792, Sandia National Laboratories, Albuquerque, NM, April 13, 2017.

[Skinner 2017] Skinner, C.M., Evaluation of Energy Released from Nuclear Criticality Excursions in Process Solutions, M.S. Thesis, University of New Mexico, December 2017.

[Skolnik 2006] Skolnik Industries, Drawing CQ5508, Rev A5, "55 Gallon Open Head Drum, 1.5 – 1.5 – 1.5 CRCQ, 1A2/X430/S & 1A2/Y1.5/175," Skolnik Industries, Inc., Chicago, IL, November 7, 2006.

[Smith 1989] Smith, D.A. revision of Stratton 1967, **A Review of Criticality Accidents,** DOE/NCT-04, Nuclear Criticality Information System, US Department of Energy, Washington, D.C, March 1989.

[Stratton 1967] Stratton, W.F., **A Review of Criticality Accidents,** LA-3611, Los Alamos National Laboratory, Los Alamos, NM, September 1967.

[Strikwerda 2004] Strikwerda, J. C., Finite difference schemes and partial differential equations, SIAM. Team, S. S. M. Sierra/SolidMechanics 4.40 User's Guide, Sandia National Laboratories, 2016.

[Tuck 1974] Tuck, G., "Simplified Methods of Estimating the Results of Accidental Solution Excursions", Nuclear Technology, Vol. 23, pp 177-188, August 1974.

[USAEC 1975] WASH-1192, US AEC, **Operational Accidents and Radiation Exposure Experience with the USAEC,** WASH-1192, US Atomic Energy Commission, Washington, D.C, 1975.

[Wilson 2015] Wilson, David L., Baker, Michael L., Hart, Bradley R., Marra, John E., Schwantes, Jon ?M., and Shoemaker, Paul E., "Waste Isolation Pilot Plant Technical Assessment Team Report," SRNL-RP-2014-01198, Savannah River National Laboratory, Aikin, SC, March 17, 2015.

[Yang 2007] Yang, J. M., “Re-Evaluation of the 1995 Hanford Large Scale Drum Fire Test Results,” UCRL-TR-230686, Lawrence Livermore National Laboratory, Livermore, CA, May 3, 2007.

[Zepper 2017] Zepper, E. T., Brown, A. L., Pierce, F., Voskuilen, T., and Louie, D., “Contaminated Fuel Fires: Parametric Sensitivity of Resuspension and Boiling Particle Evolution,” TFEC-IWHT2017-17709, Proceedings of the 2nd Thermal and Fluid Engineering Conference, Las Vegas, NV, April 2-5, 2017.

[Zhou 2005] Zhou, F., J. F. Molinari and K. T. Ramesh, "A cohesive model based fragmentation analysis: Effects of strain rate and initial defects distribution." International Journal of Solids and Structures 42(18): 5181-5207, 2005.

[Zhou 2006] Zhou, F., J.-F. Molinari and K. T. Ramesh, "Effects of material properties on the fragmentation of brittle materials." International Journal of Fracture 139: 169-196, 2006.

Appendix A: Summary Table for Handbook Data

This appendix provides a summary table for the Handbook, including a number of columns: Column 1 identifies the chapter or section number; Column 2 identifies the category, such as liquid, solid, etc.; Columns 3 and 4 tabulate the bounding values; Column 5 describes any initial size distribution provided; and Column 6 provides comments. Note that Column 1 intends to provide the information of interests from those chapters/sections from the Handbook. It is not necessarily a complete list, since Chapter 2 of the Handbook deals with gaseous forms, which are often assumed to be released during an accident. Thus, it may not have an interest in this current research in terms of ARF and RF. Note: this summary table is an "in-progress" table, which means that it would be updated as more substantiating studies are done to the data in the Handbook.

Chapter /section	Category	ARF	RF	Initial Size Distribution	Comments*
3.0	***LIQUID***				This chapter divides into types of liquids, which includes aqueous solutions, organic, and combustible solvents.
3.2	*Aqueous solution*			Droplet distribution during bubbling is provided	This section describes models related to evaporation and boiling. Formulations on entrainment of liquid droplets from the surface of a bubbling or boiling pool are provided. Phenomena associated with these entrainments are described. (see Chapter 5 of NSRD-11 for more details about describing the use of these models in the simulations.)
3.2.1	Thermal Stress				
	(a) Heating of aqueous solution in flowing air without surface rupture bubbles	3.00E-05	1		
	(b) Boiling (bubbles continuously breaking the surface of the bulk liquid with < 30% of volume of the liquid as bubbles)	2.00E-03	1		
3.2.2	Explosion Stress				
	Venting of pressurized liquids				
	(a) Venting below liquid level	1.00E-04	1	< 10 µm	
	(b) Venting above liquid level				
	[1] low pressure (< 0.35 MPa)	5.00E-05	0.8		
	[2] high pressure (>0.35 MPa)				
	(aqueous solution)	2.00E-03	1		~1 g/cc solution density
	(conc. Heavy metal solution)	1.00E-03	0.4		≥1.2 g/cc solution density
	[3] superheated liquid				
	(≤ 50°C superheat)	1.00E-02	0.6		
	(50 to 100°C superheat)	1.00E-01	0.7		
	(> 100°C superheat)	$0.33*(MF)^{0.91}$	0.3		MF = mole fraction of pressurized gas/water vapor flashed
3.2.3	Free-Fall Spill				
	3-m distance				
	(a) aqueous solution				

Chapter /section	Category	ARF	RF	Initial Size Distribution	Comments*
	[1] aqueous solution	2.00E-04	0.5		~ 1g/cc solution density
	[2] conc. Heavy metal solution	2.00E-05	1		≥ 1.2 g/cc solution density
	(b)slurries < 40% solids	5.00E-05	0.8		
	(c) viscous solution, viscosity > 8 centipoise	7.00E-06	0.8		
	> 3-m				Both ARF and RF should be larger than the 3-m fall, and the empirical correlations for ARF and drop size presented in Ballinger et.al (Jan 1988)
3.2.4	Aerodynamic Entrainment and Resuspension				Use of these values for < 100 hours would not introduce serious error due to the severe depletion of the source.
	(a) indoor surfaces (SS, concrete) up to normal facility ventilation flow; outdoors, pool for low wind speeds	4.00E-07	1		
	(b)indoor, covered with debris or under static condition	4.00E-08	1		
	(c) outdoors, large pools wind speed ≤ 30 mph	4.00E-06	1		
	(d) outdoors, absorbed on soil, no lengthy pooling wind speed ≤ 50 mph	9.00E-05	1		
3.3	*Organic Combustible Liquids*				No experimental data on the behavior of organic, combustible liquids in response to explosive release, venting of pressurized liquid, free-fall spills or aerodynamic entrainment were found. We are examining some of the experiments referenced in this section for this year in the area of fire in Section 3.3.1 and Section 3.3.6 of the Handbook (see Chapter 4 of NSRD-6, Chapter 4 of NSRD-11)
	Thermal Stress				
	(a) volatiles (i.e., I2)	1	1		
	(b) Quiescent burning, small surface pool, or on larger pool	1.00E-02	1		
	(c) vigorous burning large pools	3.00E-02	1		This includes solvent layer burning over limited aqueous layer with sufficient turbulence to disrupt bulk of aqueous layer
	(d) Same as (C) to complete dryness	1.00E-01	1		
	(e) air-dried salts under gasoline fire	5.00E-03	1		Includes aqueous solution, on a porous or cracks, depression
	(f) same as (e) above, except on metal surface	2.00E-01	1		May not include porous, cracks or depression
4.0	***SOLIDS***				This chapter of the Handbook describes the data related to metals (primarily the release from energetic hydride reactions, nonmetallic

Chapter /section	Category	ARF	RF	Initial Size Distribution	Comments*
					(such as ceramics) or composite solids, and powders.
	Metal				
4.2.1	Thermal Stress				
	(a) Plutonium				
	[1] oxidation (corrosion) at room temperatures				These values intended for < 100 hours
	(unalloyed Pu)	$2x10^{-6}$ µg Pu/cm^2-hr (dry air)	0.7		
		$7x10^{-3}$ µg Pu/cm^2-hr (100% RH)	0.7		
	(delta-phase metal)	$7x10^{-8}$ µg Pu/cm^2-hr (dry air)	0.7		
		$6x10^{-4}$ µg Pu/cm2-hr (100% RH)	0.7		
	[2] oxidation at elevated temperatures	3.00E-05	0.04		
	[3] self-sustained oxidation	5.00E-04	0.5		Includes molten metal with oxide coat, self-induced convection
	[4]disturbed molten metal surfaces	1.00E-02	1		Such as flowing metal, actions resulting in continual surface renewal, high turbulence at surface. Impacted by high air velocity or free-fall, 95% confidence on these values. It is not applicable to oxidation of trace hydride, metal, powder contamination.
	[5] oxidation of small metal drops	1	0.5		hundreds of µm size, passing through air or explosive reaction of entire metal mass
	(b) Uranium				
	[1] complete oxidation of metal mass	1.00E-03	1		For thermal condition > 500 ^oC and for upward flow velocity of 0- 2 m/s. It is for airborne particles < 10 µm. A 95% confidence level is for flow velocities < 100 cm/s.
	[2] free-fall of molten metal drops	1.00E-02	1		This is based on an arbitrary increase of 95% confidence to the experiment data.
	[3] explosive dispersal of molten uranium	1	1		If the uranium is molten and subdivided in very small drops and ejected at sonic velocities (very fine particles and aggregates ≤10 µm)
4.2.2	Explosive Stress				No recommended value is given. It refers to the surface contamination section of the handbook. For shock effects, it refers to the size of the TNT equivalent for respirable release. 20% of the metal should be used as respirable fraction. Consult national laboratories for analyses.
4.2.3	Free-Fall and Impaction Stress				No significant release as indicated. Refer to the surface contamination section of the handbook. This section will be revised in the coming year.
4.2.4	Aerodynamic Entrainment and Resuspension				Identical correlations as described in the Thermal Stress type (a)[1] above.

Chapter /section	Category	ARF	RF	Initial Size Distribution	Comments*
4.3	*NONMETALLIC OR COMPOSITE SOLIDS*				
4.3.1	Thermal Stress				
	(a) vitrified waste				No significant release by industrial-type fire.
	(b) aggregate (e.g., concrete and cement)				
	[1] tritium release from concrete				
	(if present and 200 ^{o}C)	5.00E-01	1		
	(if present and 600 ^{o} C)	1	1		
	[2] suspendible powder	6.00E-03	0.01		
	[3] spent commercial nuclear fuel				These materials were discussed in general for accident conditions related to severe accidents in commercial reactors. Thus release related to thermal stress is related to the release described in Section 4.4.1 of the Handbook.
4.3.2	Explosive Stress				No recommended value is given. It refers to the surface contamination section of the handbook. For shock effects, it refers to the size of the TNT equivalent for respirable release. 20% of the metal should be used as respirable fraction. Consult national laboratories for analyses.
4.3.3	Free-Fall and Impaction Stress	see comment	see comment	A distribution related to the UO_2 pellet impacts is provided	A correlation for a combined value of ARF*RF is given as A*P*g*h, where A is an empirical correlation of 2E-11 cm^3 per g-cm^2/s^2, P specimen density, g/cm^3, g is gravity at sea level, and h is fall height in cm. (See Chapter 6 of NSRD-11 for the simulation and model approach to substantiate the impact data.) In the coming year, this equation would be revised to include the effect of micromorphic structures of the specimen.
4.3.4	Aerodynamic Entrainment and Resuspension				No significant release. See contamination section of this handbook.
4.4	*Powders*				For high energy stresses, the bounding values of 10 µm AED and RF =0.1 should be assumed. Note that no powder release due to impact of projectile was given. Exploratory simulation was done to an impact of can containing powder from a projectile (see Chapter 5 of NSRD-6).
4.4.1	Thermal Stress				Based on the thermal condition of < 1000 ^{o}C
	(a) non-reactive compounds	6.00E-03	1.00E-02		Entrainment of pre-formed particles by the flow upwards of heated surface.
	(b) reactive compounds except PuF_4	1.00E-02	1.00E-03		Particles formed by reaction given by the experiments
	(c) PuF_4	1.00E-03	1.00E-03		Particles formed by reaction given by the experiments
4.4.2	Explosive Stress				
	(a) shock effect				No data
	(b) blast effect				Detonations and deflagrations

Chapter /section	Category	ARF	RF	Initial Size Distribution	Comments*
	[1] above the surfaces	see comment	see comment		No detailed information is provided for detonation. For large deflagration, use ARF of 1 and RF for the original powder size that is < 10 µm. It is for a container failure pressure of ~ < 0.17 MPa.
	[2] accelerated airflow parallel to surface	5.00E-03	0.3		This represents a condition of the powders shield from the effects of a detonation or strong deflagration by standard containers.
	(c) venting of pressurized powders for deflagration > 25% confined volume				This also includes the condition of a deflagration and pressurized release. We are examining the pressurized release of powder experiment in this research (see Section 5.2 of [Louie 2015] and Section 5.2 of NSRD-11).
	[1] ≤ 0.17 MPa	5.00E-03	0.4		
	[2] 0.18 to 3.5 MPa	1.00E-01	0.7		
4.4.3	Free-Fall/Impaction Stress				We are examining a projectile hitting a can filled with powder (see Section 5.1 of [Louie 2015]). No applicable experiments are done or described. In the coming year, the simulations of the free-fall and impact stress simulations of the 7A drum and another container will be provided to estimate the DR, ARF and RF. This section will be revised in the coming year.
	(a) fall height < 3 m	2.00E-03	0.3		
	(b) fall height > 3 m	See comment. The calculated value must exceed those in (a)	See comment. The calculated value must exceed those in (a). The RF is limited in the total RF in the original powder.	see comment	Using PSPILL code to model powder spills - varying Mo (mass of powder spilled, kg). Air density and viscosity assumes to be 1.18 kg/m3 and 1.85e-5 Pa-sec, respectively. The correlation is given as: $ARF=2*0.1064*(M_o^{0.125})(H^{2.37})/\rho^{1.02}$, where H = spill height, and ρ = bulk density of powder. AMMD = 12.1-329*ρ+7530*F, where F is the airborne fraction (ARF). Note this equation only has a 46% correlation coefficient due to the variability in the data (see Section 5.1 of this report for the simulation).
	(c) suspended solid dispersed into flowing air	ARF = 0.0134 v_{wind}+0.00543, where v_{wind} is the wind speed (m/s)	The RF is limited in the total RF in the original powder.		For enhanced air velocities normal to direction of powder flow.
	(d) suspension of bulk powder in confinement	1.00E-03	0.1		Due to vibration of substrate from shock-impact to powder confinement (e.g., glovebox or can) due falling debris or external energy (i.e., seismic vibration)
	(e) suspension of bulk powder in debris impact and air turbulence from falling object	1.00E-02	0.2		No confinement is involved.
4.4.4	Aerodynamic entrainment and resuspension				Use of values given for short time frame (< 100 hours) (See Chapter 2 for modeling resuspension due to hum activity described in [Fish 1967].)

Chapter /section	Category	ARF	RF	Initial Size Distribution	Comments*
	(a) homogeneous bed of powder exposed to ambient condition	ARR = 4E-5/hr	1		Normal process facility ventilation flow, nominal atmospheric wind speed < 2 m/s, gusts up to 20 m/s, following the event.
	(b) homogenous bed of powder buried under structural debris exposed to ambient condition	ARR = 4E-6/hr	1		Including static conditions within structure following the event.
	(c) entrainment of powders from road surface by passage of vehicular traffic	1.00E-02	1		ARF is per passage
5.0	***SURFACE CONTAMINATION***				
5.2	*Contaminated, combustible solids*				
5.2.1	Thermal Stress				No applicable container release experiments due to thermal stress are documented. Mostly the burning of uncontained waste experiments are documented. Chapter 3 of this paper shows the simulation of the DR, ARF and RF of a ruptured drum due to thermal stress of a fire. This simulation is extrapolated from an existing drum fire experiment.
	(a) packaged mixed waste	8.00E-05	1		For contaminated combustible materials heated/burned in packages with largely non-contaminated surfaces
	(b) uncontained cellulosic or largely cellulosic mixed waste	1.00E-02	1		For burning of unpackaged, loosely strewn cellulosic materials
	(c) uncontained plastics				
	[1] except polystyrene	5.00E-02	1		
	[2] polystyrene	1.00E-02	1		
	(d) dispersed ash dropped into air stream or forced draft air				These values are not typically applied to burning mases of combustible material in large fires. These apply to extremely severe conditions where loosely contaminated combustible material is driven airborne as part of an updraft fireball.
	[1] loose powder	4.00E-01	1		
	[2] air-dried solution or adherent contamination	8.00E-02	1		
5.2.2	Explosive Stress				
	(a) shock effect				No data. Assume to be venting of pressurized gases over material.
	(b) blast effect				No data. Assume to be venting of pressurized gases over material.
	(c) venting of pressurized gases over contaminated combustible waste	1.00E-03	1		
5.2.3	Free-Fall and Impaction Stress				This section will be revised in the coming year.
	(a) materials with high surface area to mass ratios	0	0		No significant suspension is expected for freefall spill from working heights (~1 to 1.5 m)

Chapter /section	Category	ARF	RF	Initial Size Distribution	Comments*
	(b) combustible material is unpackaged/lightly packaged and strongly impacts the floor	1.00E-03	1		Or is impacted by falling debris. The values are based on reasoned judgment.
	(c) combustible material is packaged in a relatively robust container that is opened or fails due to impact with the floor or impaction by falling objects	1.00E-03	0.1		
5.2.4	Aerodynamic Entrainment and Resuspensions				Note that no applicable data found. Reasoned judgment is used. (For < 100 hours)
	(a) indoor or outdoor exposed to ambient conditions	ARR = 4E-5/hr	1		Normal process facility ventilation flow, nominal atmospheric wind speed < 2 m/s, gusts up to 20 m/s, following the event.
	(b) buried under debris exposed to ambient condition	ARR = 4E-6/hr	1		
5.3	*Contaminated, noncombustible materials*				
5.3.1	Thermal Stress	6.00E-03	0.01		Reasoned judgment applies
5.3.2	Explosive Stress				
	(a) shock effects				No recommended value is given. It refers to the surface contamination section of the handbook. For shock effects, it refers to the size of the TNT equivalent for respirable release.
	(b) blast effects				bounded by venting of pressurized gases in (c) below
	(c) venting of pressurized gases				These apply only to a loose surface contamination on the solid, not the solid as a whole. It includes corroded solids.
	[1] accelerated gas flows in area without significant pressurization	5.00E-03	0.3		
	[2] venting of pressurized volumes				
	(> 0.17 MPa)	5.00E-03	0.4		
	(< 0.17 MPa)	1.00E-01	0.7		
5.3.3	Free-Fall and Impaction Stress				This section will be revised in the coming year.
	(a) free-fall				Most materials will not experience free-fall spill. It is bounded by impact, shock vibration (b) below
	(b) impact, shock-vibration				
	[1] under brittle fracture	see comment	see comment		A correlation for a combined value of ARF*RF is given as A*P*g*h, where A is an empirical correlation of 2E-11 cm3 per g-cm2/s2, P specimen density, g/cm3, g is gravity at sea level, and h is fall height in cm.
	[2] materials that do not undergo brittle fracture	1.00E-03	1		
5.3.4	Aerodynamic Entrainment and Resuspensions				It is bounded by powders estimates
	(a) indoor or outdoor exposed to ambient conditions	ARR = 4E-5/hr	1		Normal process facility ventilation flow, nominal atmospheric wind speed < 2 m/s, gusts up to 20 m/s, following the event.
	(b) buried under debris exposed to ambient condition	ARR = 4E-6/hr	1		
5.4	*HEPA Filters*				

Chapter /section	Category	ARF	RF	Initial Size Distribution	Comments*
5.4.1	Thermal Stress	1.00E-04	1		Extrapolation of maximum experimental of release of particles accumulated by the passage heated air through HEPA filters
5.4.2	Explosive Stress				
	(a) shock effects	2.00E-05	1		Based on experimentally measured release of accumulated particles from HEPA filers, localized failure from a momentary high pressure pulse.
	(b) blast effects	1.00E-02	1		High velocity air flow through up to filter break pressure
	(c) venting of pressurized gases	1.00E-02	1		
5.4.3	Free-Fall and Impaction Stress				No applicable experimental data for airborne release during free-fall of HEPA filters were uncovered. This section will be revised in the coming year.
	(a) HEPA filter upon impact with hard unyielding surface				Bounded by conservative extrapolation of maximum releases measured for contained and uncontained HEPA filters.
	[1] enclosed (e.g., packages, filter or plena housing)	5.00E-04	1		
	[2] unenclosed	1.00E-02	1		
5.4.4	Aerodynamic Entrainment and Resuspensions				No significant release by nominal air velocities
6.0	***INADVERTENT NUCLEAR CRITICALITY***				This chapter is being revised and described in Chapter 4 of this paper.
	Solution	see comment	none		The criticality is generically considered terminated by the evaporation of 100 liters of water or some lesser amount. The airborne source term is given by $(MAR_{c1}*DR_{c1}*ARF_{c1})+(MAR_{s1}+DR_{s1}+ARF_{s1})$, where MAR_{c1} = inventory of gas and volatile, DR_{c1}=damage ratio for gases and volatiles generated in criticality, 1.0, ARF_{c1}=1 for noble gas, MAR_{s1}=inventory of non-volatile fission products generated, DR_{s1}=damage ratio radionuclides in solution, 1.0, and ARF_{s1}=5E-4 for non-volatiles, 1E-3 for ruthenium in fuel reprocessing solutions.
	Fully Moderated/Reflected Solids	see comment	none		This includes reflected bulk metal and metal pieces or solid fines such as powders that are moderated or reflected. It assumes no severe molten eructation, reactions and vaporization. Airborne source term = $MAR_{c2}*DR_{c2}*ARF_{C2}$, where MAR_{c2}=inventory of fissionable material and radionuclides from criticality, DR_{c2}=damage ratio, metal pieces=0.1, fines or powder=1.0, and ARF_{c2}=non-volatile can be neglected, 5E-1 for noble gases, and 5E-2 for iodine.

Chapter /section	Category	ARF	RF	Initial Size Distribution	Comments*
	Bare, Dry solids	see comment	none		No moderation, rather reflection. Airborne source term = MAR_{c3}*DR_{c3}*ARF_{c3}, where MAR_{c3}=inventory of radionuclides from fission, DR_{c3}=damage ratio, metal pieces=0.1, fines or powder=0.1, and ARF_{c3}=5E-1 for noble gas, 5E-2 for iodine.
	Large Storage Arrays				No data available

*NSRD-6 [Louie 2015], NSRD-11 [Louie 2016]

Appendix B: Users Guide for Micromorphic Fragmentation Model

In this appendix, the proposed users guides for the implementation of a micromorphic fragmentation described in Chapter 2 are provided. The sequential fragmentation material model description is provided first. Then the current proposed concurrent fragmentation material model follow.

B.1 Sequential Fragmentation Users Guide

MicroFragmentation_Sequential

Description of a two-scale fragmentation model implemented as a LAMÉ Material Model

The two-scale damage mechanics model with fragmentation implemented in LAMÉ is accessed as `MicroFragmentation Sequential`. The material model is intended to calculate fragmentation of brittle materials with a two-scale modeling paradigm. At the continuum length-scale, the material is described using SIERRA/SM's Gradient Damage Explicit (GDE) scheme to distribute nonlocal damage evolution in the material and determine the size of the macroscale fragments produced; The resolution is limited by the length-scale inherent in the GDE approach. The unique capability of the material model described is the ability to calculate the distribution of microscale fragments. Microscale fragments are assumed to originate from elements that are determined to have failed according the GDE model. Once element failure occurs at a user specified value, a microscale model solves the elasto-dynamic governing equation is solved explicitly with a finite di
erence scheme. The strain rate applied to the element is chosen to be a constant value set upon the element reaching a value of damage specified by the user. The length of fragments formed must be in a unit length of material defined by regularly spaced preexisting cohesive zones. The cohesive zones open upon reaching a critical stress. These cohesive zones are able to support a load in compression after separation occurs, but the loss in tensile strength is permanent. This model reports the resulting fragment mass distribution in the form of a histogram with the range and bin sizes specified by the user in the input file. Summary statistics (average size and standard deviation) are calculated on a per element basis.

1 Theory

The damage evolution of the material model is governed by the gradient damage mechanics [1] and implemented via an explicit scheme in SIERRA/SM and described elsewhere. A summary of the gradient damage scheme is provided here for consistency. Gradient damage is an extension of continuum damage mechanics that accounts for nonlocal interactions. The stress-strain constitutive law for brittle elastic materials is modified to include a damage normalization function $A(a)$ which is a function of the local damage a, such that

$$\sigma = A(a)\,\mathbf{E} : \epsilon, \tag{1}$$

where σ is the stress tensor and $\mathbf{E}$ is the Hooke elasticity tensor with the constraint that $0 \leq A(a) \leq 1$. The damage a spatially evolves according to the equation,

$$f\left(Y, \nabla^2 a\right) = Y + \frac{3}{8}\ell G_c \nabla^2 a - \frac{3}{4}\frac{G_c}{\ell}, \tag{2}$$

where Y is the damage driving force calculated as the strain energy resulting from the positive components of strain, G_c is the fracture energy, and ℓ is the nonlocal length scale.

Below the length scale governed by the GDE model (approximately equal to the characteristic length ℓ) this material model employs an implementation of the 1D microfragmentation model described in Ref. 2. The 1D model is necessary to calculate fragment sizes too fine for the GDE technique to resolve. The 1D model represents the material as linear-elastic with cohesive zones inserted at regular intervals along the bar. Upon meeting a minimum damage criteria, the equivalent 1D strain rate,

$$\dot{\epsilon}^{1D} = \dot{\epsilon}_{xx}^2 + \dot{\epsilon}_{yy}^2 + \dot{\epsilon}_{zz}^2 + 2\left(\dot{\epsilon}_{xy}^2 + \dot{\epsilon}_{yz}^2 + \dot{\epsilon}_{zx}^2\right), \tag{3}$$

is used to initiate the microfragmentation model. The cohesive zones are characterized by their variable opening displacement δ_{coh} and stress σ_{coh}. The opening behavior of the cohesive zones is described by the cohesive law proposed by Zhou, et al. [3]:

$$\frac{\sigma_{\text{coh}}}{\sigma_c} = 1 - \frac{\delta_{\text{coh}}}{\delta_c}, \quad \text{for } \dot{\delta}_{\text{coh}} > 0, \delta_{\text{coh}} = \delta_{\max}, \tag{4}$$

and for cohesive zone closing,

$$\frac{\sigma_{\text{coh}}}{\sigma_c} = 1 - \frac{\delta_{\max}}{\delta_c}, \quad \text{for } \delta_{\text{coh}} < \delta_{\max}. \tag{5}$$

The zones have a critical opening stress σ_c, critical opening displacement δ_c, and a maximum opening distance $\delta_{\max}$. Note that damage is defined as the ratio of the maximum to critical cohesive zone opening displacement as,

$$D = \min\left(\frac{\delta_{\max}}{\delta_c}, 1\right), \tag{6}$$

such that the damage of each zone can never decrease. Cohesive zones are deemed to have failed (unable to support further tensile load) when the damage reaches a value of one. When calculating the number of fragments produced, cohesive zones that are fully damaged will divide the bar into microscale fragments.

2 Implementation

The two-scale fragmentation model is implemented in two separate stages. First, the GDE model is employed to calculate macroscale damage evolution in the system. Second, the 1D microfragmentation model [2] is applied to a bar of equivalent mass for each failed element that meets the user specified `FAILURE_CRITERIA` for the continuum damage. Upon attaining a user specified amount of continuum damage, `DAMAGE_THRESHOLD`, the strain rate is stored and used to initialize the 1D fragmentation model.

The GDE model is implemented within SIERRA/SM and documented elsewhere. The GDE model governs the damage evolution in the material such that the GDE calculated damage is compared with the `FAILURE_CRITERIA` to determine which elements are removed from the system. Each failed element is divided into N_{seg} segments with cohesive zones between them. The 1D model is implemented using a finite difference scheme along characteristic lines as proposed by Zhou, et al. [3]. The 1D strain is calculated according to (3) and stored when the GDE damage reaches `DAMAGE_THRESHOLD` for use in the 1D microfragmentation model. The 1D strain rate determines the velocity boundary condition applied to the end segments of the bar. Each cohesive zone is

given an initial velocity based on the 1D strain rate applied in increasing amounts from the center of the bar until reaching the velocity boundary condition at either end. The specified INITIAL MICROFRAGMENTATION STRESS FACTOR is the initial condition of stress as a fraction of the critical stress causing failure. The initial stress is applied uniformly across the bar at each cohesive zone.

The 1D model is run for MAX MICROFRAGMENTATION STEPS timesteps. Each timestep is equal to the time it takes for an elastic wave to propagate between two cohesive zones. The distance between the cohesive zones defines the minimum fragment size, or resolution, of the technique.

3 User Guide

This guide is intended to assist the user in controlling the model, what is computed, and how to interpret the information provided by the model.

The most sensitive parameter in determining the fragment distribution is the strain rate. The choice of what level of material damage at which to store the single strain rate applied to the 1D microfragmentation model is of critical importance. This damage is set through the DAMAGE THRESHOLD input. However, the resulting fragmentation behavior is only calculated if the element reaches the stress degradation value $(1-d)$ set using FAILURE CRITERIA. The ability to independently specify the failure and strain rate damage conditions allows for the strain rate at different points in the process to

Results are reported as state variables. Summary statistics of the resulting fragmentation distributions (mean and standard deviation of fragment size along with the total number of fragments) are provided for visualization or postprocessing. Due to limitations in the number of state variables that may be stored, and the fact that the total number are not known ahead of time, it is not possible to output the length and mass of individual microfragments. Instead, the material model creates a histogram using user supplied parameters to more compactly represent the resulting fragment size distribution.

3.1 Prerequisites

Element Death must be handled by the material model by including the command `material criterion = on` in the material death block. Other death conditions can be added, such as death on inversion, minimum timestep, or nodal Jacobian ratio limits, but are not required.

The material model requires the use of Gradient Damage block within the region specification.

```
begin gradient damage
  initial value = 0.0
  solve explicit = on
end
```

In order for the provided post-processing script to capture the full range of fragments produced, the resulting macroscale fragments must also be reported. This is done through a built-in feature of SIERRA/SM that is invoked using the following block within the `results output` block:

```
begin identify fragments
  output file = out.frag
  increment = 1.0e-6
end
```

Make sure to output the macroscale fragments at the same interval as the microfragmentation data is reported to ensure consistency.

3.2 Material Model Inputs

There a number of mandatory material properties and reporting parameters that must be provided (expressions in parentheses are the variables appearing in Sec. 1).

`YOUNGS MODULUS` Alternatively, provide LAMBDA and `SHEAR MODULUS` in lieu of Young's Modulus.

`DENSITY` Density of material.

`FRACTURE ENERGY` (G_c) Fracture Energy of material.

`CRITICAL STRESS` (σ_c) Critical Stress to cause crack formation (cohesive zone opening stress).

`FRACTURE LENGTH SCALE` (ℓ) Characteristic length scale for the gradient damage model. Recommended length is approximately five times the nominal element size.

`COHESIVE SHAPE` Parameter needed for parameterizing gradient damage model.

`PHASE VISCOSITY SCALE FACTOR` Parameter needed for parameterizing gradient damage model.

`MAX MICROFRAGMENTATION STEPS` Number of timesteps to run the 1D microfragmentation model. May need to be increased if small strain rates are present in the system. Default: 10,000

`INITIAL MICROFRAGMENTATION STRESS FACTOR` Fraction of `CRITICAL STRESS` applied in tension to the 1D bar at initiation of 1D fragmentation model. Default: 0.999.

`MIN FRAGMENT SIZE` The minimum fragment size (ΔX), that serves as the resolution of the model. This length sets the timestep of the 1D model using the speed of sound in the material.

`MAX FRAGMENT SIZE` The maximum fragment size (L_{bar}). This length should be set so as to capture the full range of fragments produced by the microfragmentation model. It may exceed the length of an individual element but the mass will be conserved as the 1D bar thickness is scaled to compensate. The maximum fragment size should be at least twice the cohesive zone: $L_{\text{bar}} = 2\ell$.

`BIN MIN` Minimum fragment size that will be included in the mass histogram of microscale fragments. It is recommended to set this value equal to the spatial resolution of the 1D model (`MIN FRAGMENT SIZE`).

`BIN MAX` Maximum length of fragment that will be included in mass histogram of microscale fragments. It is recommended to set this value to L_{bar} (`MAX FRAGMENT SIZE`) or smaller as the longest segment possible microscale fragment is limited by L_{bar}.

`NBINS` Number of bins (N_{bins}) to use in histogram to report results over the range `BIN MIN` to `BIN MAX`.

`HIGH RESOLUTION BINS` Number of bins for the high resolution portion of the histogram in the low mass (length) region. Must be less than or equal to `NBINS`.

`HIGH RESOLUTION LIMIT` Size of largest bin included high resolution portion of the histogram in the low mass (length) region.

`DAMAGE THRESHOLD` Value of damage ($0 \leq d \leq 1$) at which the strain rate is stored initiate the microfragmentation calculation.

`FAILURE CRITERIA` Value of stress degradation, $1 - d$, that will result in element death and initiation of the microfragmentation model.

3.3 Available Outputs

The state variables available for output, on a per-integration point basis, are described below. Required outputs that must be included in the exodus file output for use with Analysis Script are marked with †.

`ELASTIC STRAIN ENERGY` Local value of elastic strain predicted by FEM model without damage. This quantity is equated to 1D model's strain energy, so damage cancels.

`FRAG N TOTAL` Number of possible fragments $\leq N_{\text{seg}}$.

`FRAG N PARTIAL` Number of damaged cohesive zones that are still able to bear load in tension.

`FRAG N BROKEN`† Number of completely damaged cohesive zones that are unable to sustain tensile load.

`FRAG N CRITICAL` Number of cohesive zones where the stress has exceeded the critical stress to initiate separation of the zone.

`FRAG AVERAGE SIZE`† Average fragment length at integration point.

`FRAG STD DEVIATION`† First standard deviation of average fragment length.

`FRAG ELEMENT MASS` Mass of integration point that is conserved throughout the execution of the model.

`FRAG M UNDER` Total mass of fragments of length less than `BIN MIN`.

`FRAG M OVER` Total mass of fragments of length greater than `BIN MAX`.

`STRAIN RATE INIT`† The strain rate used in the 1D model is stored upon damage exceeding the `DAMAGE THRESHOLD` criteria specified by the material property

`CRITICAL STRESS`† Initially set equal to the material parameter of the same name but stored in a state variable to be available for modification with an `initial condition` block

`FRACTURE ENERGY`† Initially set equal to the material parameter of the same name but stored in a state variable to be available for modification with an `initial condition` block.

`DAMAGE DRIVING ENERGY` Energy driving the evolution of the Gradient Damage model.

`HISTOGRAM BIN #`† Total mass of fragments contained in a bin of the histogram generated from data provided in the material properties specification. Note that each bin must be requested separately as `HISTOGRAM BIN 0`, `HISTOGRAM BIN 1`, etc., with a maximum index of `NBINS-1`.

3.4 Post-Processing Scripts

After executing the model, the `extract_histogram.py` script must be executed to extract the fragment size histogram and other relevant data. The data can then be summarized and plotted using the `plot_fragmentation_histogram.py` script. Both scripts require certain outputs be included in the EXODUS file generated by SIERRA/SM. These quantities are marked with †in Sec. 3.3.

The `extract_histogram.py` This script uses SIERRA/SM python tools, so it must be executed where these are available and in PYTHON's path. In the listings below, default values for the parameters (if present) are provided within [ ]. Note that both of the post-processing scripts are designed to work with either the `MicroFragmentation Concurrent` and `MicroFragmentation Sequential` material models, and not all options will be relevant for each. The `extract_histogram.py` script has the options:

```
  -h, --help            show this help message and exit

Mandatory Mutually exclusive options (c/s):
  -c, --concurrent      Assume MicroFragmentation Concurrent Material Model
  -s, --sequential      Assume MicroFragmentation Sequential Material Model

Optional Arguments:
  -ep EPATH, --epath EPATH
                        Local path to the directory containing exodus files to
                        be processed. [current working directory]
  -e [EFILES [EFILES ...]], --efiles [EFILES [EFILES ...]]
                        Exodus files to be processed (if not specified, script
                        searches for *.e*.* or *.e files)
  -r REXT, --rext REXT  Restart file extension used to filter exodus files for
                        processing. [none]
  -b FRAC_BLOCK, --frac_block FRAC_BLOCK
                        Define block ID to be processed
  -n NBINS, --nbins NBINS
                        Number of histogram bins [50]
  -v, --verbose         Increase verbosity
  -t, --time            pick time step [last]
  --bins_lo BINS_LO     Minimum Length Bin [0 m]
  --bins_hi BINS_HI     Maximum Length Bin [500.0e-6 m]
```

The `plot_fragmentation_histogram.py` post-processing script calculates and plots fragment size distribution histogram and the cumulative mass distribution. Many options are available for post-processing and generating the plots. Arguments available to this command-line tool are listed below:

```
  -h, --help            show this help message and exit

Mandatory Mutually exclusive options (c/s):
  -c, --concurrent      Assume MicroFragmentation Concurrent Material Model
  -s, --sequential      Assume MicroFragmentation Sequential Material Model

Optional Mutually exclusive options (m/M):
  -m, --micro           Plot only MicroScale Fragments
  -M, --Macro           Plot only MacroScale Fragments

Mandatory Arguments:
  -t THICKNESS, --thickness
                        Thickness of ceramic [20e-6 m]
```

```
  -d INPUT_DATA, --input_data
                        Input datafile (*.data from extract_histogram.py)

Optional arguments:
  -b FRAG_BLOCK, --frag_block
                        Block name of pellet [string: block_100]
  --bin-min BIN_MIN     Minimum bin size of histogram [default reads from data
                        file] (bin_min in sierra input)
  --bin-max BIN_MAX     Maximum bin size of histogram [default reads from data
                        file] (bin_max in sierra input)
  -e, --exp             Plot experimental data? Choose:
                        Jardin 1982: {UO2,pyrex}
                        Kraftwerk Union: {210,1050,5250,9502}
  -f FRAGFILENAME, --fragfilename
                        specifies fragment file generated by SIERRA/SM
  --high_res_limit HIGH_RES_LIMIT
                        Maximum Fragment length of high resolution region
                        [20um]
  --high_res_bins HIGH_RES_BINS
                        Number of high resolution bins [20]
  -k, --cut             Cut-off last bin (prevent spike)?
  -l LBAR, --lbar length of 1D bar [1000.0e-6 m] (LBAR or Max Fragment
                        Size in sierra input, needed for sequential
                        analysis option only )
  --logy                Make number of particle y-axis logarithmic
  -n, --norm_length_hist
                        Normalize the length histogram by the total number of
                        fragments
  -p RHO, --rho RHO     Density of ceramic [10500.0 kg/m^3])
  --time TIME           Enter time to find [last time in seconds]
  --two-scale TWO_SCALE Use two-scales for fragment lengths
  -w DIAM, --diam       Diameter of pellet [13.7e-3 m]
  --xlim_rate XLIM_RATE X limits of strain rate histogram
  --ylim_rate YLIM_RATE Y limits of strain rate histogram
  -y YLIM YLIM, --ylim  Y limits of histogram [0-1e6 scale]
  --ylim_mass YLIM_MASS Y limits of histogram [1e-8 to 1 default, set to [0,0]
                        for autoscale]
```

3.5 Notes

The element type used with this material model should contain only a single integration point. If more than one integration point is present, the 1D fragmentation analysis will be applied to each integration point separately. This will result in inconsistent behavior as the fragment mass distribution is generated assuming that each material point has the same mass as the element.

Acknowledgements

This work was funded by DOE Nuclear Safety Research and Development (NSRD) Program under WAS Project No. 2016HS201601210. Sandia National Laboratories is a multimission laboratory managed and operated by National Technology and Engineering Solutions of Sandia, LLC, a wholly owned subsidiary of Honeywell International, Inc., for the U.S. Department of Energy's National Nuclear Security Administration under contract DE-NA0003525.

References

[1] Eric Lorentz, S. Cuvilliez, and K. Kazymyrenko. Convergence of a gradient damage model toward a cohesive zone model. *Comptes Rendus - Mecanique*, 339(1):20–26, 2011. ISSN 16310721. doi: 10.1016/j.crme.2010.10.010. URL http://dx.doi.org/10.1016/j.crme.2010.10.010.

[2] David L Y Louie, Alexander L Brown, Fred Gelbard, John Bignell, Filnt Pierce, Tyler Voskuilen, Salvador B Rodriguez, Rémi Dingreville, Ethan T Zepper, Pierre-Alexandre Juan, San Le, and Lindsay N Gilkey. NSRD-11: Computational Capability to Substantiate DOE-HDBK-3010 Data. Technical Report SAND2016-12167, Sandia National Laboratories, 2016.

[3] Fenghua Zhou, Jean François Molinari, and K. T. Ramesh. A cohesive model based fragmentation analysis: Effects of strain rate and initial defects distribution. *International Journal of Solids and Structures*, 42(18-19):5181–5207, 2005. ISSN 00207683. doi: 10.1016/j.ijsolstr.2005.02.009.

B.2 Concurrent Fragmentation Users Guide

MicroFragmentation_Concurrent

Description of a two-way coupled continuum-microfragmentation model implemented as a LAMÉ Material Model

The two-way coupled fragmentation model implemented in LAM É is accessed as `Microfrag-mentation Concurrent` when selecting material models. The material model is intended to calcu-late fragmentation of brittle materials with a multiscale modeling paradigm. At the continuum length-scale, the material is described as brittle linear-elastic with damage accounted for using SIERRA/SM's Phase Field Reaction Di usion scheme to distribute nonlocal damage in the material; The resolution at the macroscale is limited by the length-scale inherent in the Reaction Di usion approach. The unique capability of the material model described is the ability to calculate the distribution of microscale fragments concurrently with the macroscale fragments. The damage value (the source term for the reaction di usion equation) is calculated via solving the elasto-dynamic governing equation explicitly with a finite di erence scheme. The damage calculated by the microscale model is related to continuum damage mechanics by ensuring strain compatibility across length scales. The length of fragments formed will be in terms of the unit length of material defined by regularly spaced preexisting cohesive zones. The cohesive zones open upon reaching a critical stress. These cohesive zones are able to support a load in compression after separation occurs, but the loss in tensile strength is permanent. This model reports the resulting fragment mass distribution in the form of a histogram with a range and bin sizes specified by the user in the input file. Summary statistics (average size and standard deviation) are calculated on a per element basis.

1 Theory

A summary of the theory used to develop this model is provided to aid in understanding how to use the model and interpret the results.

1.1 Microscale Damage Model

Below the length scale governed by the phase-field model (approximately equal to the characteristic length ℓ) this material model employs an implementation of the 1D fragmentation model described in Ref. [1]. In this approach, each failed element is represented by a 1D bar of equivalent mass with a specified total length minimum fragment size. A cohesive zone is assumed to exist between each segment. The strain energy calculated by the continuum model is used to calculate an equivalent 1D strain, and the equivalent 1D strain-rate, that results in the 1D bar having the same strain

energy as the failed material point. The 1D strain-rate is continually updated from the macroscale model to ensure continuity with the macroscale model. The 1D model calculates fragment sizes too fine for the finite element technique to resolve.

The 1D model represents the material as linear-elastic with cohesive zones inserted at regular intervals along the bar. The cohesive zones are characterized by their variable opening displacement δ_{coh} and stress σ_{coh}. The opening behavior of the cohesive zones are described by the cohesive law proposed by Zhou et al. [2]:

$$\frac{\sigma_{\text{coh}}}{\sigma_c} = 1 - \frac{\delta_{\text{coh}}}{\delta_c}, \quad \text{for } \dot{\delta}_{\text{coh}} > 0, \delta_{\text{coh}} = \delta_{\max}, \tag{1}$$

and for cohesive zone closing

$$\frac{\sigma_{\text{coh}}}{\sigma_c} = 1 - \frac{\delta_{\max}}{\delta_c}, \quad \text{for } \delta_{\text{coh}} < \delta_{\max}. \tag{2}$$

Note that damage is defined as the ratio of the maximum to critical cohesive zone opening displacement as,

$$D = \min\left(\frac{\delta_{\max}}{\delta_c}, 1\right). \tag{3}$$

The zones have a critical opening stress σ_c, critical opening displacement δ_c, and a maximum opening distance $\delta_{\max}$. Cohesive zones are deemed to have failed (unable to support further tensile load) when the damage reaches a value of one. Note that $\delta_{\max}$ is the maximum crack opening displacement of any cohesive zone. When calculating the number of fragments produced, cohesive zones that are fully damaged will divide the bar into microscale fragments.

1.2 Continuum Damage Model

The damage evolution of the material model is governed by a phase-field model and implemented via an implicit scheme in SIERRA/SM and described elsewhere. Internally to SIERRA/SM the phase-field solver is referred to as reaction-diffusion. A summary of the reaction-diffusion damage scheme is provided here for consistency. The reaction-diffusion approach is an extension of continuum damage mechanics that accounts for nonlocal interactions between damage in nearby elements. The stress-strain constitutive law for brittle elastic materials is modified to include degradation of the stress where, $0 \leq c \leq 1$, such that

$$\boldsymbol{\sigma} = c^2 \mathbf{E} \boldsymbol{\epsilon}, \tag{4}$$

where $\boldsymbol{\sigma}$ is the stress tensor, $\boldsymbol{\epsilon}$ is the strain tensor, and $\mathbf{E}$ is the Hooke elasticity tensor. The c term is the value of the phase-field that evolves from 1 (intact) to 0 (fully degraded).

The macroscale damage model is an implicit phase-field model implemented within SIERRA/SM and described elsewhere. A summary of the phase-field scheme is provided here for consistency of presentation. The phase-field model of Borden et al. [3] (Eq. 22b), provides for non-local damage evolution by solving:

$$\left(\frac{4\ell\mathcal{H}(\psi_e^+)}{\Gamma} + 1\right)c - 4\ell^2\nabla^2 c = 1, \tag{5}$$

where c is the phase-field, ℓ is the nonlocal length-scale, Γ is the energy that can be dissipated by crack opening, and $\mathcal{H}$ is a history function which ensures that the 1D undamaged extensional (positive) strain energy ψ_e^+ only increases. This history function is also applied to the entire first

term of the equation to ensure that the phase-field damage cannot decrease. This can occur because Γ is not fixed in the present formulation as it was in the Borden et al. [3] formulation. The phase-field has a value of 1 for undamaged material and decreases toward 0 with increasing degradation (damage) in the material. The phase-field is defined such that the damaged stress tensor is the sum of the undamaged tensile and compressive strain energies with the tensile component multiplied by the decay coefficient:

$$\sigma_{ij} = c^2 \frac{\partial \psi_e^+}{\partial \epsilon_{ij}} + \frac{\partial \psi_e^-}{\partial \epsilon_{ij}}. \tag{6}$$

Using a Griffith model of fracture where is the fracture energy release-rate, we assume $\Gamma = G_c$. However, due to the presence of the microscale model, Γ is not equal to the energy dissipated in the model at the onset of fracture as it would be in the case of Griffith fracture. The microscale model can actually dissipate more than G_c due to the presence of multiple cohesive zones in the 1D bar. According to Eq. 15 of Zhou et al. [2], the energy dissipated in the 1D bar due to partially opened cracks is $\sum_i D_i^2 G_c$, summed over all cohesive-zones, where the damage measure ($0 \leq D_i \leq 1$) is defined by (3).

The coupling between the length-scales occurs via the energy dissipated by cohesive-zone opening at the microscale. Equation(5) is formulated under the premise that the energy ratio in the first term goes to unity upon meeting the condition for fracture, assuming only a single crack in each element. Due to the presence of multiple cohesive-zone crack nucleation sites, the dissipated energy exceeds G_c by $\sum_i D_i^2 G_c$. To ensure the ratio goes to 1 when any given cohesive-zone becomes fully damaged, the maximally damaged ($D_{\max} = \max D_i$) cohesive-zone energy must be removed from the total amount of dissipated energy. The total energy that may be dissipated due to fracture in (5) becomes

$$\Gamma = G_c \left(1 + \sum_{i=1}^{N_{\text{seg}}} D_i^2 - \max D_i^2 \right). \tag{7}$$

This expression ensures that, in the case of one fully-opened (fractured) cohesive-zone, the dissipated energy is the sum of the partially opened cohesive-zone energies and from the fully-opened cohesive-zone. Thus, we replace Γ in (5) with (7) so that

$$\left(\frac{4\ell \mathcal{H}(\psi_e^+)}{G_c \left(1 + \sum_{i=1}^{N_{\text{seg}}} D_i^2 - \max D_i^2 \right)} + 1 \right) c - 4\ell^2 \nabla^2 c = 1 \tag{8}$$

This is the phase-field equation solved implicitly during model execution. Due to the way this model was formulated by Borden et al. [3], the critical stress σ_c' where the value of the phase-field and stress decrease with increasing strain is

$$\sigma_c' = \frac{9}{16} \sqrt{\frac{E G_c}{6\ell}}. \tag{9}$$

For consistency between length-scales, the phase-field model's critical stress σ_c' must reach the material's critical stress σ_c used in the 1D fragmentation model. This may be accomplished by replacing E with a modified Young's modulus $E^\star$. Substituting E for $E^\star$ and replacing σ_c' with σ_c in (9), the fracture length-scale ℓ is found to be

$$\ell = \frac{27}{512} \frac{E^\star G_c}{\sigma_c^2}. \tag{10}$$

Substituting the expression for ℓ into the phase-field's value of critical strain,

$$\epsilon_c' = \sqrt{\frac{G_c}{6\ell E^\star}}, \tag{11}$$

it is found that, in order for the materials critical strain and stress to be related according to Hook's law ($\sigma_c = E^\star \epsilon_c$), the modified modulus must be

$$E^\star = \frac{16}{9} E. \tag{12}$$

Using $E^\star$ as the modulus at the macroscale guarantees that the conditions for cohesive-zone opening at the microscale and degradation of the stress tensor will occur simultaneously. With this approach, the maximum principle stress may exceed σ_c because the amount of energy dissipated increases with cohesive zone opening. Therefor, to prevent the unphysical situation of the maximum principle stress ($\max \sigma^P$) exceeding that for cohesive zone opening, the phase-field value in (6) must satisfy

$$c^2 = \min\left(c^2, \sigma_c / \max\left(\sigma^P\right)\right). \tag{13}$$

The microscale model of fracture is identical to that used in the sequentially-coupled fragmentation model but with the boundary conditions continually updated to reflect the changing loading conditions on each element. The conditions are updated each macroscale time-step before the microscale model is executed over its smaller time-step (governed by the speed of sound and fragment resolution requested) to advance the microscale model to the next macroscale time-step. As in the sequentially-coupled model, each element contains a single instance of the 1D microscale model. As the microscale model employs a 1D representation of the material, the continuum state of stress must be projected onto a single dimension. The direction is chosen by recognizing that microcracks will form normal to the maximum principle stress when that stress exceeds σ_c. Upon the state of stress meeting this condition in an element, the direction of the maximum principle stress is recorded. All future crack opening must occur along the direction recorded when the maximum principle stress first reached σ_c. The projection of the continuum state of stress is denoted as ϵ_M.

2 Implementation

Each integration point (or element if each contains a single integration point) is represented by a 1D bar with length $L = \sqrt[3]{V}$, equivalent to the size of a cube with the same mass as the integration point. The 1D bar is divided into N_{seg} segments of length ΔX. A cohesive zone is assumed to exist between each segment with a cohesive law specified in (1) and (2). The strain energy calculated by the continuum model is used to calculate an equivalent 1D strain, and then the equivalent 1D strain rate. The 1D strain rate is used to update the boundary conditions of the 1D fragmentation model that will be run for as many microscale timesteps (based on the speed of sound and minimum fragment size) as necessary to reach the next continuum timestep.

As soon as the maximum principle stresses in an element reaches or exceeds the critical stress for fracture, the direction of applied stress is recorded so that only the component of tension in that direction can cause opening of the cracks. This choice was made to ensure that once cohesive zones begin to separate (cracks start to form) they will effectively concentrate stress and suppress crack formation in other directions.

SIERRA/SM provides the strain tensor for the present time-step to the material model: ϵ_i. The continuum stress is calculated from the continuum strain at the current time-step i without

damage as $\sigma_i = E\epsilon_i^e$. This is accomplished by directly calculating the stress from the given strain without applying the damage. The microscale model is initiated upon an element decaying to the critical value of the phase-field defined by Borden et al. [3] as $c_c = \sqrt{\sigma_c/E\epsilon_c} = 3/4$. At this point, the direction of applied stress ς is stored and the current continuum state of stress is projected onto that direction thereafter.

The strain applied to the microscale model is calculated at the current time-step as

$$\epsilon_i = \frac{\sigma_i \cdot \varsigma}{E}. \tag{14}$$

The strain-rate projected from the macroscale model $\dot{\epsilon}_i$ is provided by SIERRA/SM at a mid-step value. The strain-rate at the current timestep $\dot{\epsilon}_{i-1}$ therefor calculated consistent with the 1D strain by using the prior value of the 1D strain ϵ_{i-1} to calculate the current value of strain rate,

$$\dot{\epsilon}_i = \frac{\epsilon_i - \epsilon_{i-1}}{\Delta t}, \tag{15}$$

The microscale fragmentation model then calculates the evolution of cohesive-zone opening and stress in the bar. This microscale damage in each cohesive-zone is used to calculate the value of the phase-field at the next timestep as described previously.

3 User Guide

3.1 Prerequisites

The material model requires the use of Reaction Diffusion block, within the region specification:

```
begin reaction diffusion
  initial value = 1.0
  block         = {block_XXX}
end
```

The block specification `block_XXX` must be replaced with the block containing the material that is described by the `MicroFragmentation_Concurrent` material model.

Element Death must be handled by the material model by including the command `material criterion = on` in the material death block. Other death conditions can be added, such as death on inversion, minimum timestep, or nodal Jacobian ratio limits, but are not required.

3.2 Material Model Inputs

There a number of mandatory material properties and reporting parameters that must be provided Optional variables are marked with [o] after their names and default values with units are given in braces [ ]

`YOUNGS MODULUS` Alternatively, provide `LAMBDA` and `SHEAR MODULUS` in lieu of Young's Modulus. [none]

`DENSITY` Density of material. [10500 kg/m^3]

`FRACTURE ENERGY` (G_c) Value of the energy needed to cause crack opening. [none]

`CRITICAL STRESS` (σ_c) Critical Stress to cause crack formation (cohesive zone opening stress). [none]

`MIN FRAGMENT SIZE` [o] The minimum fragment size (ΔX), that serves as the resolution of the model. This length sets the timestep of the 1D model using the speed of sound in the material. [1.0 μm]

`MAX FRAGMENT SIZE` [o] The maximum fragment size (L_{bar}). Used only to allocate memory, must be larger than the largest mass equivalent element dimension in the sample. [500.0 μm]

`BIN MIN` [o] Minimum fragment size that will be included in the mass histogram of microscale fragments. It is recommended to set this value equal to the spatial resolution of the 1D model (`MIN FRAGMENT SIZE`). [1 μm]

`BIN MAX` [o] Maximum length of fragment that will be included in mass histogram of microscale fragments. To ensure all fragments are accounted for in the histogram, it is recommended that this quantity be set equal to `MAX FRAGMENT SIZE`. [1000 μm]

`NBINS` [o] Total number of bins (N_{bins}) to use in histogram to report results over the range specified by `BIN MIN` to `BIN MAX`. [120]

`HIGH RES NBINS` [o] Number of bins for the high resolution portion of the histogram in the low mass (length) region from `BIN MIN` to `HIGH RES LIMIT`. Must be less than or equal to `NBINS`. [20]

`HIGH RES LIMIT` [o] Size of largest bin included in the high resolution portion of the histogram in the low mass (length) region. [20.0 μm].

`FRACTURE LENGTH SCALE` [currently unused] Automatically set to ensure that maximum principle stress is reached in element that meets condition for phase-field failure ($c \leq 0.75$).

`MAX PRINCIPAL STRESS FAILURE FLAG` [o] Used to replace the use of ψ_e^+ with the strain energy calculated using the maximum principle stress. The value is the fraction of the strain energy at the critical value for cohesive-zone opening stress that is calculated from the ratio of the maximum principle stress to the critical stress as $\left(\max \sigma_i^P/\sigma_c\right)^2 \cdot \left(\frac{1}{2}\sigma_c^2/E^\star\right)$.

3.3 Available Outputs

The state variables available for output, on a per-integration point basis, are described below. (expressions in parentheses are the variables appearing in Sec. 1). Required outputs that must be included in the exodus file output for use with Analysis Script are marked with †.

`CRITICAL STRESS`† Initially set equal to the material parameter of the same name but stored in a state variable to be available for modification with an `initial condition` block.

`FRACTURE ENERGY`† Initially set equal to the material parameter of the same name but stored in a state variable to be available for modification with an `initial condition` block.

`FRAG N TOTAL` Number of possible fragments $\leq N_{\text{seg}}$.

`FRAG N PARTIAL` Number of damaged cohesive zones that are still able to bear load in tension.

`FRAG N BROKEN`† Number of completely damaged cohesive zones that are unable to sustain tensile load.

FRAG N CRITICAL Number of cohesive zones where the stress has exceeded the critical stress to initiate opening of the cohesive zone.

FRAG AVERAGE SIZE† Average fragment length at integration point.

FRAG STD DEVIATION† First standard deviation of average fragment length.

FRAG ELEMENT MASS† Mass of integration point that is conserved throughout the execution of the model.

FRAG M UNDER† Total mass of fragments of length less than BIN MIN.

FRAG M OVER† Total mass of fragments of length greater than BIN MAX.

STRAIN RATE 1D The strain rate experienced by the element at the condition where the failure direction is recorded. This value provides a representative initial strain-rate for any element.

STRESS 1D The stress experienced by the element at the condition where the failure direction is recorded. This value provides a representative initial stress applied to the 1D bar representing each element.

RXNCOEF MAX Maximum value of the reaction coefficient. The reaction coefficient is the term in parentheses in front of the phase-field (c) variable in (5).

STRAIN 1D Equivalent 1D strain at integration point to produce the same strain energy as the continuum calculation (without damage).

DISSIPATED ENERGY RATIO Energy dissipated at the microscale. This quantity is defined by the portion of (7) that includes $G_c\left(\sum_{i=1}^{N_{seg}} D_i^2 - \max D_i^2\right)$.

N SEGMENTS Total number of possible fragments at integration point, expressed in units of ΔX.

FAILURE DIRECTION X Failure direction (ς) recorded upon the value of phase-field reaching the critical value of $c = 0.75$. (Components X,Y,Z)

UNDAMAGED STRESS TENSOR XX (Components XX,YY,ZZ,ZX,YX,ZY)

LENGTH SCALE The quantity ℓ calculated via (10).

PHASE FIELD FRACTURE ENERGY Fracture energy calculated by teh phase-field model per unit volume defined as $G_c(1 + \text{DISSIPATED ENERGY RATIO}) \cdot \left(\ell \nabla c \cdot \nabla c + (c-1)^2/(4\ell)\right)$.

PF DAMAGE The quantity $1 - c$.

LEFT END LENGTH† Length of the fragment that contains the left-hand end of the bar.

RIGHT END LENGTH† Length of the fragment that contains the right-hand end of the bar.

HISTOGRAM BIN #† Total mass of fragments contained in a bin of the histogram generated from data provided in the material properties specification. Note that each bin must be requested separately as HISTOGRAM BIN 0, HISTOGRAM BIN 1, etc., with a maximum index of NBINS−1.

3.4 Post-Processing Scripts

After executing the model, the `extract_histogram.py` script must be executed to extract the fragment size histogram and other relevant data. The data can then be summarized and plotted using the `plot_fragmentation_histogram.py` script. Both scripts require certain outputs be included in the EXODUS file generated by SIERRA/SM. These quantities are marked with † in Sec. 3.3.

The `extract_histogram.py` This script uses SIERRA/SM python tools, so it must be executed where these are available and in PYTHON's path. In the listings below, default values for the parameters (if present) are provided within [ ]. Note that both of the post-processing scripts are designed to work with either the `MicroFragmentation Concurrent` and `MicroFragmentation Sequential` material models, and not all options will be relevant for each. The `extract_histogram.py` script has the options:

```
  -h, --help            show this help message and exit

Mandatory Mutually exclusive options (c/s):
  -c, --concurrent Assume MicroFragmentation Concurrent Material Model
  -s, --sequential Assume MicroFragmentation Sequential Material Model

Optional Arguments:
  -ep EPATH, --epath EPATH
                        Local path to the directory containing exodus files to
                        be processed. [current working directory]
  -e [EFILES [EFILES ...]], --efiles [EFILES [EFILES ...]]
                        Exodus files to be processed (if not specified, script
                        searches for *.e*.* or *.e files)
  -r REXT, --rext REXT  Restart file extension used to filter exodus files for
                        processing. [none]
  -b FRAC_BLOCK, --frac_block FRAC_BLOCK
                        Define block ID to be processed
  -n NBINS, --nbins NBINS
                        Number of histogram bins [50]
  -v, --verbose         Increase verbosity
  -t, --time            pick time step [last]
  --bins_lo BINS_LO     Minimum Length Bin [0 m]
  --bins_hi BINS_HI     Maximum Length Bin [500.0e-6 m]
```

The `plot_fragmentation_histogram.py` post-processing script calculates and plots fragment size distribution histogram and the cumulative mass distribution. Many options are available for post-processing and generating the plots. Arguments available to this command-line tool are listed below:

```
  -h, --help            show this help message and exit

Mandatory Mutually exclusive options (c/s):
  -c, --concurrent      Assume MicroFragmentation Concurrent Material Model
```

```
  -s, --sequential      Assume MicroFragmentation Sequential Material Model

Optional Mutually exclusive options (m/M):
  -m, --micro           Plot only MicroScale Fragments
  -M, --Macro           Plot only MacroScale Fragments

Mandatory Arguments:
  -t THICKNESS, --thickness
                        Thickness of ceramic [20e-6 m]
  -d INPUT_DATA, --input_data
                        Input datafile (*.data from extract_histogram.py)

Optional arguments:
  -b FRAG_BLOCK, --frag_block
                        Block name of pellet [string: block_100]
  --bin-min BIN_MIN     Minimum bin size of histogram [default reads from data
                        file] (bin_min in sierra input)
  --bin-max BIN_MAX     Maximum bin size of histogram [default reads from data
                        file] (bin_max in sierra input)
  -e, --exp             Plot experimental data? Choose:
                        Jardin 1982: {UO2,pyrex}
                        Kraftwerk Union: {210,1050,5250,9502}
  -f FRAGFILENAME, --fragfilename
                        specifies fragment file generated by SIERRA/SM
  --high_res_limit HIGH_RES_LIMIT
                        Maximum Fragment length of high resolution region
                        [20um]
  --high_res_bins HIGH_RES_BINS
                        Number of high resolution bins [20]
  -k, --cut             Cut-off last bin (prevent spike)?
  -l LBAR, --lbar length of 1D bar [1000.0e-6 m] (LBAR or Max Fragment
                        Size in sierra input, needed for sequential analysis
                        option only )
  --logy                Make number of particle y-axis logarithmic
  -n, --norm_length_hist
                        Normalize the length histogram by the total number of
                        fragments
  -p RHO, --rho RHO     Density of ceramic [10500.0 kg/m^3])
  --time TIME           Enter time to find [last time in seconds]
  --two-scale TWO_SCALE Use two-scales for fragment lengths
  -w DIAM, --diam       Diameter of pellet [13.7e-3 m]
  --xlim_rate XLIM_RATE X limits of strain rate histogram
  --ylim_rate YLIM_RATE Y limits of strain rate histogram
  -y YLIM YLIM, --ylim  Y limits of histogram [0-1e6 scale]
  --ylim_mass YLIM_MASS Y limits of histogram [1e-8 to 1 default, set to [0,0]
                        for autoscale]
```

3.5 Notes

The element type used with this material model should contain only a single integration point. If more than one integration point is present, the 1D fragmentation analysis will be applied to each integration point separately. This will result in inconsistent behavior as the fragment mass distribution is generated assuming that each material point has the same mass as the element.

SIERRA/SM has the `identify fragments` capability to identify macroscale fragments that contain contiguous regions of unbroken elements. These fragments are reported in a file that is needed by the post-processing script to account for their mass in the calculation of mass versus fragment size distribution. The file containing fragments is give as the `-f` or `--fragfilename` argument.

```
begin identify fragments
  output file = {NAME}.frag
  increment = {TIME}
end
```

Element Death must be handled by the material model by including the command `material criterion = on` in the material death block. Other death conditions can be added, such as death on inversion, minimum timestep, or nodal Jacobian ratio limits, but are not required. Now we only want to kill elements on the last timestep. This way, the code will calculate the macroscale fragments for us, but will not remove elements during analysis. We don't want to remove elements during analysis because they can still support compressive loading! To kill elements only on last timestep, we must include the `DEATH START TIME` command in the death block of the input file and set it to be a time just before the last timestep. Alternatively, a second time control block can be created in which the material criterion can be used to remove all elements that had met the death criteria.

```
begin element death material_failure
  include all blocks
  material criteria = on
  death start time = {TIME}
end
```

Acknowledgements

This work was funded by DOE Nuclear Safety Research and Development (NSRD) Program under WAS Project No. 2016HS201601210. Sandia National Laboratories is a multimission laboratory managed and operated by National Technology and Engineering Solutions of Sandia, LLC, a wholly owned subsidiary of Honeywell International, Inc., for the U.S. Department of Energy's National Nuclear Security Administration under contract DE-NA0003525.

References

[1] David L Y Louie, Alexander L Brown, Fred Gelbard, John Bignell, Filnt Pierce, Tyler Voskuilen, Salvador B Rodriguez, Rémi Dingreville, Ethan T Zepper, Pierre-Alexandre Juan, San Le, and Lindsay N Gilkey. NSRD-11: Computational Capability to Substantiate DOE-HDBK-3010 Data. Technical Report SAND2016-12167, Sandia National Laboratories, 2016.

[2] Fenghua Zhou, Jean François Molinari, and K. T. Ramesh. A cohesive model based fragmentation analysis: Effects of strain rate and initial defects distribution. *International Journal of Solids and Structures*, 42(18-19):5181–5207, 2005. ISSN 00207683. doi: 10.1016/j.ijsolstr.2005.02.009.

[3] Michael J. Borden, Clemens V. Verhoosel, Michael A. Scott, Thomas J R Hughes, and Chad M. Landis. A phase-field description of dynamic brittle fracture. *Computer Methods in Applied Mechanics and Engineering*, 217-220:77–95, 2012. ISSN 00457825. doi: 10.1016/j.cma.2012.01.008. URL http://dx.doi.org/10.1016/j.cma.2012.01.008.

DISTRIBUTION

External Distribution

2 U.S. Department of Energy
Office of Nuclear Safety - Nuclear Safety R&D Program
Attn: Alan Levin, NSR&D Program Manager
1000 Independence Avenue, SW
Germantown, MD 20585

2 U.S. Department of Energy
Office of Nuclear Safety Basis and Facility Design (AU-31)
Attn: Patrick Frias, NSR&D Project Manager
19901 Germantown Road (AU-31)
Germantown, MD 20874

1 U.S. Department of Energy
Office of Nuclear Safety Basis and Facility Design (AU-31)
Attn: Garrett Smith, Director, Office of Nuclear Safety Basis and Facility Design
19901 Germantown Road (AU-31)
Germantown, MD 20874

1 U.S. Department of Energy
Office of Nuclear Safety Basis and Facility Design (AU-31)
Attn: Samuel Rosenbloom
19901 Germantown Road (AU-31)
Germantown, MD 20874

1 U.S. Department of Energy
Office of Nuclear Energy
Attn: James C. Bresee
Mail Stop NE-52
19901 Germantown Road
Germantown, MD 20874

1 U.S. Nuclear Regulatory Commission
Office of Nuclear Material Safety and Safeguards
Attn: Wendy Reed, Division of Spent Fuel Management/LTSF
Mail Stop TWFN 4 B34
Washington DC, 20555-0001

1 U.S. Nuclear Regulatory Commission
Office of Nuclear Regulatory Research, Environmental Transport Branch
Attn: Mark Fuhrmann
Mail Stop TWFN 10 A12
Washington, DC 20555-0001

1 Louis F. Restrepo
Vice President, Business Development
Atkins Nuclear
1100 Rhode Island St. NE
Albuquerque, NM 87110

1 Jose R.O. Munoz
Assistant Manager for Operations
DOE-NNSA, Los Alamos Field Office
3747 West Jemez Road
Los Alamos, NM 87544

1 Robert D. Busch
Principal Lecturer – Department of Nuclear Engineering
University of New Mexico
MSC01 1120
1 University of New Mexico
Albuquerque, NM 87131-0001

1 Anil K. Prinja
Professor and Chair – Department of Nuclear Engineering
University of New Mexico
MSC01 1120
1 University of New Mexico
Albuquerque, NM 87131-0001

Internal Distribution

1	MS0721	Carol L. Adkins	8800
1	MS0736	Richard O Griffith	8850
1	MS0744	John Bignell	8853
1	MS0744	Patrick D. Mattie	8853
1	MS0747	Remi P.M. Dingreville	8853
1	MS0748	Nathan E. Bixler	8852
1	MS0748	Randall O. Gauntt	8852
1	MS0748	David L.Y. Louie	8852
1	MS0748	Christopher J. O'Brien	8853
1	MS0748	Corey M. Skinner	8852
1	MS1135	Alexander Brown	1532
1	MS1135	Carlos Lopez	1532
1	MS1135	Ethan T. Zepper	1532
1	MS0899	Technical Library	(electronic copy)


Sandia National Laboratories